NASA-CR-174805

National Aeronautics and
Space Administration

CONSTITUTIVE MODELING FOR ISOTROPIC MATERIALS

Annual Report

by

V.G. Ramaswamy
R.H. Van Stone
L.T. Dame
J.H. Laflen

General Electric Company
Aircraft Engine Business Group
Cincinnati, Ohio 45215

March 1985

Prepared For

National Aeronautics and Space Administration
Lewis Research Center
21000 Brookpark Road
Cleveland, Ohio 44135

(NASA-CR-174805) CONSTITUTIVE MODELING FOR ISOTROPIC MATERIALS Annual Report, May 1983 - Apr. 1984 (General Electric Co.) 86 p
CSCL 21E G3/07

N89-13436
Unclas
0181366

NASA-Lewis Contract
NAS3-23927

1 Report No	2 Government Accession No.	3. Recipient's Catalog No
NASA-CR-174805		

4 Title and Subtitle	5. Report Date
CONSTITUTIVE MODELING FOR ISOTROPIC MATERIALS	15 April 1985
	6. Performing Organization Code

7. Author(s)	8. Performing Organization Report No
V.G. Ramaswamy, R.H. Van Stone, L.T. Dame, J.H. Laflen	
	10. Work Unit No

9 Performing Organization Name and Address	11. Contract or Grant No.
General Electric Company Aircraft Engine Business Group 1 Neumann Way Cincinnati, Ohio 45215	NAS3-23927
	13. Type of Report and Period Covered Annual Report May 1983 - April 1984

12. Sponsoring Agency Name and Address	14. Sponsoring Agency Code
National Aeronautics and Space Administration Lewis Research Center 21000 Brookpark Road Cleveland, Ohio 44135	

15 Supplementary Notes

16. Abstract

This report documents the first year of progress on a NASA-Lewis contract with the General Electric Co. The purpose of this contract (NAS3-23927) is to develop and evaluate unified constitutive equations for application to hot-path components of aircraft gas turbine engines such as high pressure turbine blades and vanes. To accomplish this goal, uniaxial, notched, and multiaxial specimens made of conventionally cast René 80 are being tested under conditions that simulate engine operating conditions. To reduce the raw data, automated data reduction techniques are being developed that produce computer files containing the information needed to analyze proposed constitutive theories. Described in this report are the analytical methods being developed to determine the parameters for these nonlinear unified theories by using the reduced data files. In another activity, a dedicated finite-element computer code is being developed to use unified theories in the structural analysis of hot-section components. This code has been extensively verified for one such theory by successfulyy predicting the strain histories measured experimentally at the notch root of complex specimens taken from complex laboratory specimens.

17. Key Words (Suggested by Author(s))	18. Distribution Statement
Constitutive modeling, finite element modeling, nickel-base alloys, nonlinear unified theory, structural analysis	UNLIMITED

19 Security Classif. (of this report)	20. Security Classif. (of this page)	21. No. of Pages	22 Price*
UNCLASSIFIED	UNCLASSIFIED	80	

* For sale by the National Technical Information Service, Springfield, Virginia 22161

ABSTRACT

(Constitutive Modeling for Isotropic Materials)

This report documents the first year's progress on a NASA-Lewis contract with the General Electric Company. The purpose of this contract (NAS3-23927) is to develop and evaluate unified constitutive equations for application to hot path components of aircraft gas turbine engines such as high pressure turbine blades and vanes. To accomplish this goal, uniaxial, notched, and multiaxial specimens made of conventionally cast Rene' 80 are being tested under conditions which simulate engine operating conditions. In order to reduce the raw data, automated data reduction techniques are being developed which produce computer files which contain the information required in the analysis of proposed constitutive theories. As described in the report, analytical methods are being developed for determining the parameters in these nonlinear unified theories by using these reduced data files. In another activity, a dedicated finite element computer code is being developed for using unified theories in structural analyses of hot section components. This code has been extensively verified for one such theory by successfully predicting the strain histories measured experimentally at the notch root of complex specimens of complex laboratory specimens.

TABLE OF CONTENTS

LIST OF ILLUSTRATIONS

LIST OF ILLUSTRATIONS (Concluded)

LIST OF TABLES

1.0 INTRODUCTION

The inelastic finite element analytic model that is chosen for a particular type of numerical analysis of material behavior represents a compromise between (1) the requirements of physical verisimilitude, (2) mathematical accuracy and stability, and (3) computational convenience and economy. In the past, the mathematical and computational problems have been so dominant that most analysts have been content to adopt simple uncoupled material models. Plasticity has been represented by an engineering stress-strain curve, monotonic or cyclic, and creep by a relatively uncomplicated power law equation.

It is well known that the simplest uncoupled material models ignored many of the more complex, well documented kinds of high temperature material behavior: inelastic recovery, cyclic creep, strain rate effects, and thermomechanical (simultaneous temperature and load variation) effects on material response. Recent work has evolved constitutive theories that contain representations for various combinations of these effects. Frequently these models do not separate the analytical treatment of time-dependent and time-independent inelastic strains as do more classic models; these methods are generally referred to as unified theories. It is the purpose of this NASA-sponsored program to thoroughly evaluate such methods for application to typical isotropic cast nickel base superalloys used for air-cooled turbine blades and vanes.

This objective is being accomplished through a two year combined analytical and experimental program. During this nine-task program, a nonlinear finite element program will be developed using the selected constitutive theory. The model will be evaluated against a series of uniaxial smooth specimen experiments selected both to determine material constants and for verification purposes. Additional experimental work on more complicated specimen geometries will be used to further evaluate the constitutive model and to develop efficient numerical algorithms for the nonlinear finite element code. These additional experiments will evaluate multiaxial states of stress; also, a notch specimen geometry will be subjected to a variety of loading conditions. The finite element computer program will be further demonstrated by modeling an actual hot path component such as a turbine blade or vane. At the end of the effort, the final computer program will be delivered to NASA.

This report summarizes the work performed during the first year of the contract.

2.0 INITIAL MODEL EVALUATION

The purpose of the initial model evaluation was to select two theories to be incorporated into a finite element computer program. The work described in this section was Task A of the contract.

A comprehensive literature survey of proposed constitutive theories was conducted by General Electric in order to identify the two most promising theories for use in subsequent tasks. Theories by the following authors were chosen for closer review:

1. Bodner et al. (Reference 1)
2. Chaboche (Reference 2)
3. Haisler et al. (Reference 3)
4. Hart (Reference 4)
5. Krempl (Reference 5)
6. Krieg, Swearengen, and Rohde (Reference 6)
7. Laflen and Stouffer (Reference 7)
8. Lee and Zaverl (Reference 8)
9. Miller (Reference 9)
10. Pian (Reference 10)
11. Robinson (Reference 11)
12. Valanis (Reference 12)
13. Walker (Reference 13)

To evaluate these theories, criteria were developed to measure various requirements for constitutive theories. These criteria considered material behavior phenomena, experimental requirements, and the numerical aspects of each theory. Fourteen criteria were developed:

1. Cyclic hardening and softening
2. Kinematic hardening
3. Strain-rate effects
4. Creep-plasticity interaction
5. Nonisothermal cycling
6. Anelastic effects
7. Thermal recovery
8. Generalization to multiaxial stress states
9. Extension to anisotropic materials
10. Ease of computer implementation
11. Computer storage requirements
12. Economy of integration
13. Ease of determining material constants
14. Cost of determining material constants

Prior to conducting a detailed review, a number of theories were eliminated for various reasons. The theories of Haisler et al. and Pian were

too classical for the purposes of the current study. In a similar vein, it was required that a theory not make use of a yield function; this eliminated the theories of Chaboche, and Lee and Zaverl. The method devised by Laflen and Stouffer was not considered since it had not been developed for cyclic loading conditions, a mandatory consideration for hot-section components. Similarly, the theory of Krempl was not evaluated in detail since it had not been totally developed for cyclic conditions at the time of the review. The theory of Valanis was eliminated bacause it has not yet been developed to consider different time-dependent flow effects in a unified fashion. Finally, the theory developed by Hart was eliminated because it called for specialized test data from a load relaxation experiment.

The five remaining theories were those of Bodner et al.; Krieg, Swearengen, and Rohde; Miller; Robinson; and Walker. Each was evaluated in detail against the fourteen criteria listed above. For each criterion, a theory could receive up to a maximum numerical score of three. At the end of this review all five theories were close in total score. Since the numerical rating system is somewhat subjective, all five theories were further evaluated through numerical comparison to determine if there were any distinguishing features which would aid in selecting the final two theories. A detailed description of the five unified theories is given in Appendix A.

Each of these five theories was programmed as a subroutine in a program that performed a simple numerical integration of three basic equations: the flow rule and the evolution equations for the state variables. All the theories selected for detailed evaluation except that of Bodner use two types of state variables - the back stress Ω and the drag stress Z. The subroutine developed from each theory performs simple numerical integration of the following equations:

$$\dot{\varepsilon}^{I}_{ij} = f\,[\sigma_{ij}, \Omega_{ij}, Z, T] \qquad (1)$$

$$\dot{\Omega}_{ij} = g\,[\sigma_{ij}, \Omega_{ij}, Z, T] \qquad (2)$$

$$\dot{Z} = h\,[\sigma_{ij}, \Omega_{ij}, Z, T] \qquad (3)$$

where $\dot{\varepsilon}^{I}_{ij}$ is the inelastic strain rate tensor, σ_{ij} is the stress tensor, and T is the temperature. In all the theories considered, the drag stress Z is a scalar. The theory of Bodner does not involve the back stress Ω_{ij}. The computer programs were written for three-dimensional model evaluations. Although some of these theories are not available in nonisothermal form, the basic evaluation described here were performed under isothermal conditions.

All of these theories involve a number of material parameters. At the time of evaluations, these parameters were not available for René 80, the base material for this project; therefore, for the purpose of evaluation of the theories, constants available for different materials and temperature in published literature were used.

Constitutive Theory	Material	Temperature, °F	Reference
Miller	Hastelloy X	1200	9
Walker	Hastelloy X	1200	13
Krieg, Swearengen, and Rohde	Aluminum	110	6
Bodner	René 95	1200	23
Robinson	2.25 Cr-1 Mo	1000	11

Using the computer program, the above theories have been evaluated in terms of their ability to model several basic aspects of material behavior. These include:

1. Strain rate sensitivity
2. Creep
3. Stress relaxation
4. History dependence
5. Cyclic hardening/softening
6. Anelasticity

Each of these considerations is discussed below.

2.1 STRAIN RATE SENSITIVITY

A basic feature of any unified constitutive theory is its sensitivity to strain rate. This can easily be verified using a simple monotonic loading; at different strain rates all the theories examined displayed this sensitivity. Some examples are shown in Figures 1-4. Although all these theories displayed the appropriate strain rate sensitivity, their state variables showed different characteristics. In the Bodner, Robinson, and Walker models, they saturated to the same limits at high strain rates, whereas in the Miller and Krieg et al. models, the limits of the state variables were rate dependent. The models of Bodner and Miller seem to have distinct point which depends on strain rate, where the stress-strain behavior changes from linear to nonlinear. However, none of these unified theories involves any specific yield criteria.

2.2 CREEP

Another fundamental ability required of any model is to predict the constant stress creep behavior of materials. This was verified for the models by loading uniaxially under constant strain rate and then holding at constant stress. All the models showed primary and secondary creep regimes. The models of Krieg et al. and Bodner are shown as examples in Figures 5 and 6.

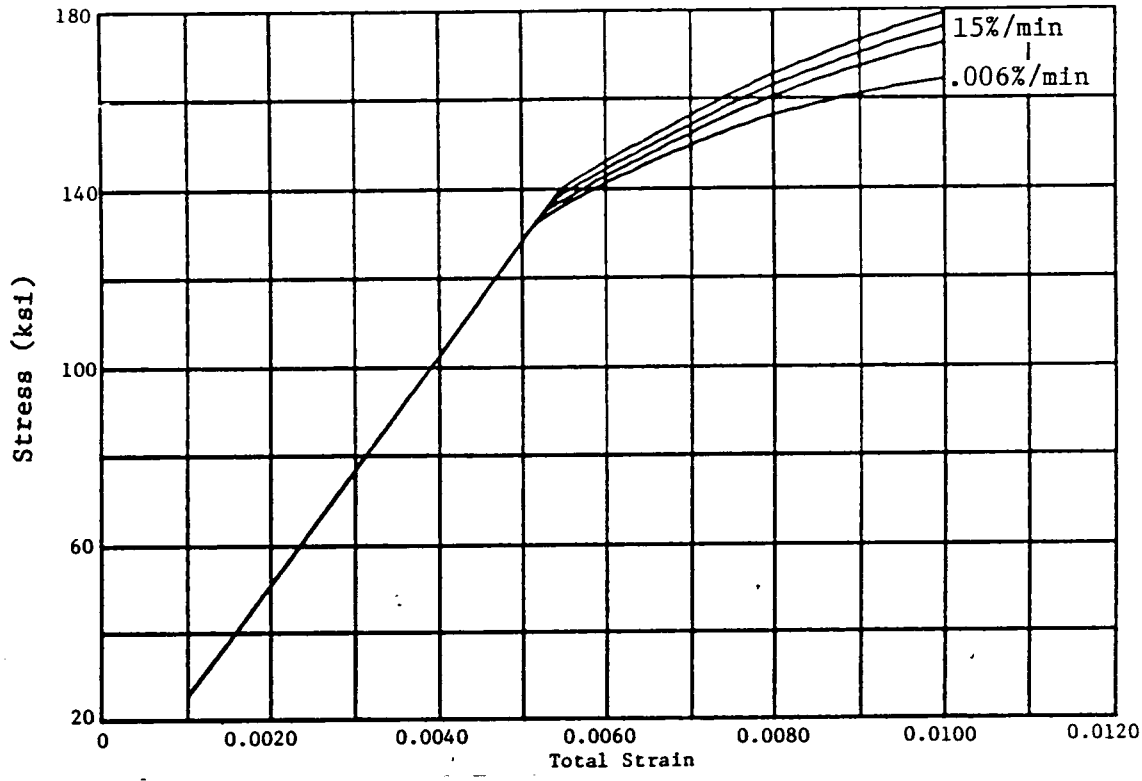

Figure 1. Bodner Model Strain Rate Sensitivity.

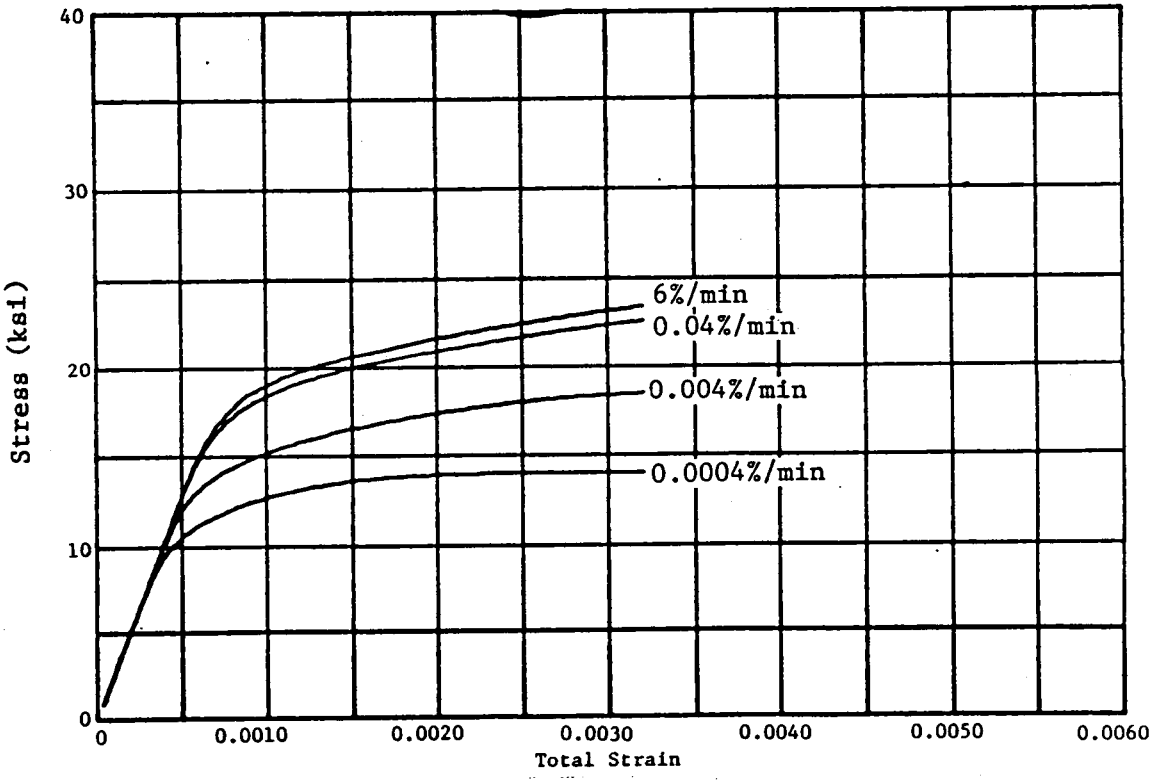

Figure 2. Robinson Model Strain Rate Sensitivity.

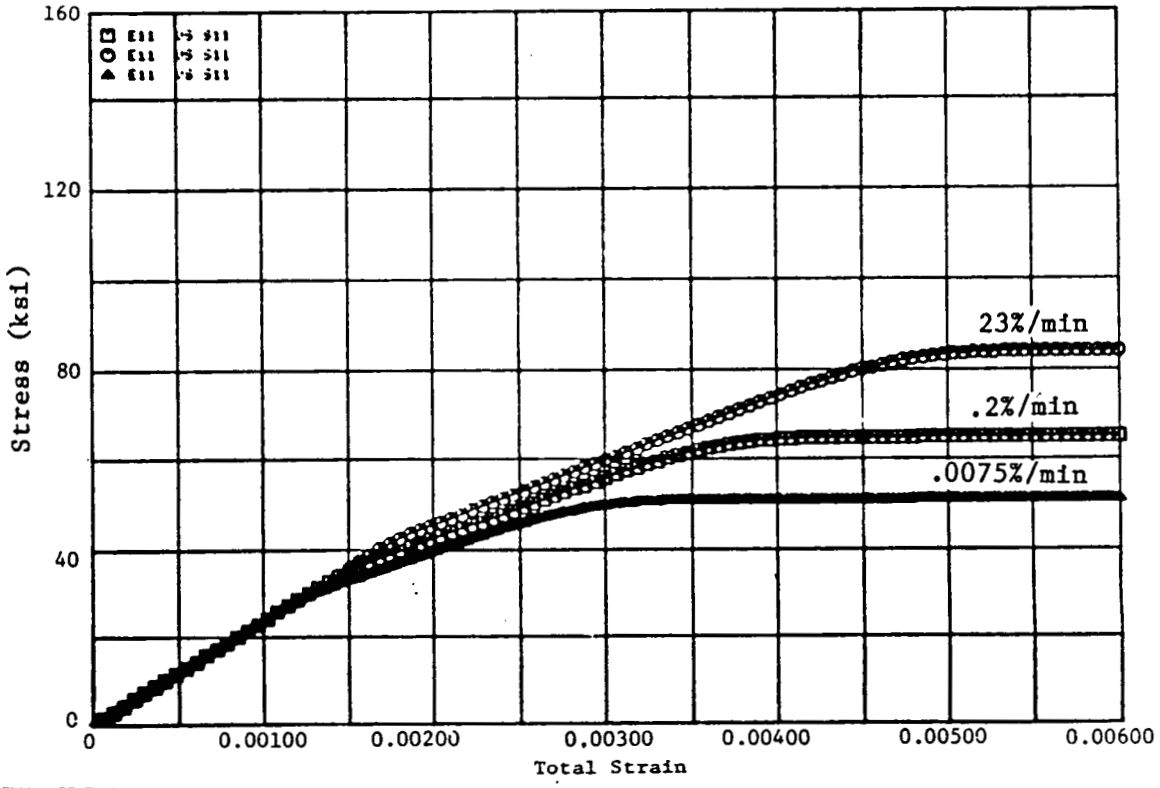

Figure 3. Miller Model Strain Rate Sensitivity.

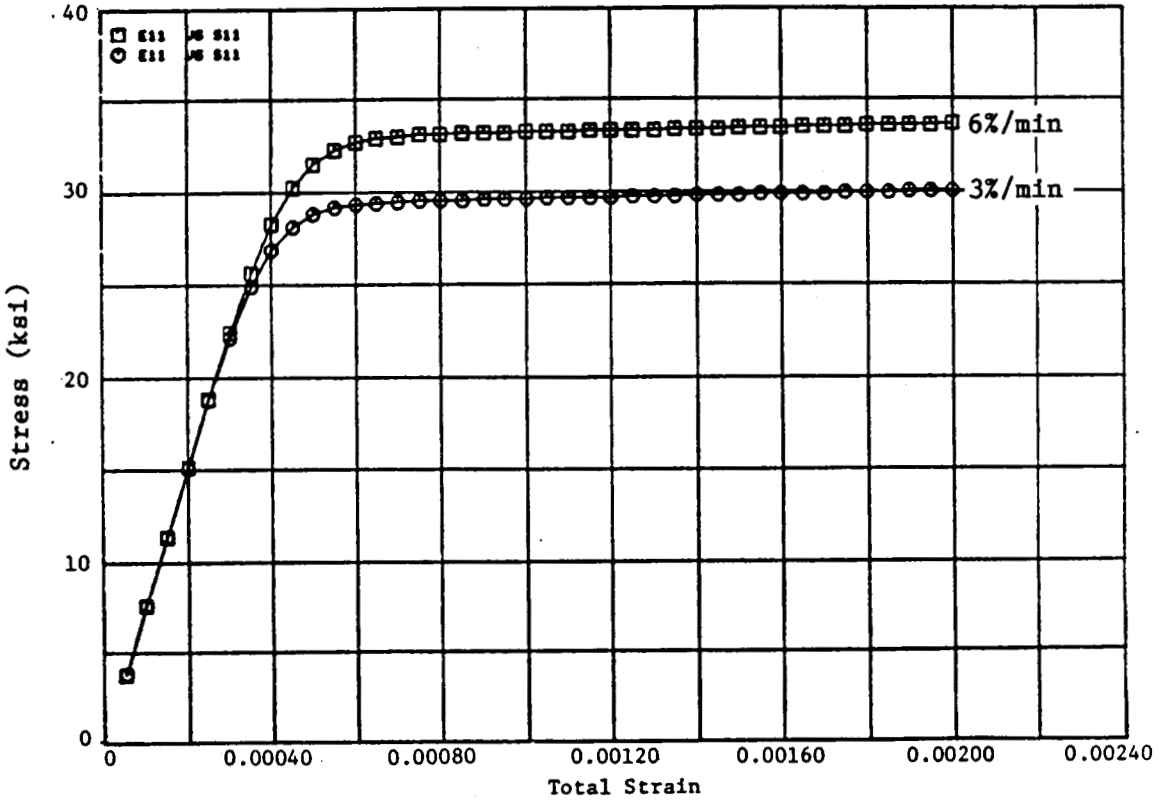

Figure 4. Krieg Model Strain Rate Sensitivity.

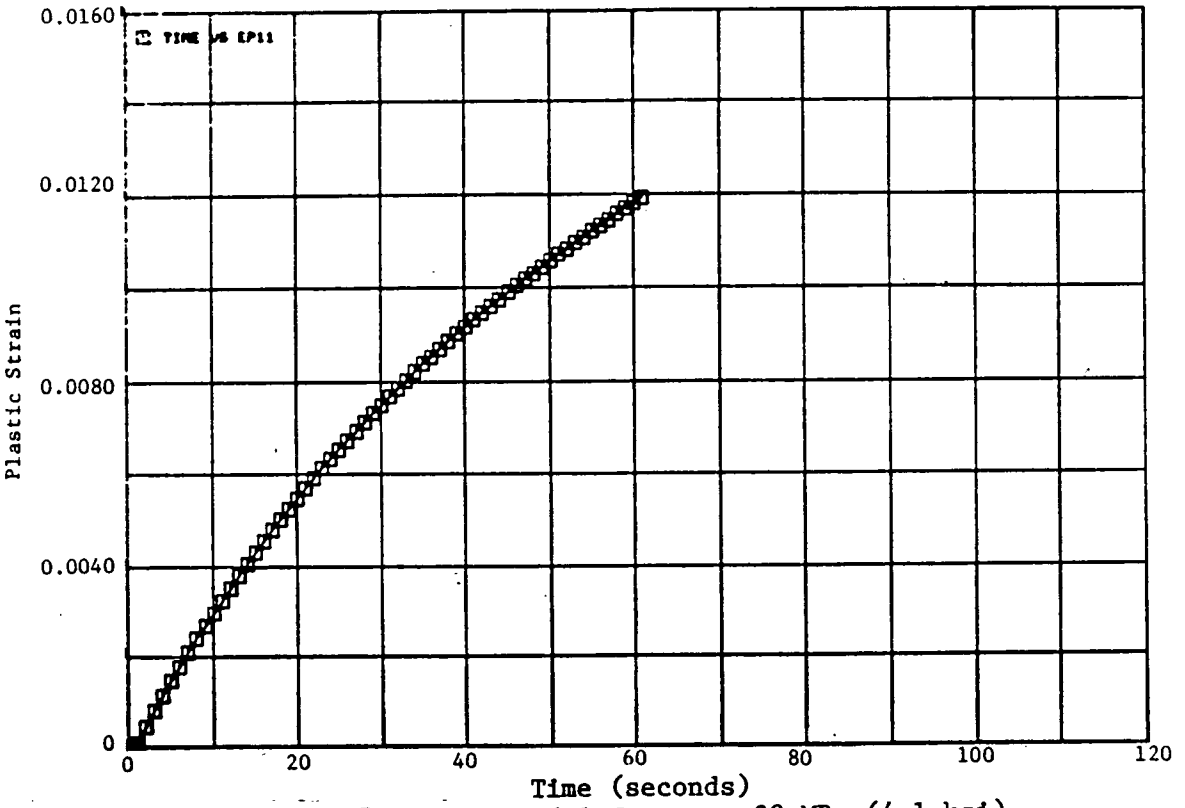

Figure 5. Krieg Model Creep at 28 MPa (4.1 ksi).

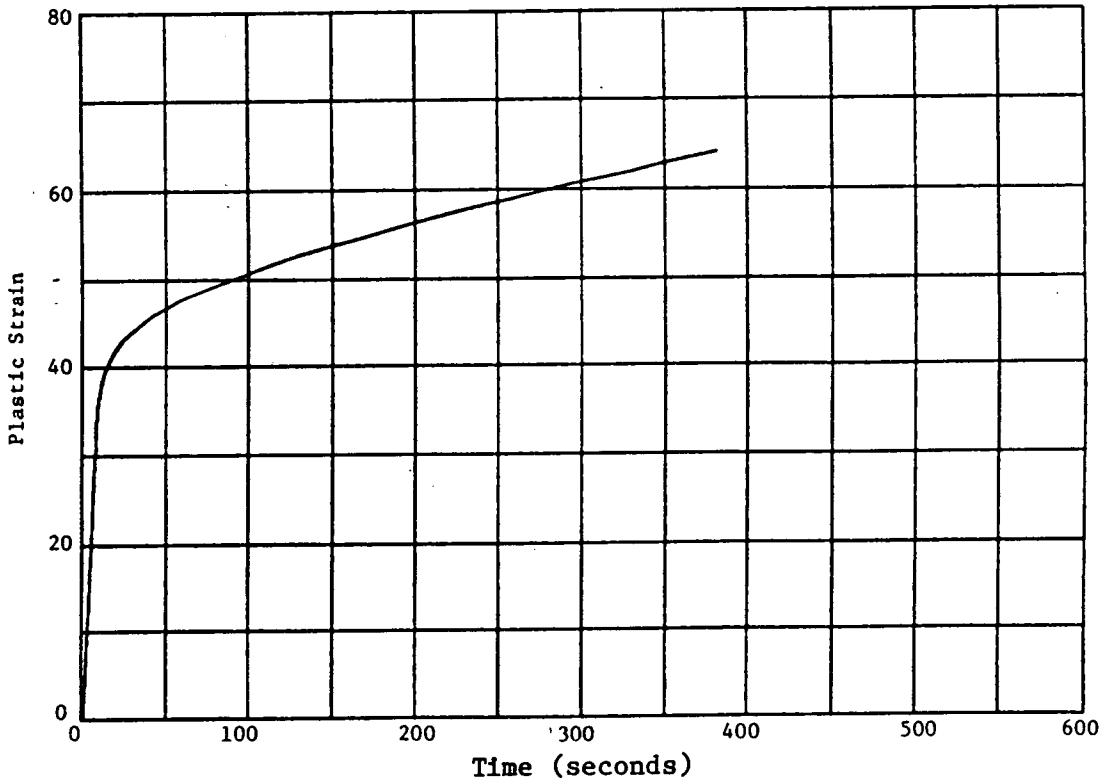

Figure 6. Bodner Model Creep at 1240 MPa (180 ksi).

Figure 7 shows the interesting results of an exercise using the Robinson model. It is well known that the steady state creep rate depends on the stress and temperature. Under isothermal conditions, many materials display a certain delay in the creep response when the stress is lowered during secondary creep. The ability of the unified theories to model such behavior was checked by exercising the Robinson model. Figure 7 shows four different creep cases superimposed for comparison. In Figure 7a, after steady state creep is reached, the stress is suddenly lowered. Figure 7b shows the creep response. It is seen that the creep resumes at a lower rate, after a brief delay. Figure 7c shows the response of the state variable (back stress in this case). It is seen to be gradually saturating to a lower limit. It was not conclusively determined if the creep response shown in Figure 7b is due to the inequalities in the Robinson model or is an inherent part of the unified theories. Reference 15 discusses the Robinson Model for high-temperature creep-plasticity.

2.3 STRESS RELAXATION

During strain hold tests, materials show stress relaxation. This feature has been verified for the theories. Figures 8 and 9 show the stress relaxation responses predicted by the models of Walker and Miller, respectively. These show a large amount of relaxation in a very short time (about 15 ksi in less than 30 seconds). This seems to be true of all the theories and materials examined. No stress relaxation data for the materials modeled were available for verification.

2.4 HISTORY DEPENDENCE

Any rate-dependent unified constitutive theory should be able to model the dependence of material behavior on prior deformation history. This ability in the various theories considered here was verified by exercising the computer model using "ramped" cyclic. The strain amplitude is increased gradually to finally involve inelastic strains in the reverse direction. These, together with the cyclic hysteresis loops and the response of the back stress state variable, are shown in Figures 10 through 12 for the Walker model and Figures 13 through 15 for the Robinson model. Note from Figure 11 and Figure 14 that these models exhibit ratcheting behavior, as is typical of real materials undergoing inelastic deformation. It is observed that the effect of initial deformation is wiped out when large inelastic strains are involved. Figures 12 and 15 show the behavior of a state variable, back stress. During this type of loading the back stress tends to saturate for large inelastic strains. The back stress remains constant during the beginning of loading or unloading when the inelastic strain rate is very small. (The sharp corners during loading and unloading phases of Figure 15 appear to be due to the basic form of the Robinson model, which involves inequalities.)

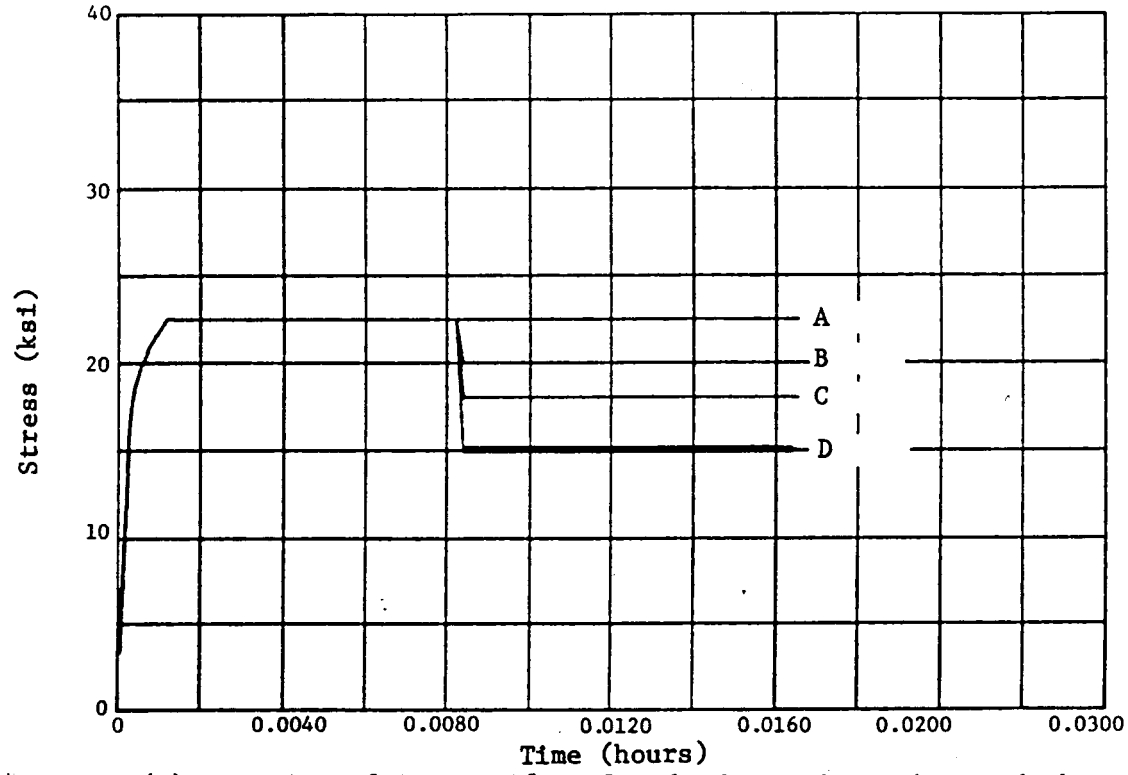

(a) Lowering of Stress After Steady-State Creep is Reached.

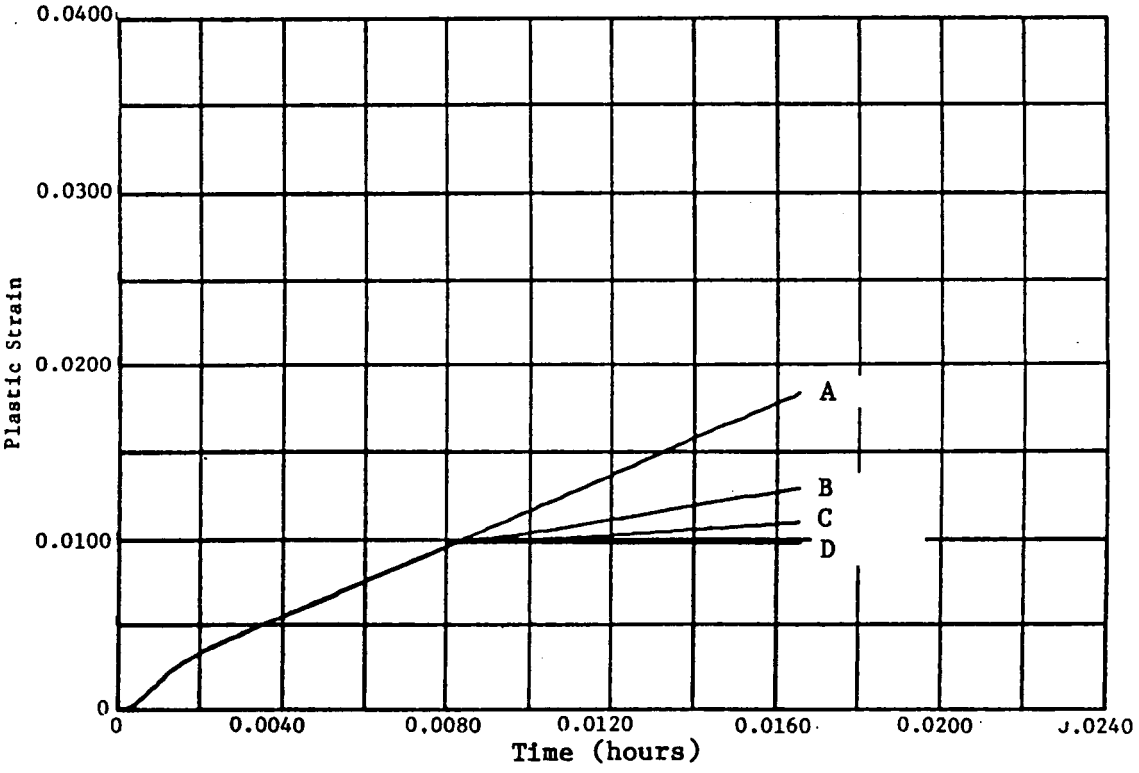

(b) Creep Response to Lowering of Stress.

Figure 7. Robinson Model, Creep - Four Cases (A, B, C, D) Superimposed.

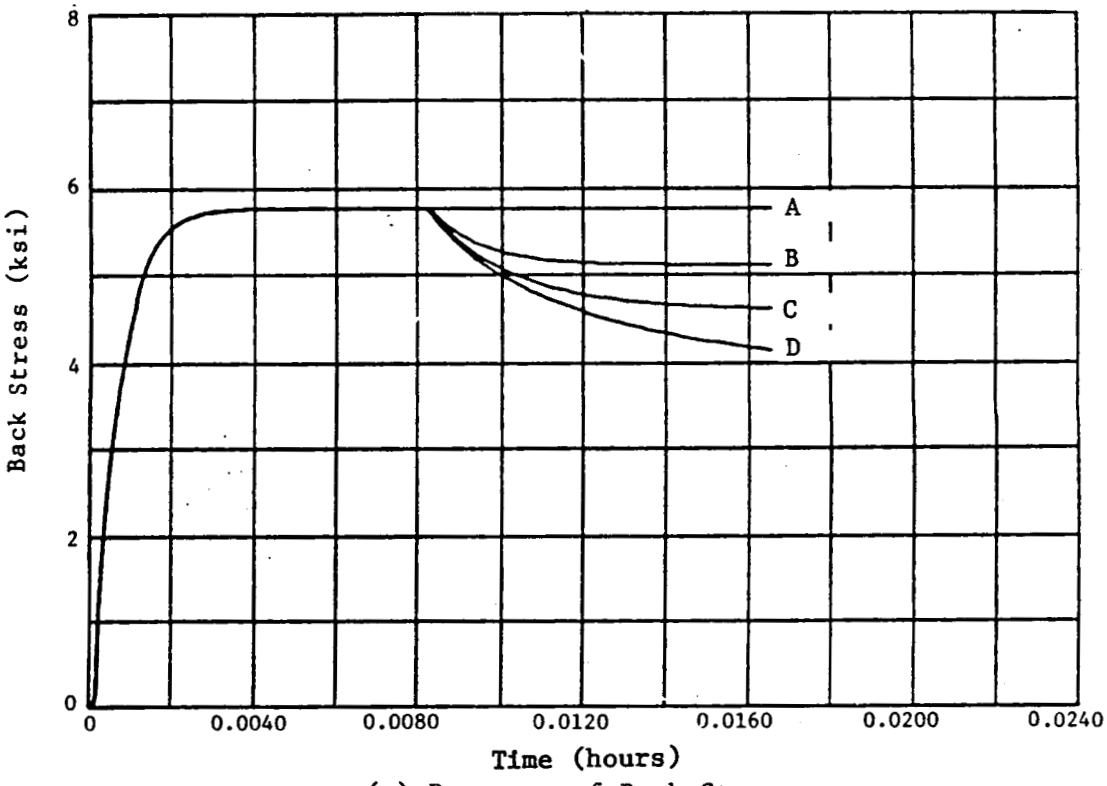

(c) Response of Back Stress.

Figure 7. Robinson Model, Creep - Four Cases (A, B, C, D) Superimposed (Concluded).

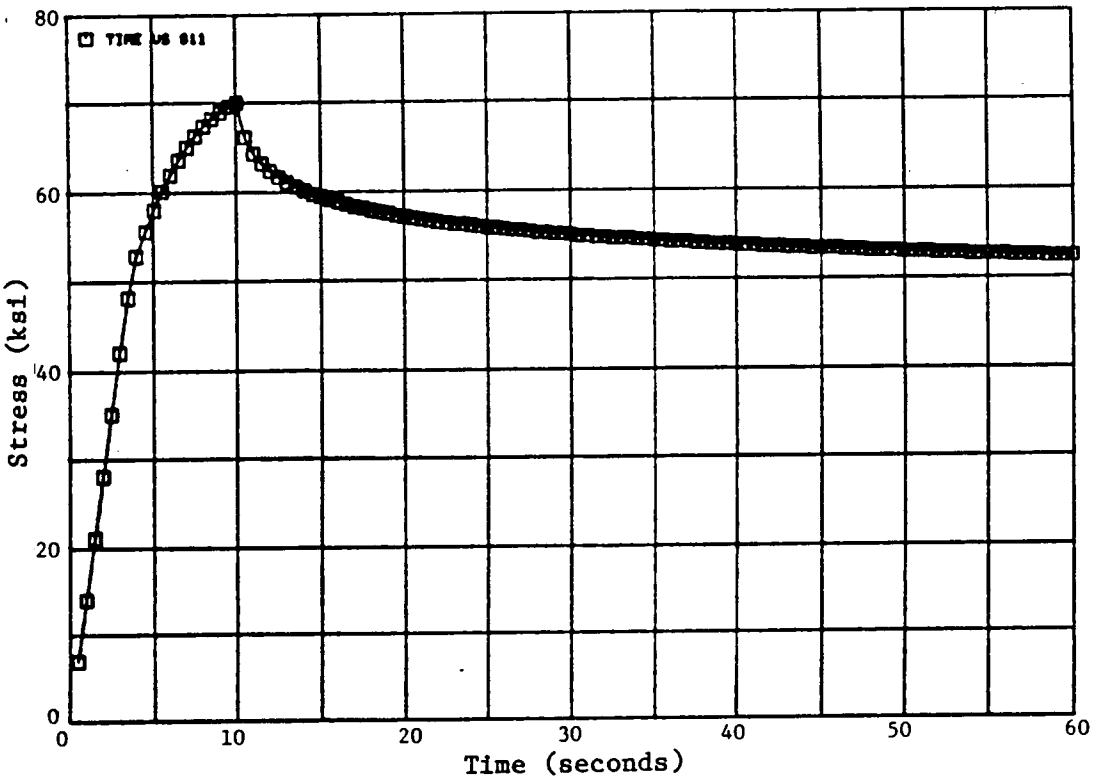

Figure 8. Walker Model, Stress Relaxation.

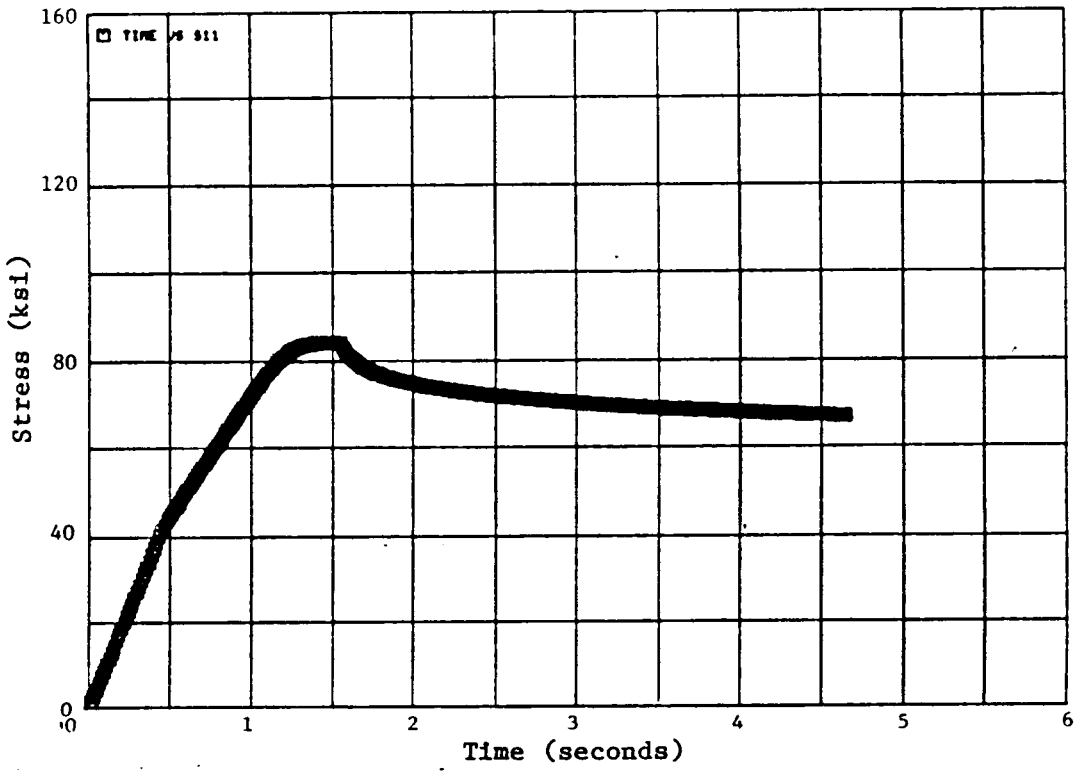

Figure 9. Miller Model, Stress Relaxation.

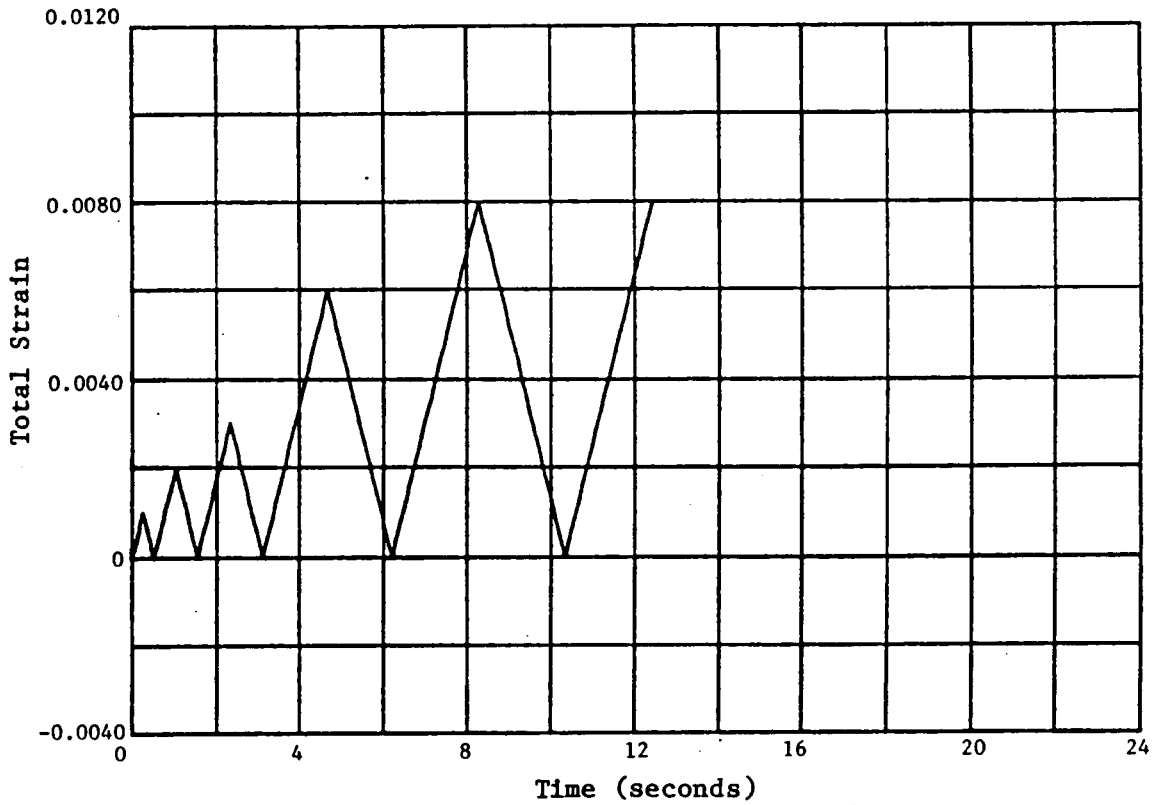

Figure 10. Walker Model, Ramped Cycles - Cyclic Strains (Control).

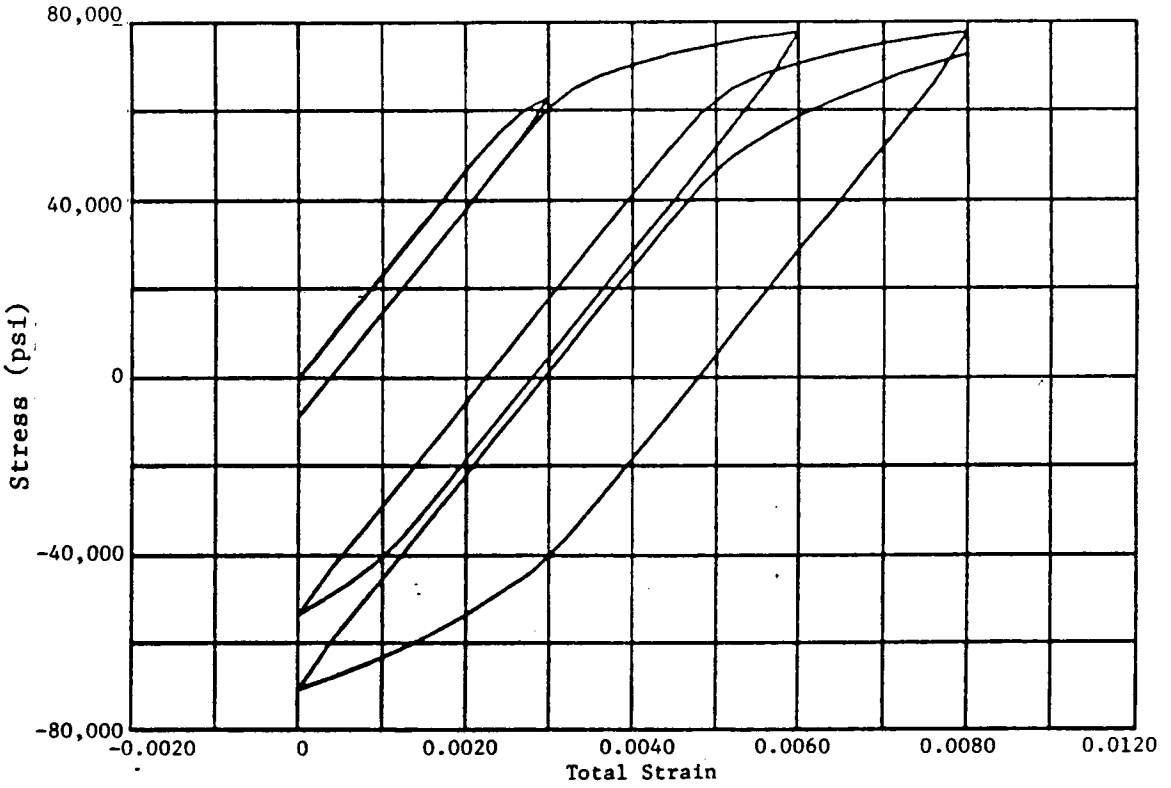

Figure 11. Walker Model, Ramped Cycles - Cyclic Hysteresis Loops.

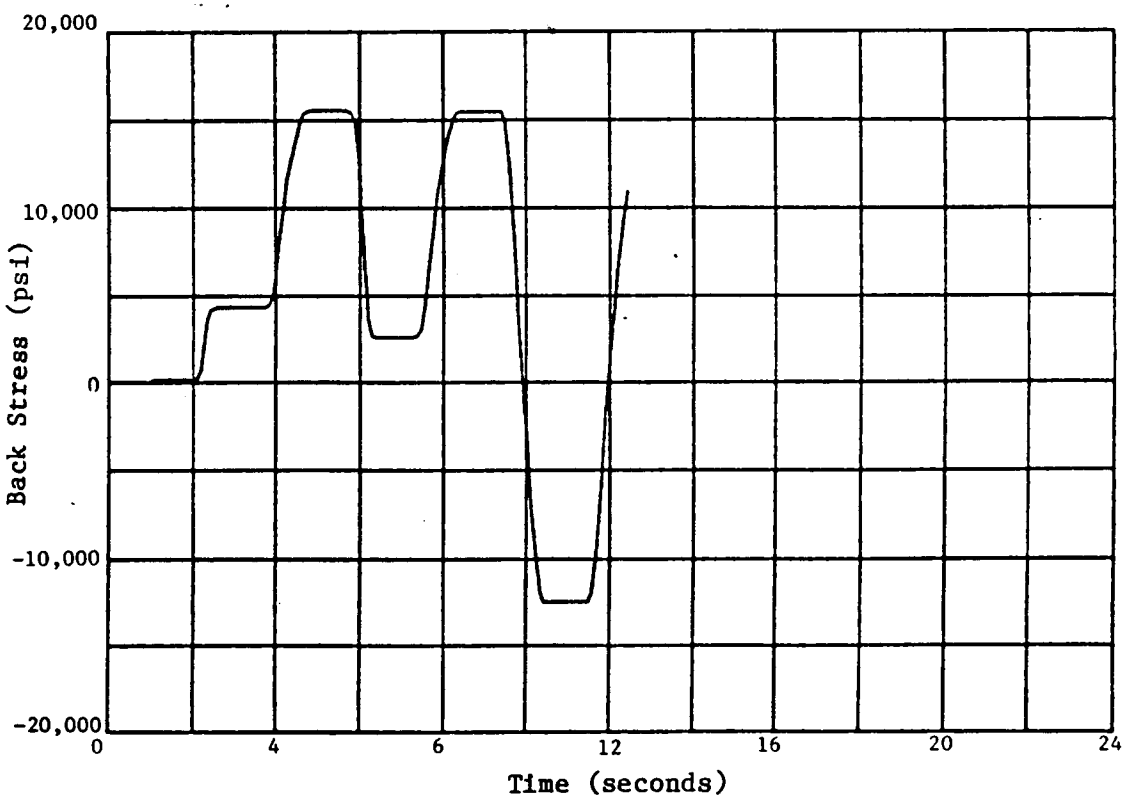

Figure 12. Walker Model, Ramped Cycles - Response of Back Stress.

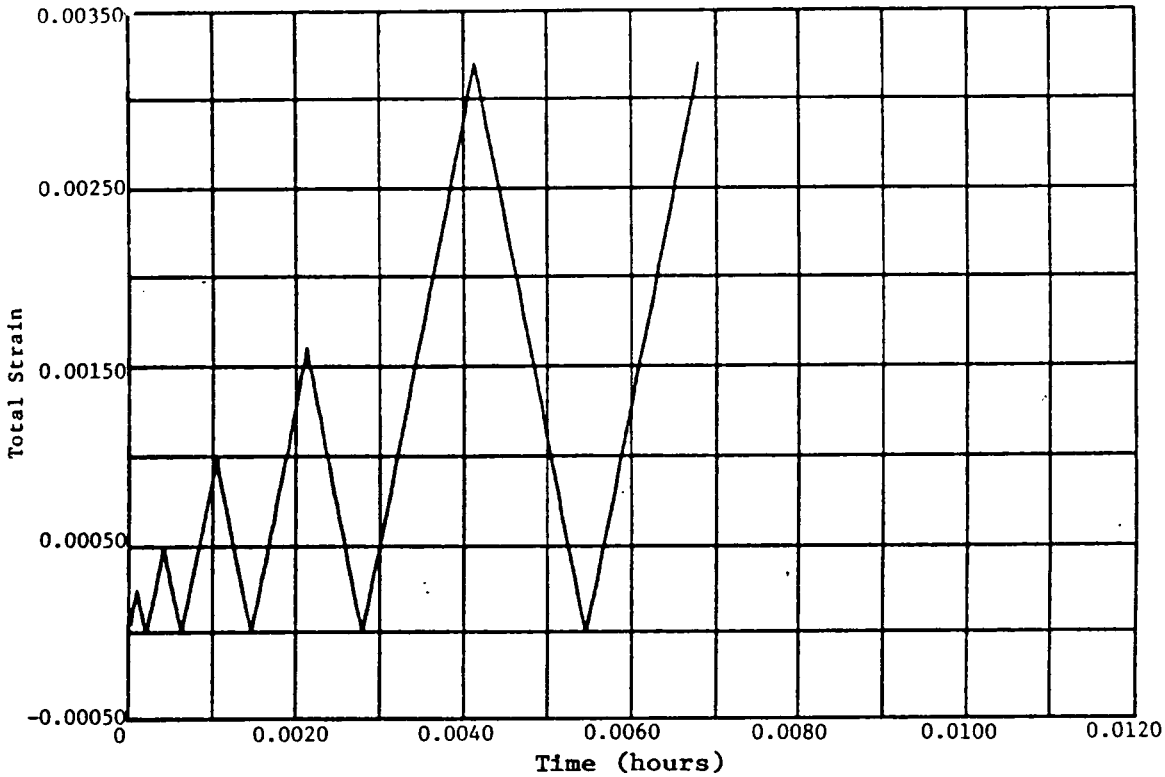

Figure 13. Robinson Model, Ramped Cycles - Cyclic Strain (Control).

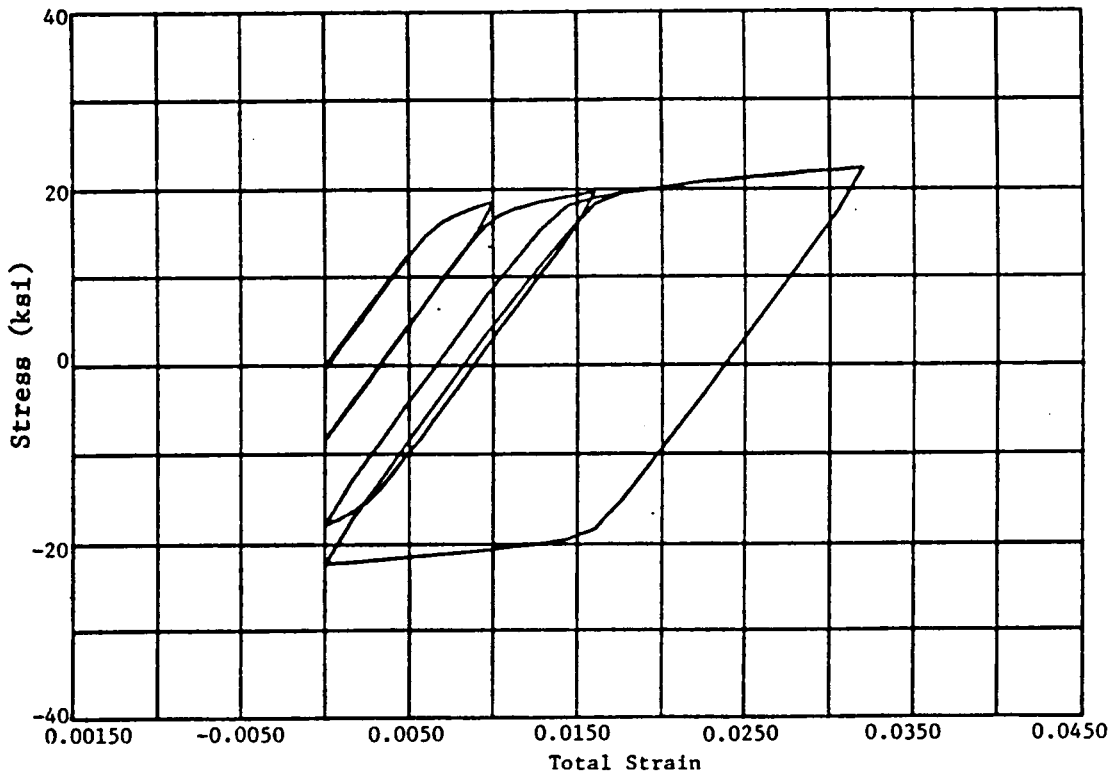

Figure 14. Robinson Model, Ramped Cycles - Cyclic Hysteresis Loops.

2.5 CYCLIC HARDENING AND SOFTENING

Modeling of the cyclic hardening and softening is very important for predicting the life of high temperature alloys. All the models were exercised using completely reversed cycles. It was found that all the models predicted cyclic hardening and that almost all of the hardening occurred during the first cycle. Figure 16 showed the hysteresis loops obtained using the Krieg et al. model at two different strain ranges. Figure 17 shows hysteresis loops for several cycles using the Robinson model. Note that the stress-strain response stabilized after the first cycle. Figure 20 shows a case where stress was relaxed at the peak tensile strain of the cycle. Note the significant amount of relaxation that occurred in the first 60 seconds. Figure 19 shows the same cycling, but with the relaxation occurring at the minimum strain (compressive) of the cycle. Figure 18 shows the same case without any strain hold in the cycle. An examination of the above three cases shows that at the end of the cycle, the stress-strain point at the end of the cycle is the same in each case. This indicates a negligible history effect for this material and this model when large strain ranges are involved.

It has been seen that all the models discussed predicted cyclic hardening for the materials examined. Several materials, such as René 80 and Inconel 718, are known to cyclically soften. In order to ensure that the unified theories are indeed able to predict cyclic softening, the Walker model was exercised with arbitrary modifications of some appropriate material parameters. The material parameters K_2 and N_7 in the Walker model control the evolution of the drag stress. These were arbitrarily given values of -40,000 and 100 respectively, and it was seen that this lowered the drag stress enough to produce cyclic softening. Figure 21 shows the hysteresis loops with cyclic softening. It is possible that the drag stress may control cyclic softening in all the models.

2.6 ANELASTIC (RECOVERY) EFFECTS

Since all the unified constitutive theories feature time dependence, it is useful to examine whether significant anelastic effects can be predicted. A simple way to check this is to load the model into the inelastic regime and unload and hold at the strain corresponding to near zero load. The stress response will then give an indication of anelastic effects. This was done for all the models, and none exhibited any significant anelastic recovery. Figure 22 shows the stress-strain response and the stress-time response using the Krieg model. Note that the stress remains at zero during strain hold after unloading.

2.7 THEORY SELECTIONS

During the course of the detailed evaluations, several generic features of the models became more evident, such as the roles played by the back stress and drag stress. The numerical difficulties involved in using these theories in practical problems also became more apparent. For example, in the theory

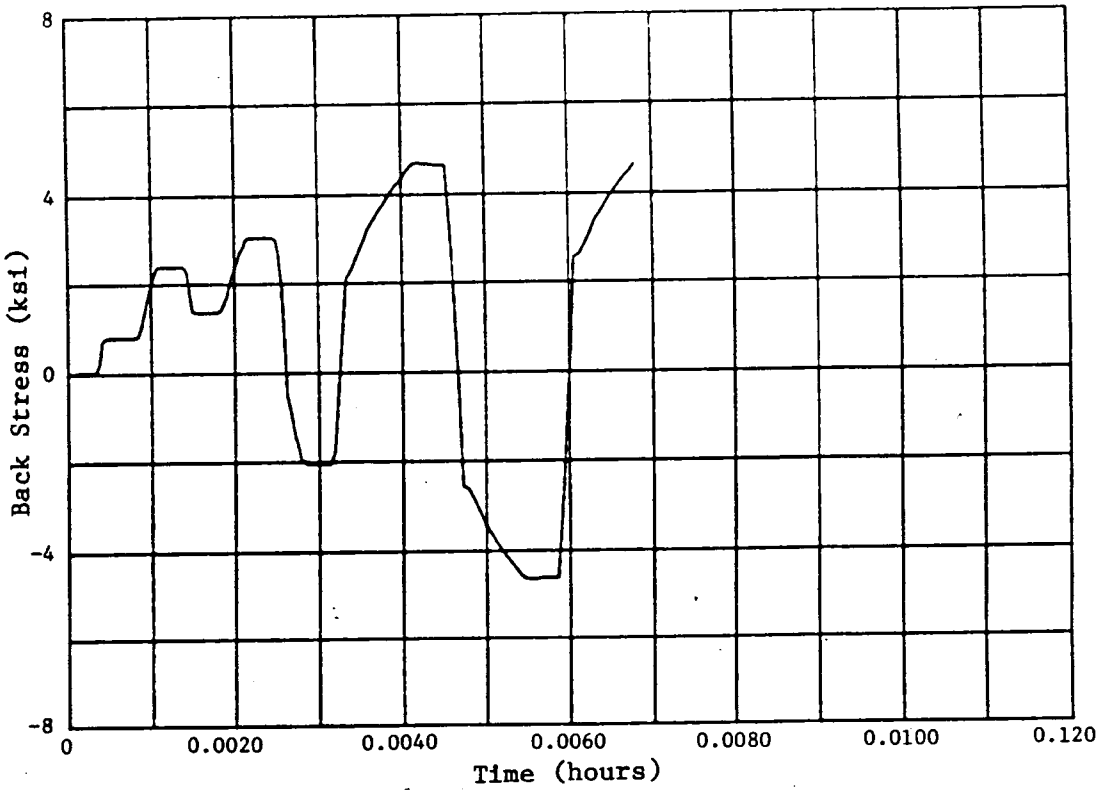

Figure 15. Robinson Model, Ramped Cycles - Response of Back Stress.

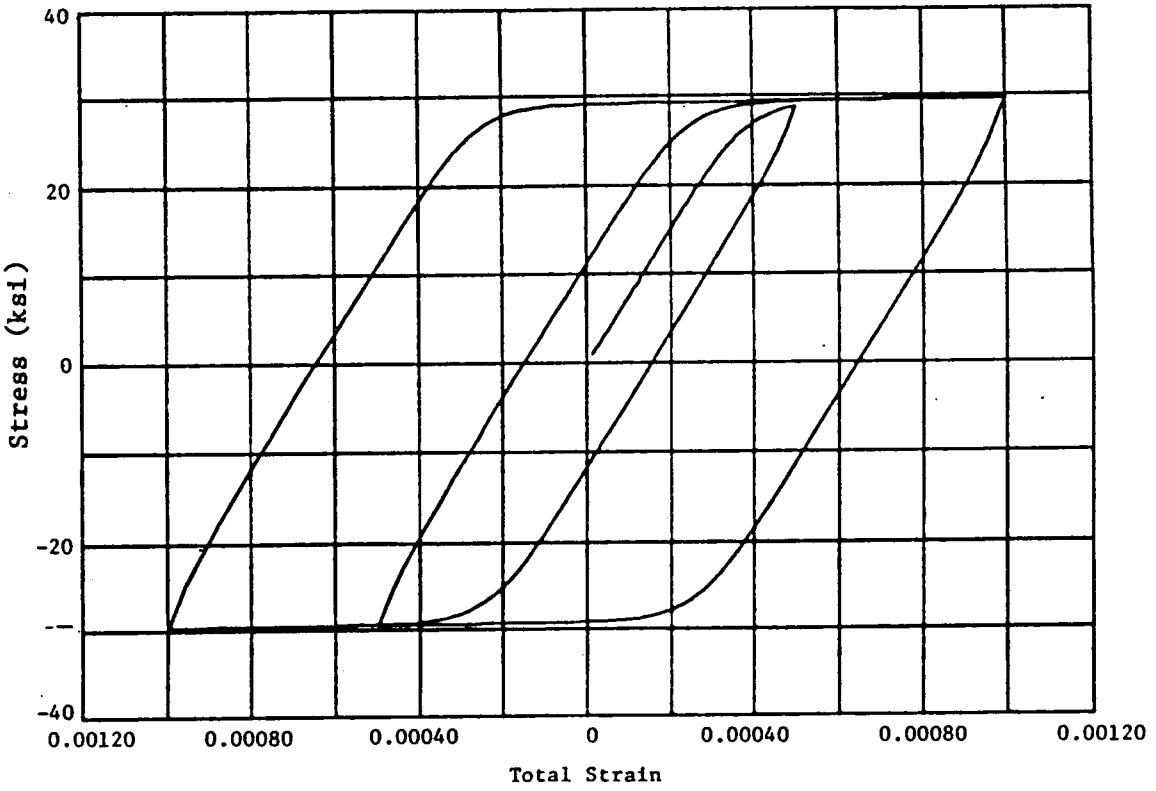

Figure 16. Krieg Model, Cyclic Hysteresis Loops.

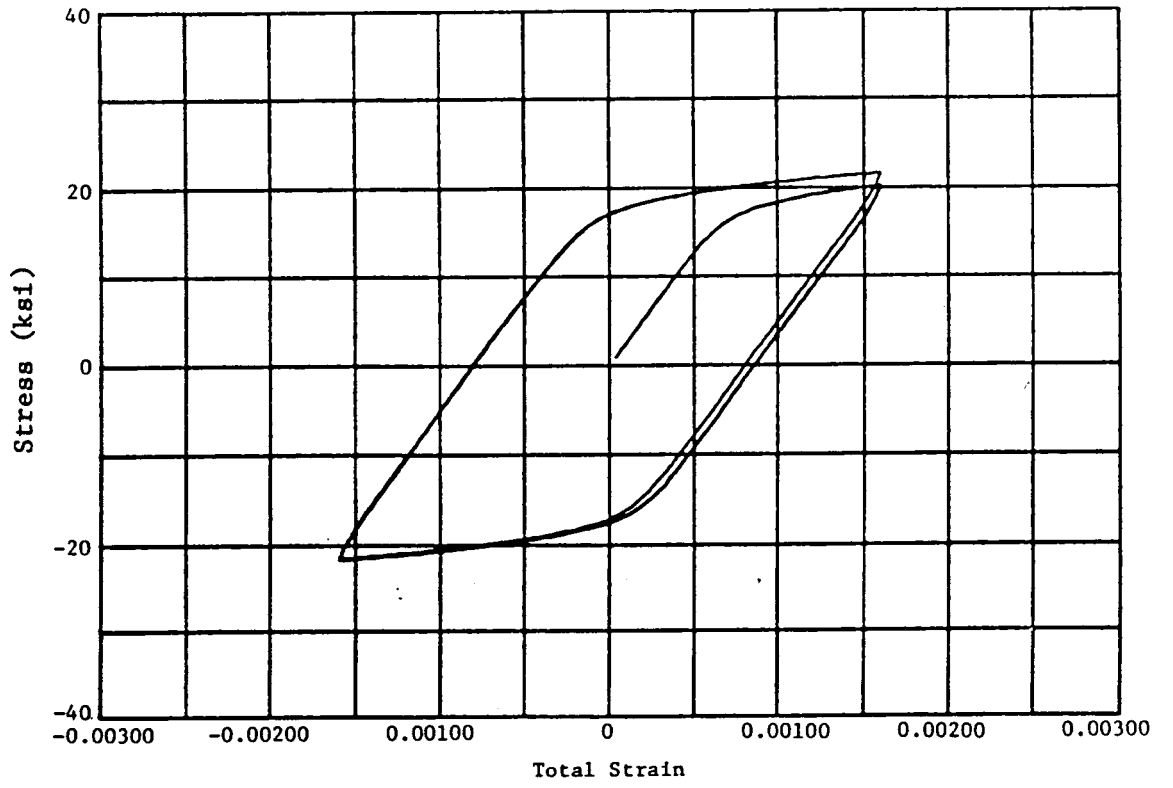

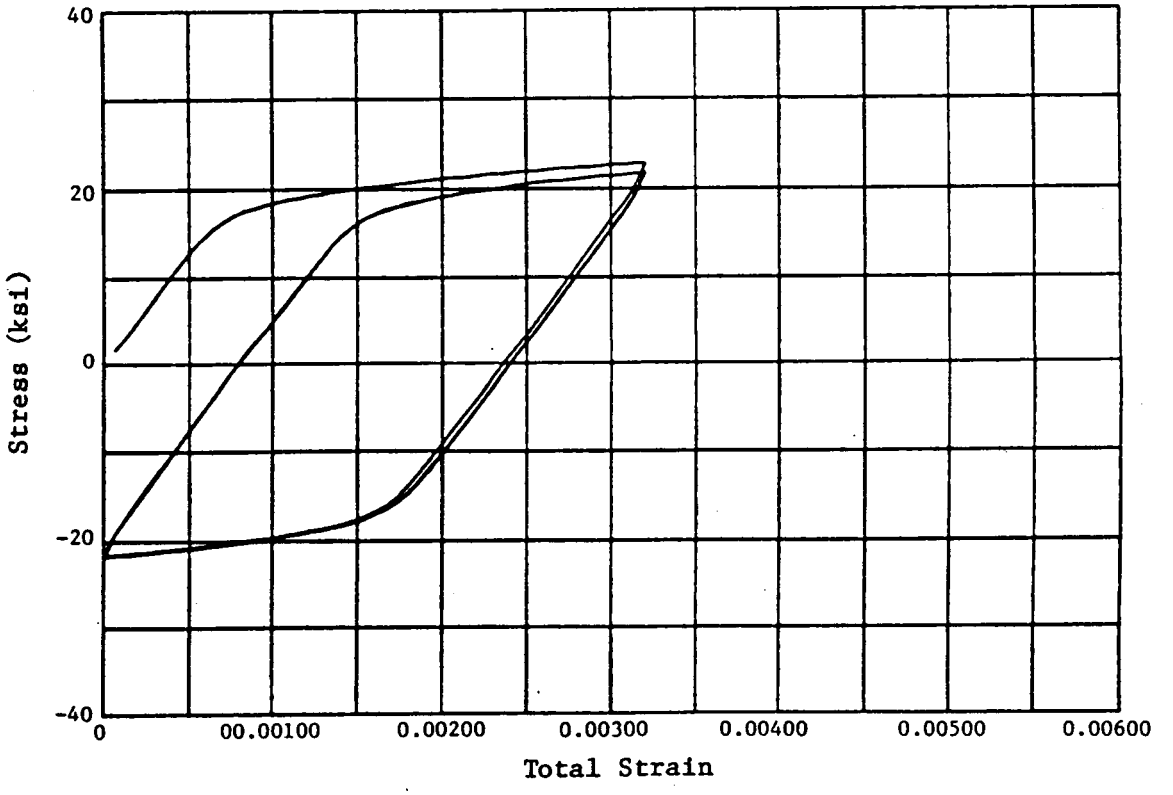

Figure 17. Robinson Model, Cyclic Hysteresis Loops (Two Examples).

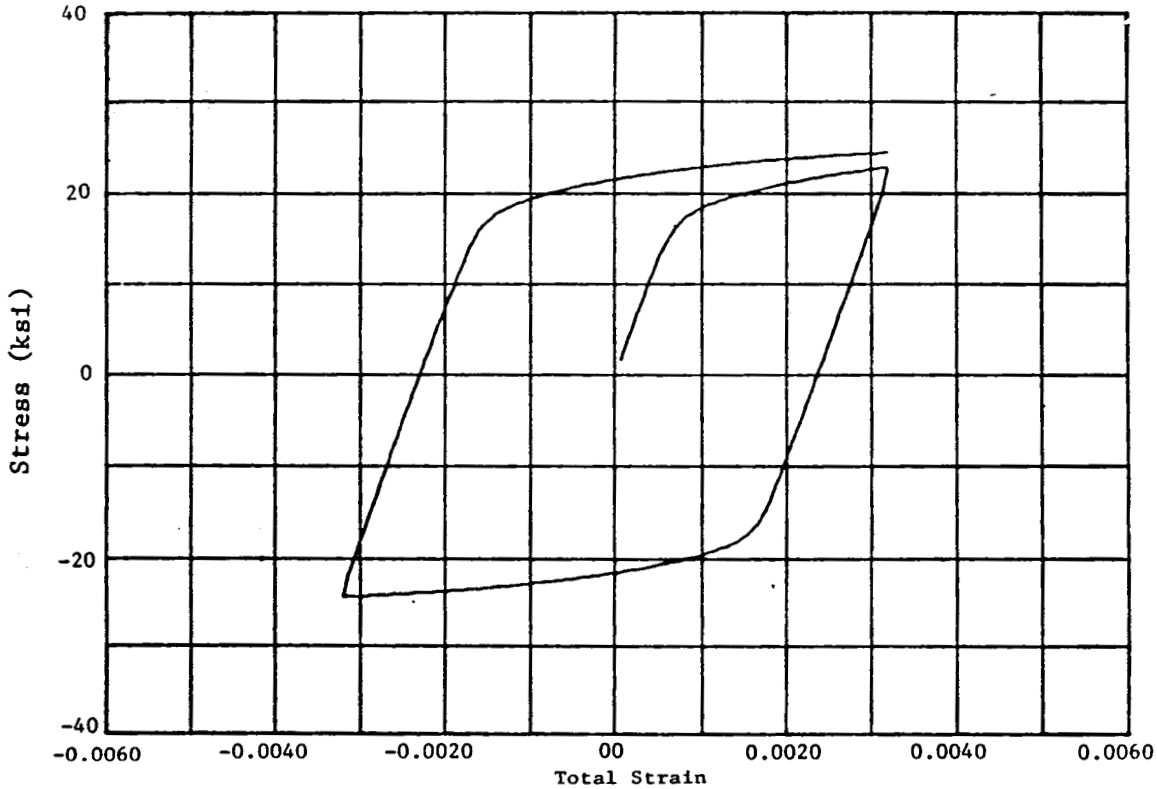

Figure 18. Robinson Model, Cyclic Loading - No Stress Relaxation.

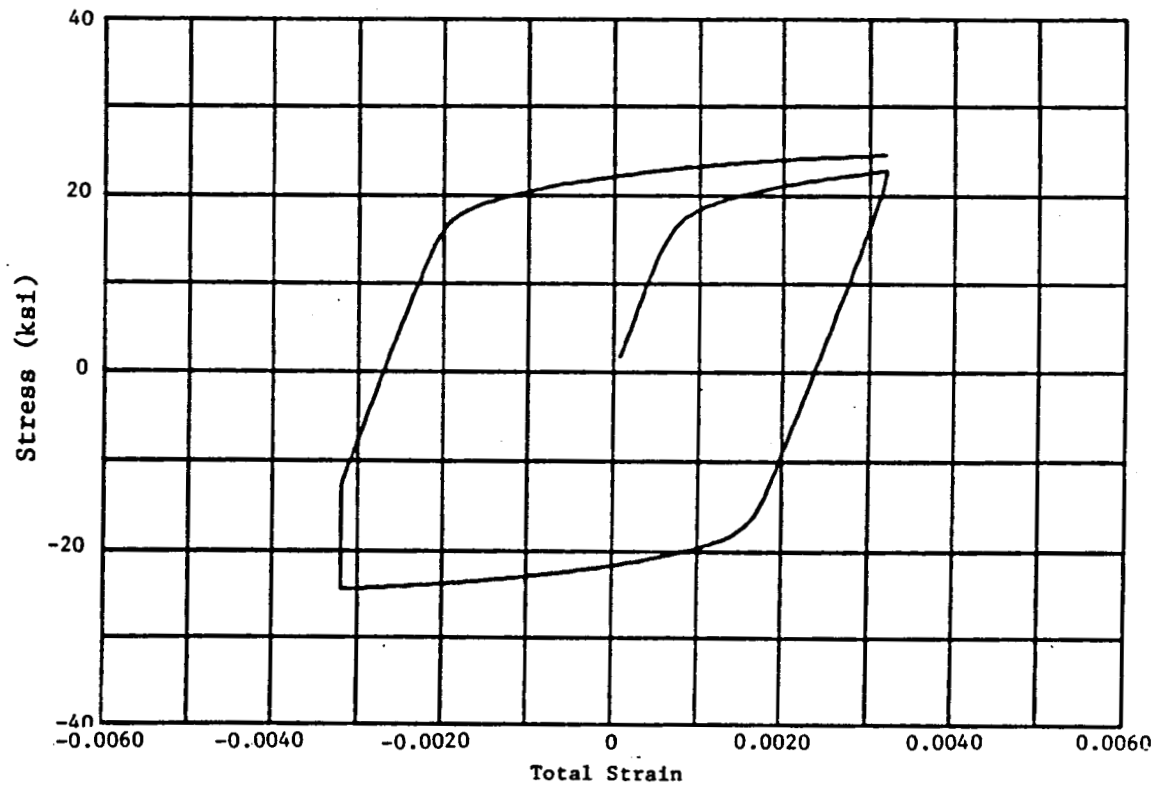

Figure 19. Robinson Model, Cyclic Loading with 1 Min. Hold - Stress Relaxed at Minimum (Compression) Strain.

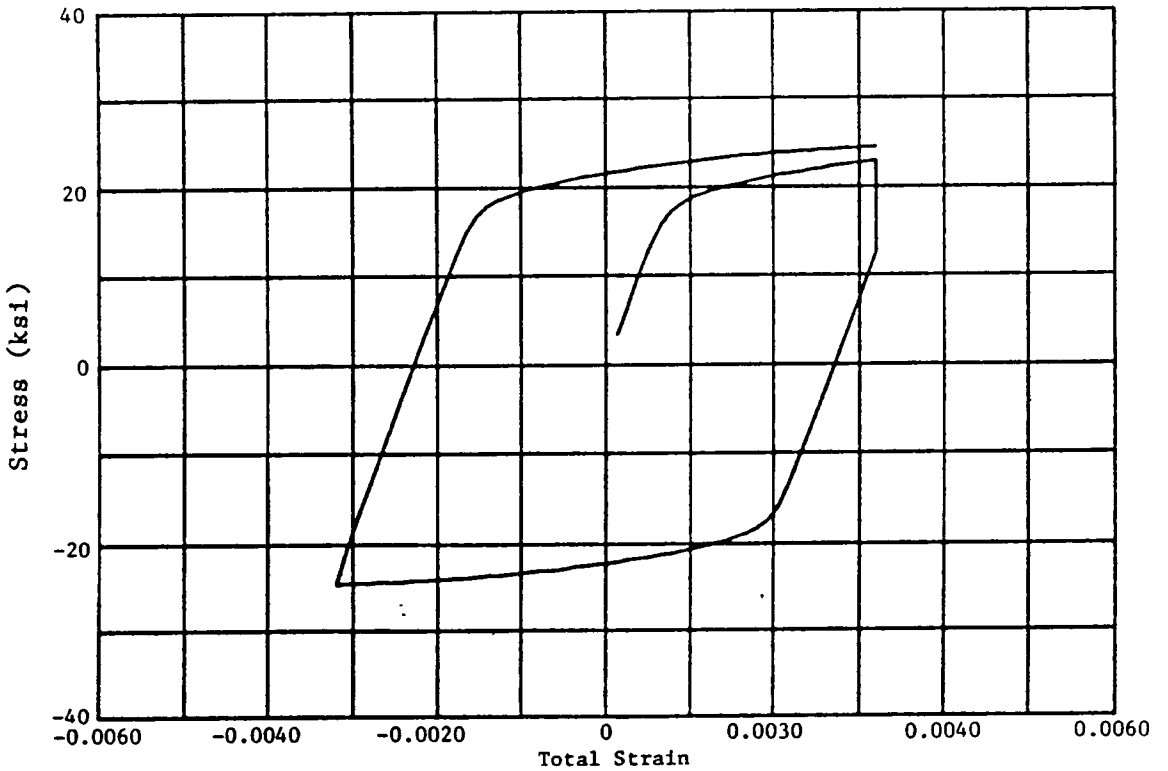

Figure 20. Robinson Model, Cyclic Loading with 1 Min. Hold - Stress Relaxed at Maximum (Tensile) Strain.

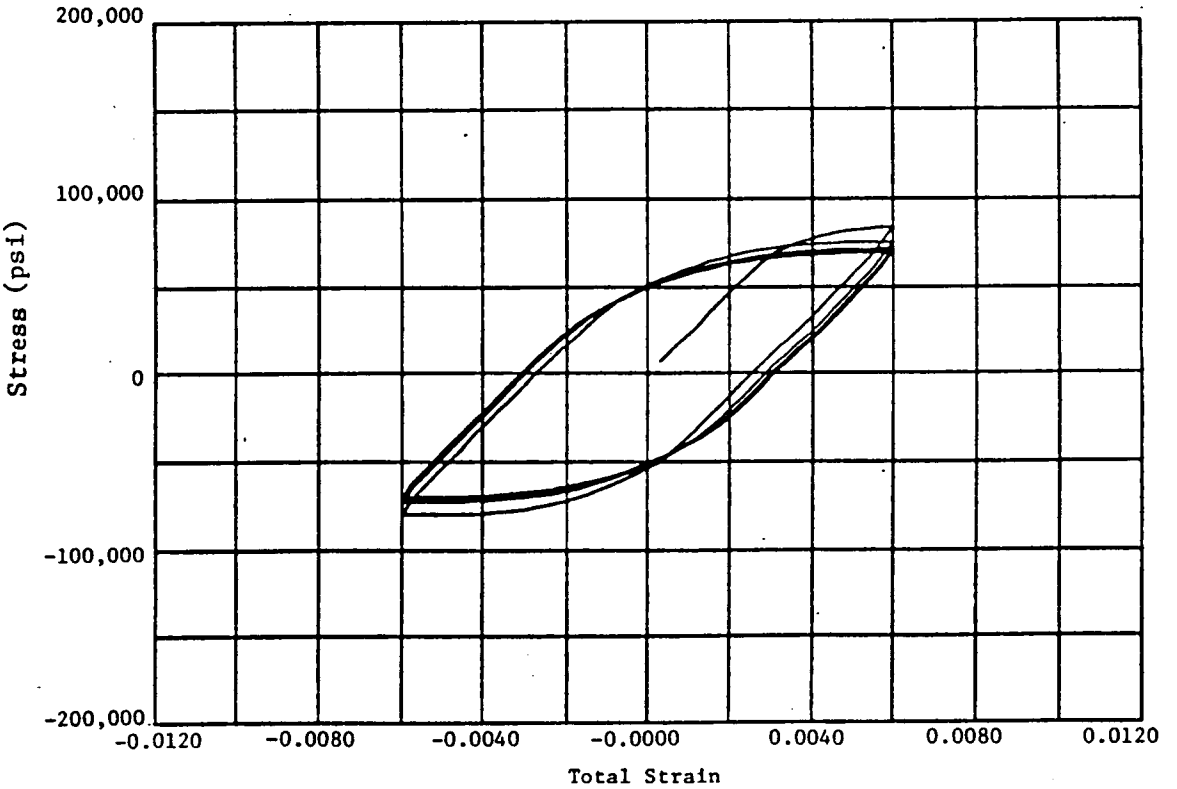

Figure 21. Walker Model, Cyclic Softening K2 = -40000, N7 = 100.

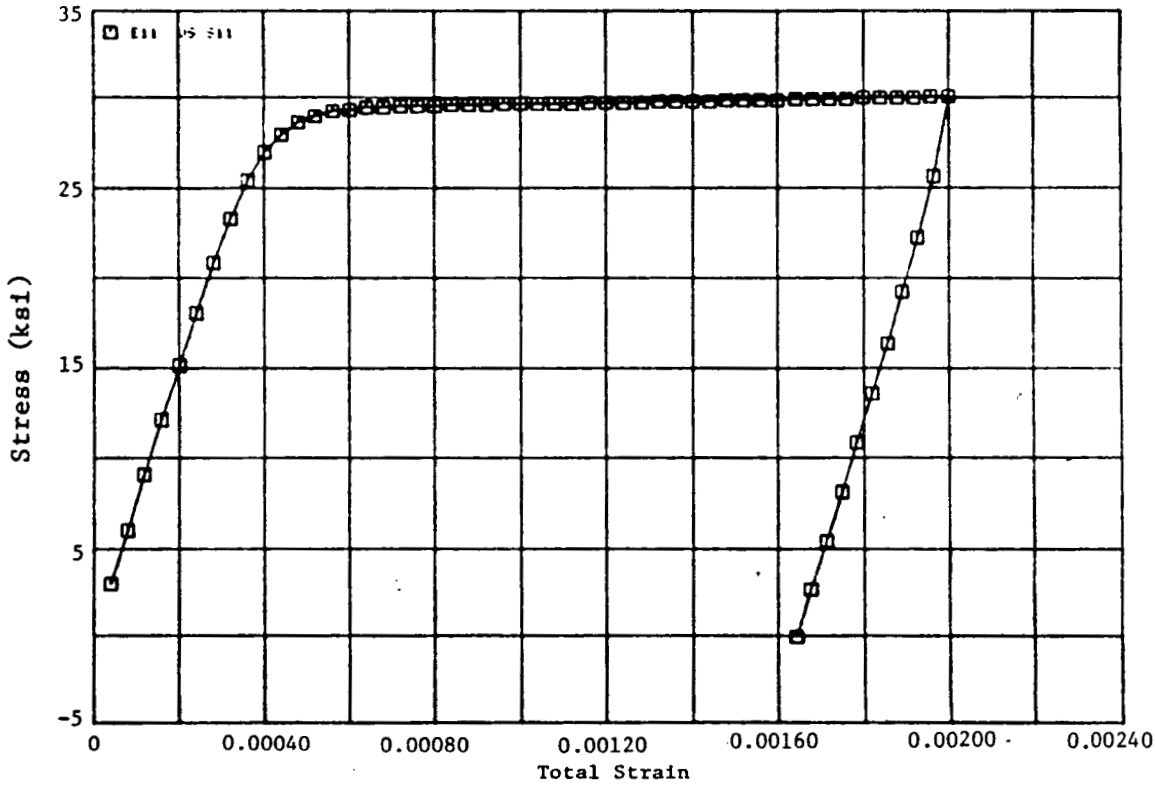

(a) Stress-Strain Response.

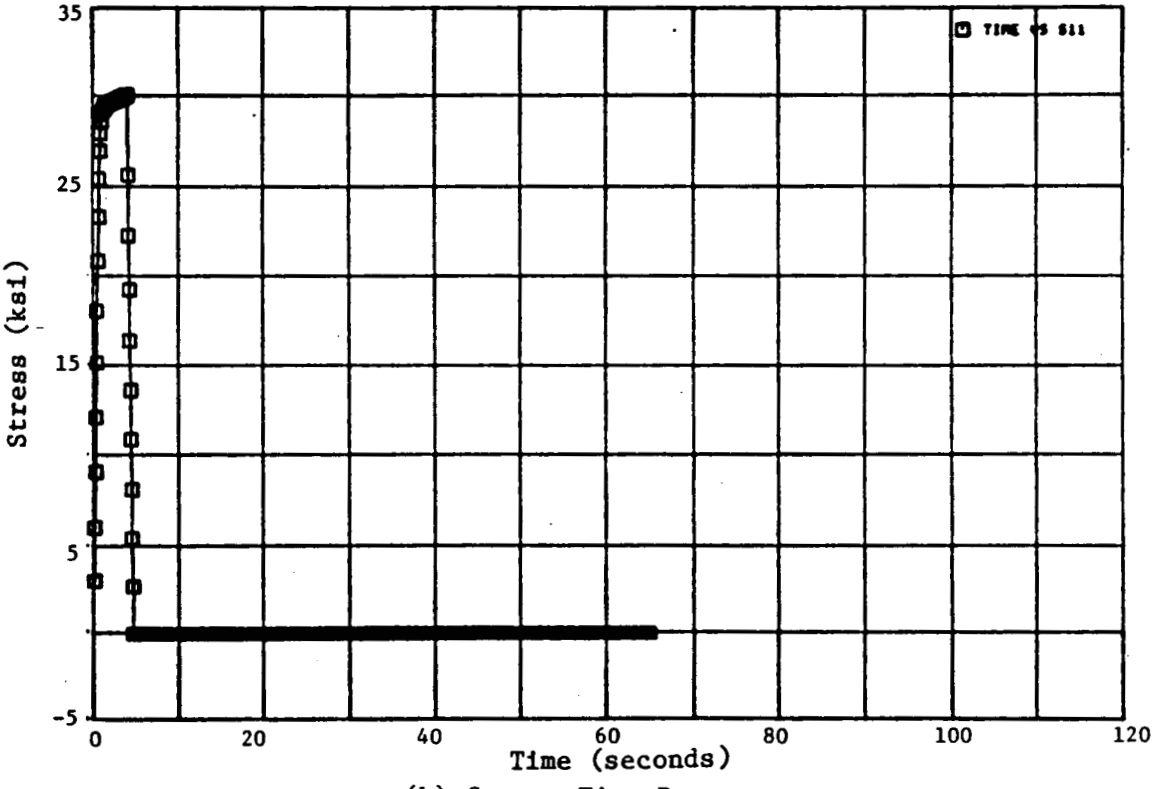

(b) Stress-Time Response.

Figure 22. Krieg Model Anelasticity.

of Miller (which uses three sinh functions) the numerical difficulties are particularly severe. The inequalities involved in Robinson's model are a potential source of problems, as mentioned previously. The Bodner model has the advantage of simplicity without involving several different material parameters. This model was, therefore, selected for further use in the program. The second choice was what is referred to as a generic drag stress/back stress model. The general formulations of the other four models will be used but the selection of the specific functional forms for the flow rule and the evolutionary equations will be deferred. The final selection of the specific mathematical formulations will be made through detailed evaluations of the baseline René 80 data. Thus, the second selected model was a hybrid that includes preferred elements of the other four models.

3.0 MATERIAL SELECTION, EXPERIMENTAL PLAN, AND SPECIMEN DESIGN

This section of this report describes the experimental plan for Tasks B, C, E, and F. In this investigation, conventionally cast Rene 80 was chosen as the base material because of its frequent use in aircraft engine blade applications, and because its thin wall properties have been extensively evaluated (References 16 and 17). The thin wall properties are important because the thin sections of turbine blades experience the largest temperature/stress gradients, Reference 18, and because some elevated temperature properties are diminished with reduced wall size (References 16 and 17). For these two reasons, and since the information from this contract is to be used to predict the stress distribution in blades, all the Rene 80 test specimens were designed with a nominal wall thickness of 0.03 inch. The test specimens were cast as solid bars and machined to final dimensions. This was done so that the measured material properties would not include the effects of surface or microstructural heterogeneities associated with cast-to-size specimens.

3.1 MATERIAL PROCESSING

The René 80 material used in this program was 3.5-inch-diameter remelt stock cast by Howmet Turbine Components Corporation, Alloy Division. The certified composition of this material is compared to the alloy composition specification in Table I. All analyses meet this composition specification.

The remelt stock was cast into cylinders by the Metals Division of TRW, Inc. Two sizes of cylinders were cast. The smaller ones were approximately 0.5 inch in diameter by 4 inches long and were used for tensile, creep, cyclic, and notched axisymmetric testing. The larger specimen blanks were approximately 1.125 inches in diameter by 6 inches long and were used for tension-torsion and benchmark testing. All the specimen blanks were investment cast in MgO. Care was taken so that both sizes of castings would have similar grain size.

Twenty-four small specimens were cast at one time. The individual blanks were cast in a vertical position, in two concentric rings, with each ring containing twelve specimens. A total of three heats was cast to obtain 56 specimen blanks procurred for this program. TRW personnel noted that the specimens from the outer ring may have a slightly finer grain size than those from the inner ring. A specimen distribution plan was developed so that specimens for tensile, creep, smooth cyclic, and notched cyclic properties were evenly distributed among the three heats and ring (outer versus inner) positions.

The large specimen blanks (1.125-inch diameter by 6-inch long) were also investment cast in vertical position. Each heat contained six blanks in a single ring. A total of seven heats was cast to get the 24 required specimens. A specimen distribution plan was developed so that the axial-torsion and benchmark specimens would be evenly distributed among the six heats.

Table I. Composition of René 80.

Element	Specification	Certified Analysis
C	0.15–0.14	0.17
Mn	0.10 Max.	0.01
Si	0.10 Max.	0.02
S	0.0075 Max.	0.002
P	0.015 Max.	0.009
Cr	13.70–14.30	14.06
Ti	4.80–5.0	4.87
B	0.01–0.12	0.015
Al	2.8–3.2	3.05
W	3.70–4.30	4.00
Mg	3.70–4.30	4.06
W+Mo	7.70 Min.	8.06
Co	9.00–10.00	9.55
Zr	0.02–0.10	0.03
Fe	0.03 Max.	0.07
Cb	0.10 Max.	0.01
Ta	0.10 Max.	0.02
V	0.10 Max.	0.01
Cu	0.10 Max.	0.01
Hf	0.10 Max.	0.01
Mg	0.10 Max.	0.0032
Ni	Balance	Balance

Each specimen blank successfully passed an x-ray inspection at the casting vendor.

The specimen blanks were then heat treated at General Electric. The standard Rene 80 heat treatment, comprising four steps, was followed:

1. 2200° F/2 hrs; cool to 2000° F within 10 min; cool to room temperature.

2. 2000° F/4 hrs; cool to 1200° F within 6 min; cool to room temperature.

3. 1925° F/8 hrs; cool to 1200° F within 30 min; cool to room temperature.

4. 1550° F/16 hrs; cool to room temperature.

3.2 TEST SPECIMENS

There are three basic types of tests used in this investigation - uniaxial (Task C), multiaxial (Task E), and benchmark verification (Task F). Figure 23 shows the uniaxial tubular thin wall specimen which was used for all uniaxial experiments. Figure 24 shows the tubular, thin wall notched specimen used in the multiaxial evaluations. The notch, shown in Figure 24, was designed based on elastic finite element analysis and has a ratio of 0.35 between the maximum and minimum principal stresses. This is believed to be adequate for the evaluation of the constitutive relationships developed in this program. The notch geometry was also designed to facilitate use of the interferometric strain gage (ISG, References 19 through 21) during the test. Figure 25 shows a drawing of the hollow axial-torsion specimen used in the multiaxial evaluations. This specimen has a larger gage length and inside diameter than the specimen shown in Figure 23 in order to give more accurate test data in the axial-torsion tests. Figure 26 shows the geometry of the benchmark specimen. This is identical to the specimen analyzed and verified by Domas, et al. (Reference 21) except that the specimen thickness was reduced to 0.030 inch, consistent with the other specimens used in this program.

3.3 UNIAXIAL TEST MATRIX (TASK C)

During this task, tensile/stress relaxation, creep, and cyclic tests were conducted. Table II shows the test matrix of the tensile tests. Tests were performed at a strain rate of 0.02 min^{-1} (baseline) at temperatures from 537° to 980° C (1000° to 1800° F) in 111° C (200° F increments.) At both 1000° and 1800° F the tensile properties were evaluated at strain rates an order of magnitude higher and lower than the baseline strain rate. These temperatures were selected to determine the influence of temperature on strain rate sensitivities. The tension tests were performed using closed loop testing equipment to assure proper strain rate control. Most of these tests were terminated after a strain of 0.015. (It was planned to stop the

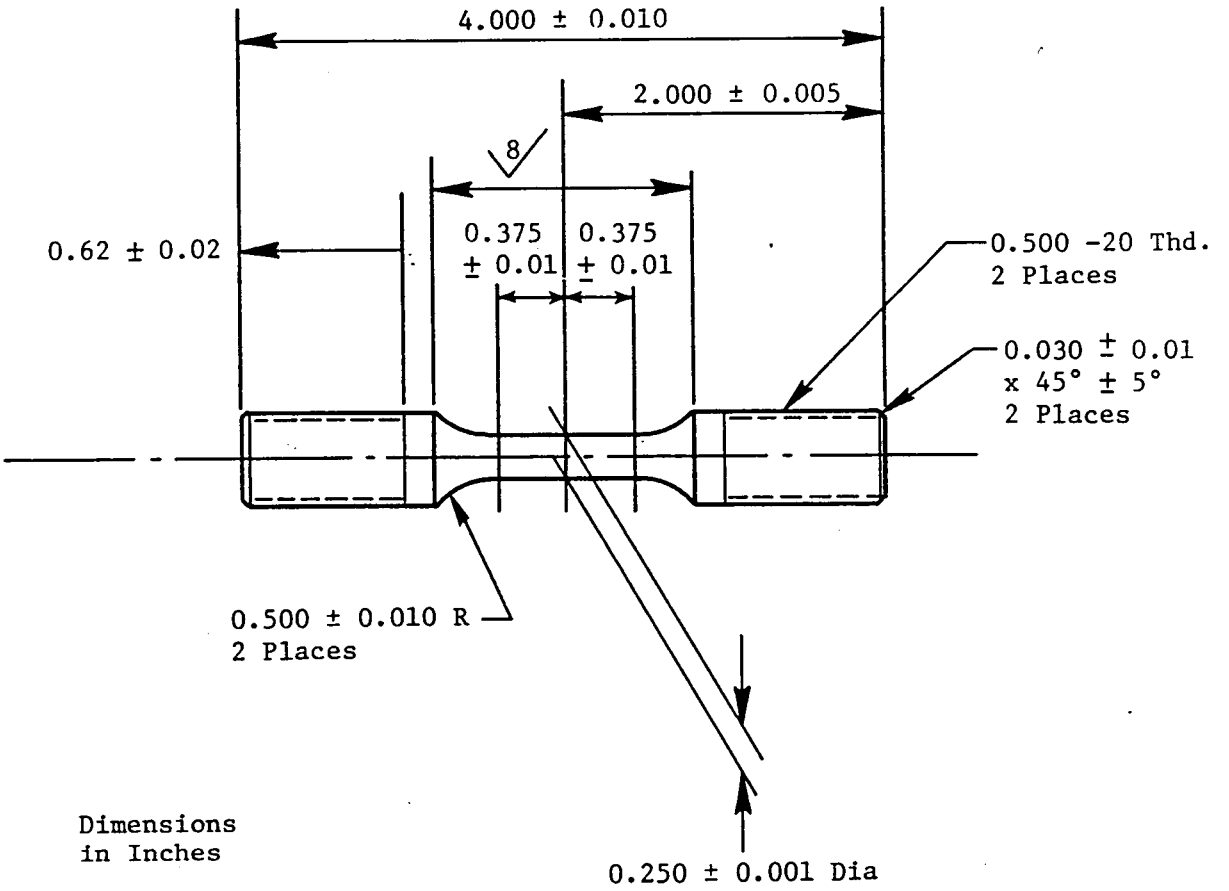

Figure 23. Uniaxial Thin Wall Test Specimen.

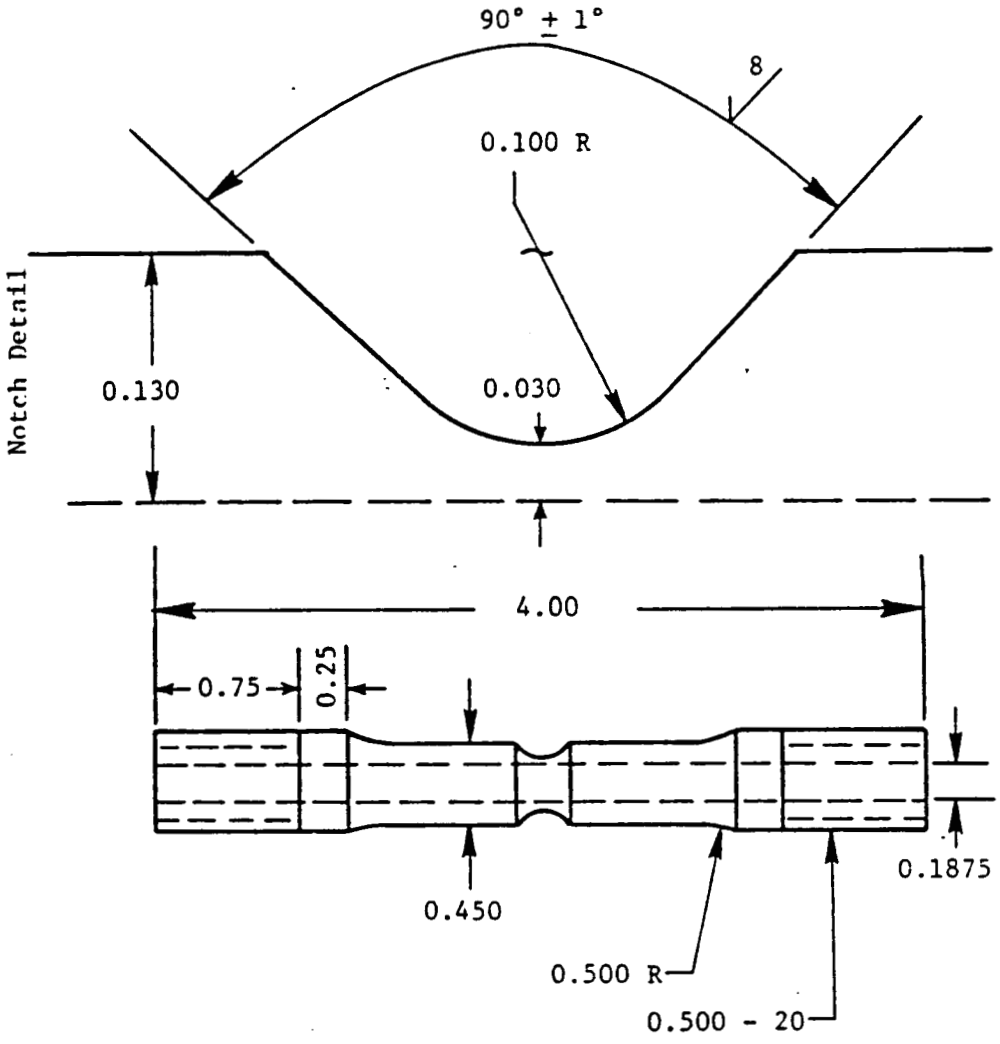

Figure 24. Axisymetric, Notched Thin Wall Test Specimen.

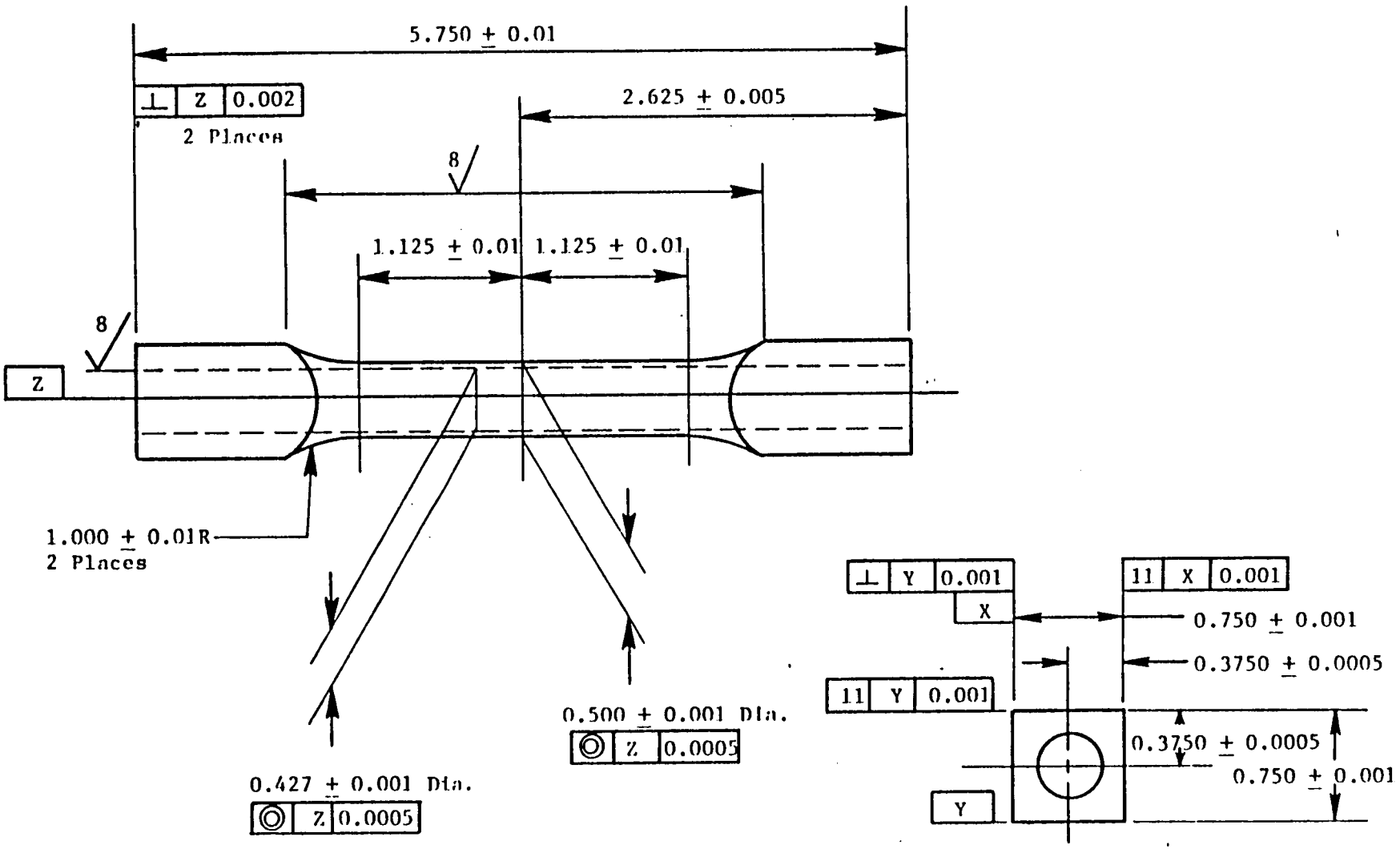

Figure 25. Axial-Torsion Thin Wall Test Specimen.

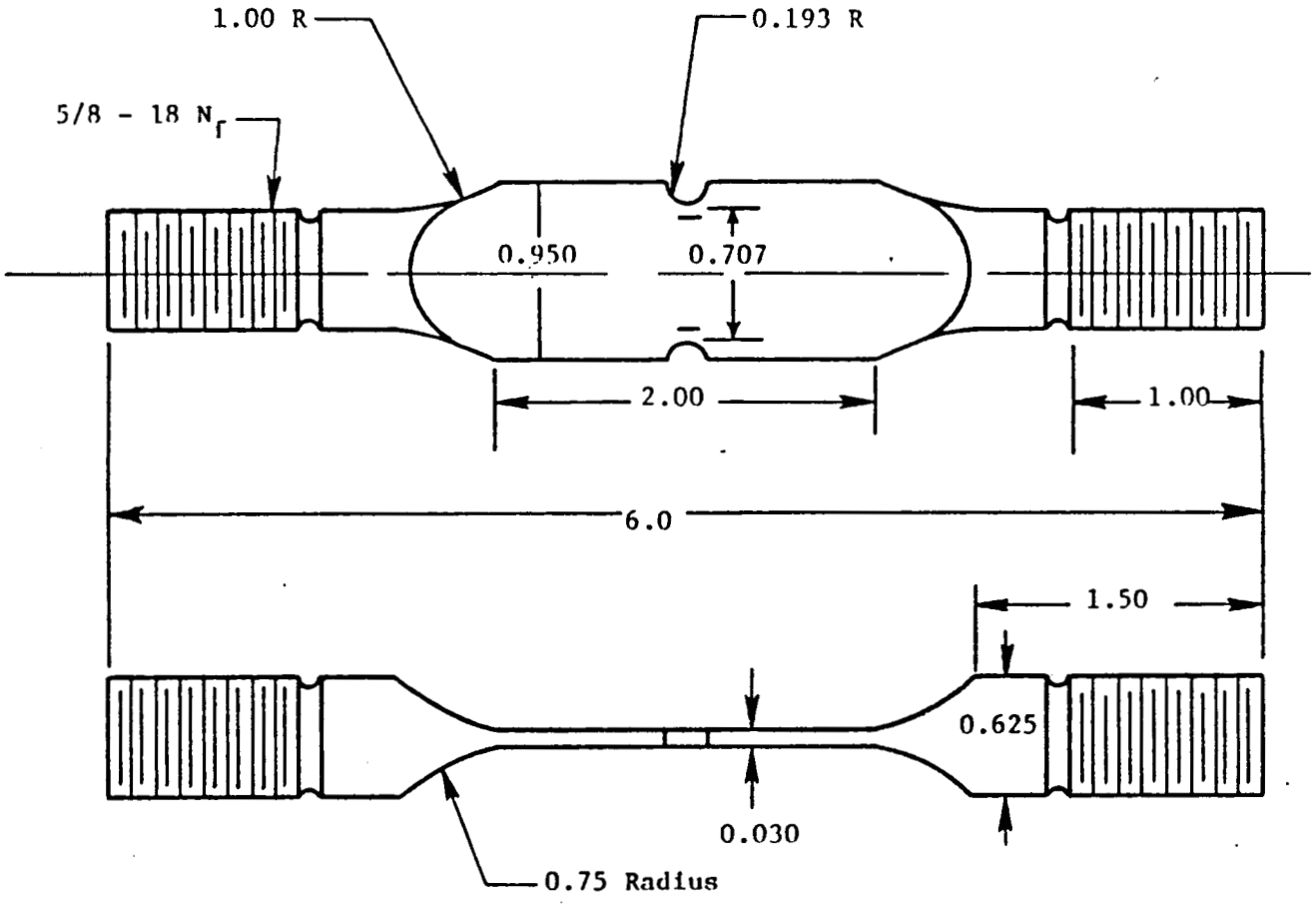

Figure 26. Thin Wall Benchmark Notch Specimen (K_t = 1.9).

straining of several of the early tests at 0.03; however, the specimens failed at lesser strains. For that reason, the termination strain was reduced to 0.015.) After this strain level was reached, the strain was maintained for the tests with baseline, higher, and lower strain rates at 1800° F for approximately 24 hours.

Table III shows the test matrix for the ten monotonic creep tests. These tests were terminated after a nonelastic strain of 0.01 or a time less than 1,500 hours. These tests were done using closed-loop testing equipment to maintain good specimen alignment.

The matrix for the first uniaxial cyclic tests consists of 30 tests. The intent of the first 20 tests was to furnish input for the constitutive model; the other 10 tests (not yet completed) will be used to verify the predictions of the selected constitutive models. It is anticipated that the last 10 tests will include additional monotonic and isothermal cycling along with thermal mechanical fatigue tests.

All cyclic specimens were tested in strain control in closed loop testing machines at a constant value of A_ε (alternating strain/mean strain). These tests were performed using the constant strain amplitude block sequence technique with ε_{max} (for $A_\varepsilon = 1$ and $A_\varepsilon = \infty$) or $|\varepsilon_{min}|$ (for $A_\varepsilon = -1$) values of 0.0015, 0.0030, and 0.0045. Each testing block contained about 20 cycles. The ε_{max} or $|\varepsilon_{min}|$ was increased for each of the first three blocks; then the sequence of strain ranges was modified to look for transient behavior occurring with sudden increasing and decreasing strain ranges. The test temperatures were 1400°, 1600°, and 1800° F to cover the range of temperatures where strain rate of sensitivity is more severe. The strain rates ($\dot{\varepsilon}$) were selected to cover the range anticipated during airfoil mission cycles.

In Table IV, the uniaxial cyclic test matrix is divided into three sections: continuously cycled with $\varepsilon = 0.2$/min, continuously cycled with $\varepsilon = 0.002$/min, and hold-time tests at $\varepsilon = 0.2$/min. An A_ε ratio of ∞ (totally reversed strain cycling) was used as the baseline for the continuously-cycled tests and all hold-time tests. This A_ε was used for both strain rates at all three temperatures.

The other six continuously cycled tests were conducted with A of either +1 or -1. At 1600° and 1800° F, tests with $A_\varepsilon = -1$ were performed; the 1400° F tests included both $A_\varepsilon = +1$ and -1. The rationale for this selection is based on the predictions of McKnight, et al. (Reference 18) of strain levels in advanced airfoils. At lower temperatures the mean strains are positive, while at higher temperatures the mean strains are negative. The influence of strain rate was evaluated at 1600° and 1800° F, where higher strain rate sensitivity was observed.

Table II. Tensile Specimen Test Matrix.

Test Temperature °F (°C)	Strain Rate, min^{-1} 0.002	0.02	0.2
1000 (537)	T	T + SR	T + SR
1200 (650)		T + SR	
1400 (760)		T + SR	
1600 (870)		T + SR	
1800 (980)	T + SR	T + ST	T + SR

T Indicates a constant strain rate tension test terminated at a strain of 0.03.

SR is a stress relaxation test to be performed at a constant strain 0.03.

Table III. Creep Specimen Test Matrix.

Test Temperature, °F (°C)	Initial Applied Stress Levels, ksi
1400 (760)	80.3, 92.0, 99.3
1600 (870)	45.3, 60.0, 71.5
1800 (980)	16.0, 31.5, 43.5
2000 (1093)	16.6

The eight hold-time tests shown in Table IV were strain controlled tests with a strain rate of 0.2 min^{-1} and fully reversed cycling ($A_\varepsilon = \infty$). Hold times of 12 and 120 seconds were used. Because of the mission cycle considerations mentioned above, the 1400° F tests were done with hold times at both minimum and maximum strain, and the 1800° F tests received a hold at compressive strains. The 1600° F tests were done with hold times at maximum strains.

The data reduction methods and the results of these tests are presented in Section 4.0 of this report.

3.4 MULTIAXIAL TEST MATRIX (TASK E)

This experimental portion of this program used both notched axisymmetric (Figure 24) and axial-torsion specimens (Figure 25). The intent of these tests is to experimentally verify the predictions of the selected constitutive models. The notched axisymmetric tests will be performed at Michigan State University using the ISG technique (References 19-21) and the tension-torsion tests will be conducted at General Electric's Turbine Technology Laboratory. (It has been experimentally verified that the ISG technique will work at 1600° F if the specimen has a vapor-deposited gold-palladium coating. This prevents extensive oxidation from obliterating the microhardness indentations.) The notched axisymmetric test matrix is shown in Table V. The first and second tests are a tension/stress relaxation and a creep test. These will be identical to those performed in Task C except that these will be notched specimens.

The cyclic tests on notched axisymmetric specimens listed in Table V will be performed in remote strain control under totally reversed ($A_\varepsilon = \infty$) conditions. The remote strain limits will be those which result in maximum longitudinal strain levels on the notch root of 0.0015, 0.0030, and 0.0045 under monotonic loading. The four cyclic tests will be performed at two strain rates under continuously cycled conditions, and with 120-second holds at maximum and minimum strains.

Table VI lists the test matrix for the evaluation using axial torsion specimens (Figure 25). They will be tested at 1600° F and 1800° F under combined axial and torsional strain control. Several tests will receive no axial strain with the remainder being in-phase or out-of-phase cycling. In-phase cycling has proportional axial-torsional straining while out-of-phase cycling has non-proportional loading. At each temperature, two torsional tests, four continuously cycled tests, and one hold time test will be performed. One of these continuously cycled tests has a shift in axial strain.

Table IV. Uniaxial Cyclic Specimen Test Matrix.

a) Continuously Cycled

	Temperature, °F		
	1400	1600	1800
	A_ε	A_ε	A_ε
$\dot{\varepsilon}$ = 0.2/min	∞ +1 -1	∞ -1	∞ -1
$\dot{\varepsilon}$ = 0.002/min	∞	∞	∞

b) Hold Time: $A_\varepsilon = \infty$, $\dot{\varepsilon}$ = 0.2/min

	Temperature, °F		
	1400	1600	1800
Hold Times	12 Sec Max 12 Sec Min 120 Sec Max 120 Sec Min	12 Sec Max 120 Sec Max	12 Sec Min 120 Sec Min

Table V. Axisymmetric Notched Specimen Test Matrix.

(1600° F)

Tensile = 0.02 min^{-1}; Stress Relaxation After = 0.03

Fatigue (ε, $\varepsilon_{n_{max}}$ = 0.0015, 0.0030, 0.0045, Remote Strain Control)

Strain Rate $\dot{\varepsilon}_n$, min^{-1}	A_ε	Test Description
0.02	∞	Continuously Cycled
0.002	∞	Continuously Cycled
0.002	-1	Continuously Cycled
0.02	∞	Minimum Strain 120 Sec. Hold

Table VI. Test Matrix for Axial-Torsion Tests.

Temperature (I)	Test Type	$\dot{\varepsilon}$ (1/min.)	$A_{e_{xy}}$	In- or Out-of-Phase	Comment
	Torsion	0.02			
		0.002			
1600° F	Axial-Torsion	0.02	∞	In	
		0.002	∞	In	
		0.02	∞	In	120 sec hold at ε_{max}
		0.002	∞	Out	
		0.002	∞	Out	ε_{xx} shift = 0.0015
	Torsion	0.02			
		0.002			
1800° F		0.02	∞	In	
		0.002	∞	In	
		0.02	∞	In	120 sec. hold at at ε_{min}
		0.002	∞	Out	
		0.002	∞	Out	ε_{xx} shift = -0.0015

An axial-torsion extensometer has been designed for use in these experiments. A new design was needed because most available axial-torsion extensometers were too heavy for these thin-walled specimens. This design, shown in Figure 27, consists of two annular rings contacting the specimen with spring loaded, pointed quartz rods. From one of these rings an arm extends parallel to the axis of the specimen; this arm acts as a target for the separate axial and torsion displacent measurements. These measurements will be made using high temperature capacitive displacement gages.

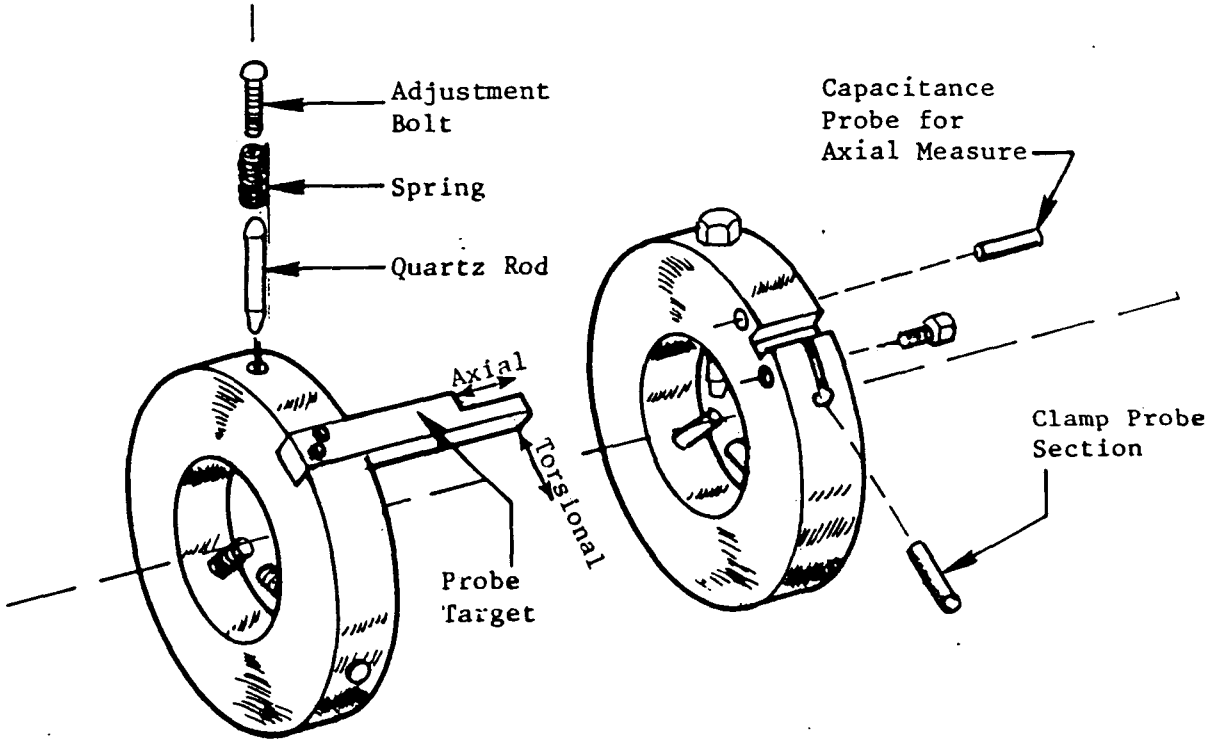

Figure 27. Axial-Torsion Extensometer

All test specimens for the multiaxial evaluation have been machined but testing has not yet begun.

3.5 BENCHMARK NOTCH VERIFICATION EXPERIMENTS (TASK F)

The benchmark test specimens (Figure 26) must be tested in load control with positive loads. (Compressive loads would buckle these 0.03-inch-thick specimens.) An elastic-plastic finite element analysis was made to determine if reversed plasticity could be obtained at the notch root under positive load

cycling. The analysis was performed using CYANIDE, a code developed by General Electric for rapid, inexpensive finite element analysis. A two-dimensional finite element grid that consists of constant-strain triangular elements (Figure 28) was used. Four load cases were analyzed wherein the remote boundary was loaded with a uniform stress. The cyclic stress strain curve used in this analysis was reported by McKnight et al. (Reference 9). Only four load cases were needed to determine if reversed plasticity occurred at the notch root. In subsequent analyses more load cases will be used. An elastic analysis matched the K_t value for this specimen reported by Domas et al. (Reference 21).

Figure 29 shows the stress-total strain results at the notch root and at the edge of the mesh where loads are applied. The longitudinal stresses and strains are reported where the longitudinal direction is parallel to the loading axis. As one would expect, the stresses in the notch root are much larger than those calculated at the remote location. Upon unloading the specimen to zero load, the stresses at the notch root are compressive. The data shown in this figure are connected by straight lines, so it is difficult to determine if reversed plasticity occurred. Figure 30 shows the longitudinal stress plotted against longitudinal plastic strain. For that case, unloading showed no change in the remote plastic strain, but at the notch root, the plastic strain diminished by approximately 0.0009 upon unloading. This demonstrates that this specimen can be tested using positive load cycling to obtain reversed notch root plasticity. This reversal is great enough for accurate experimental measurement and control.

All the benchmark specimens have been machined but testing has not started.

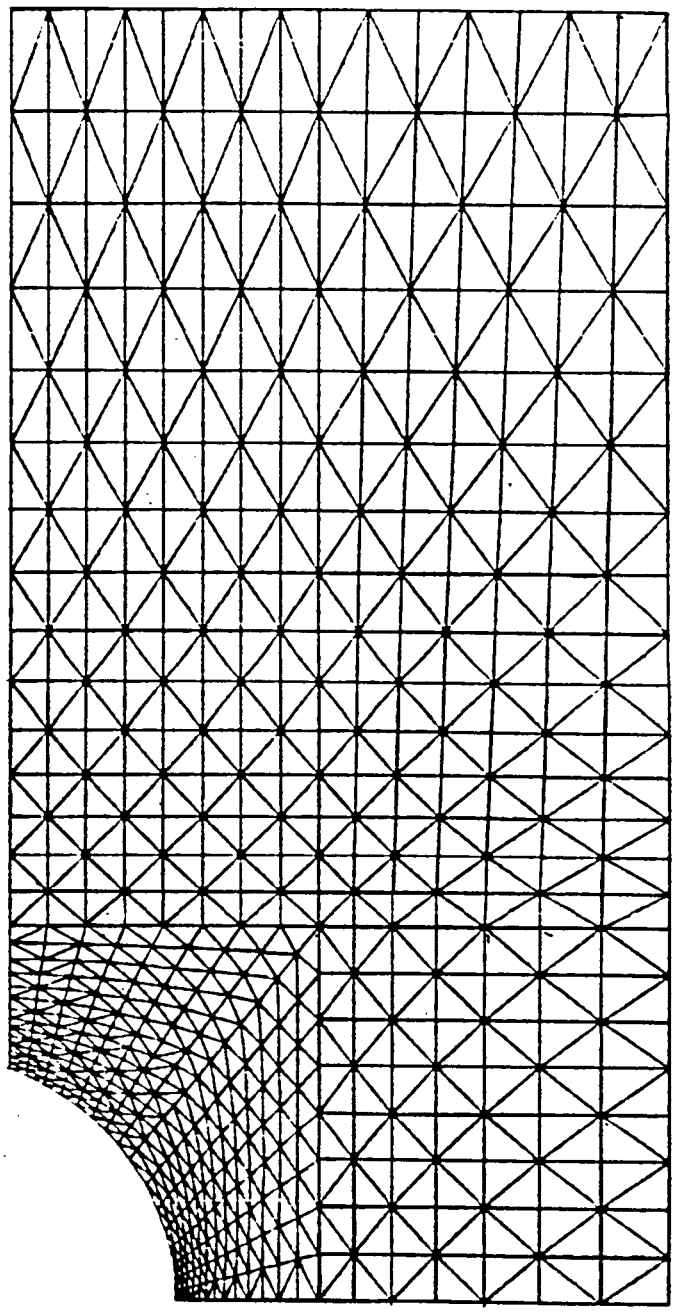

Figure 28. Finite Element Mesh of the Benchmark Notch Specimen Using Quarter Symmetry.

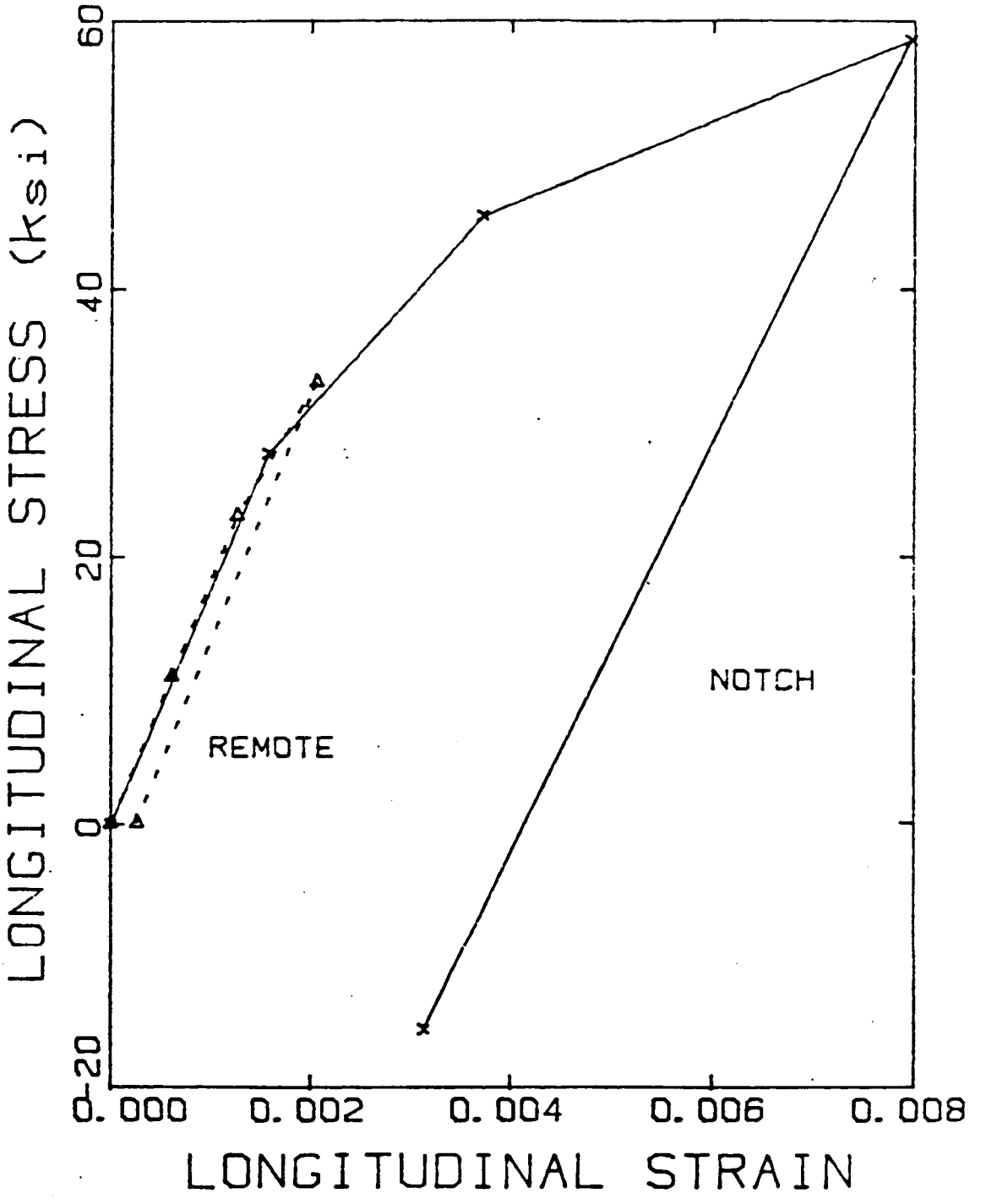

Figure 29. Stress-Total Strain Results at the Notch Root and Grid Edge.

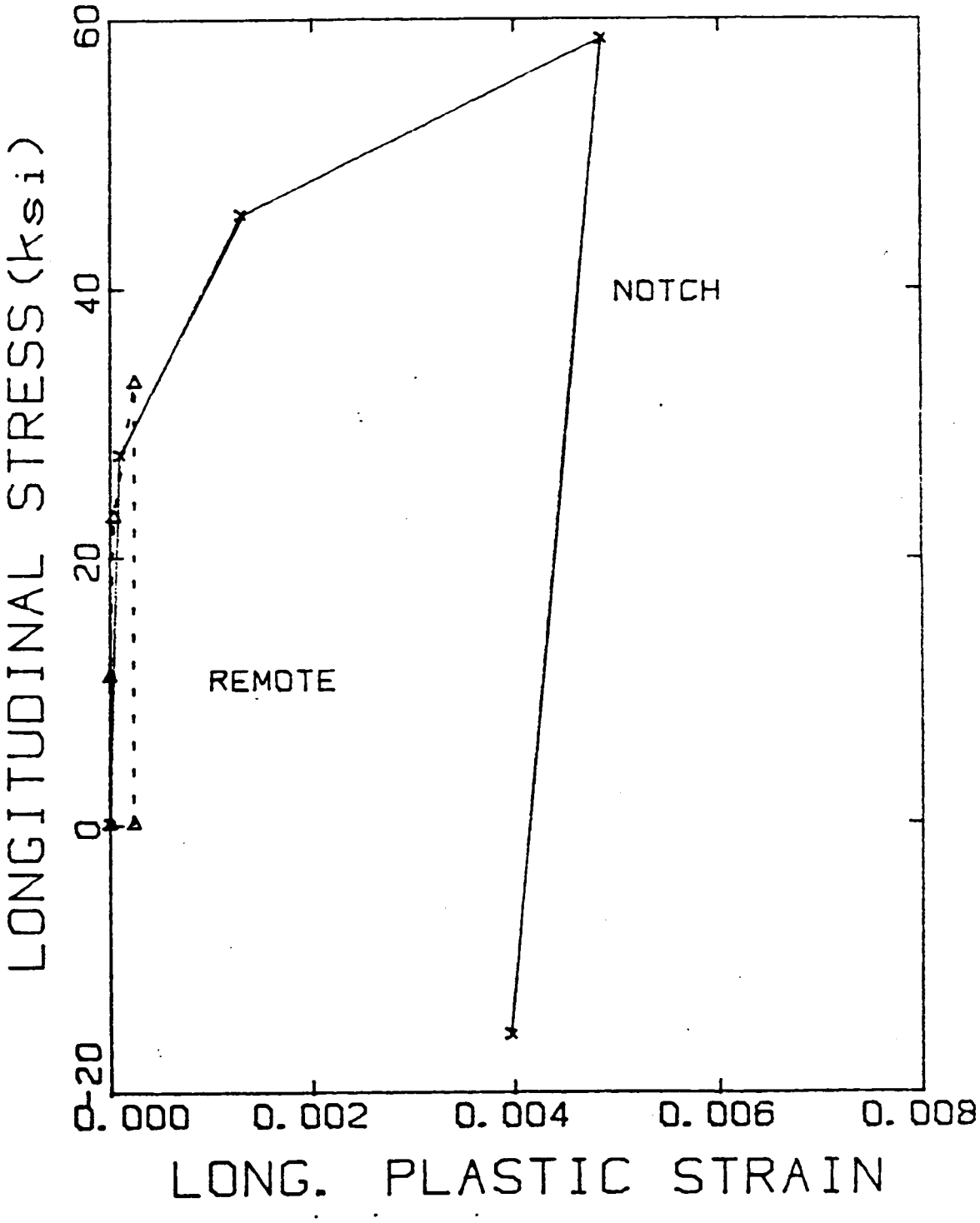

Figure 30. Longitudinal Stress Versus Longitudinal Plastic Strain.

4.0 UNIAXIAL EXPERIMENTS

All of the tensile, creep, and the first 20 cyclic tests have been completed. The tensile and creep test data were recorded autographically on X-Y recorders and strip charts. These data were digitized for data analysis.

The cyclic data were obtained with an automated test control and data acquisition system manufactured by Engineering Technical Services of Champaign, Illinois. The load and extensometer outputs were determined with a resolution of 5mV, where the full scale signal was 10V. For a typical test in this program, the resolutions for stress and strain were 1.4 MPa and 0.00002, respectively.

The cyclic tests were conducted in blocks of constant alternating strain range ($(\varepsilon_{max} - \varepsilon_{min})/2$). Table VII lists the sequence of the cycling blocks for these tests. This sequence was designed to determine the influence of strain cycling history on the constitutive response, During Blocks 1 through 7, the alternating strain range of 0.15, 0.3, and 0.45% was studied along with every possible transition between. The purpose of Block 8 was to determine the material response when the drag and back stress terms in the constitutive relationships are ideally fully saturated.

Table VII. Sequence of Alternating Strain Range in Cyclic Tests.

Test Block	Alternating Strain Range
1	0.0015
2	0.0030
3	0.0045
4	0.0030
5	0.0015
6	0.0045
7	0.0015
8	0.0100

The data acquisition system recorded approximately 200 data points per hysteresis loop. Data were determined for the first three cycles at the beginning of each strain range block. After that, the loop data were acquired every other cycle. This approach caused two minor difficulties: at rapid strain rates, there was a small period of time between the first three cycles of each block where the strain rate was zero. This period, on the order of milliseconds, was the time needed to transfer the data from a buffer to

storage. A look at the load-displacement plots showed that this had negligible influence on the hysteresis loops. The second difficulty was that the data obtained from every other cycle did not start precisely at the beginning of a cycle (strain = 0 for $A_\varepsilon = \infty$). This was resolved in the analysis software. Both these problems were considered minor and of negligible consequence to this investigation.

4.1 DATA ANALYSIS

The purpose of the data analysis was to reduce the experimental data to basic properties (σ, ε, ε^I_E) as well as the first temporal derivative properties ($\dot{\sigma}$, $\dot{\varepsilon}$, and $\dot{\varepsilon}^I_E$). Software was constructed to do this automatically. The data reduction has three basic phases - calculation of stress and total strain from load, displacement, and specimen geometries; determination of elastic modulus and calculation of ε^I_E and calculation of the derivative properties.

All stresses and strains in this report are engineering (and not true) stresses and strains. The error associated with this restriction is less than 1% and makes the results consistent with finite element calculations.

Figure 31 shows the data from the first cycle of a 980° C (1800° F) cyclic test on a hollow axisymmetric specimen of René 80. This cycle had an alternating strain range of 0.15% and a strain rate of 0.02/min (0.0033/sec). These data have the appearance of a well-behaved hysteresis loop. Young's modulus was calculated by performing a linear regression between stress and strain. Software was developed to use the data between zero and some specified stress on the loading portion of a cycle. Visual examination of the hysteresis loop suggested that the proportional limit was approximately 20 ksi. An elastic modulus was calculated in this fashion and used to calculate inelastic strains. With this modulus, negative inelastic strains were frequently noted at strains between 0 and 20 ksi during the initial loading, suggesting tht yielding had already occurred at 20 ksi. As a result, modulus calculations were performed as a function of limiting maximum stress. Figure 32 shows the resulting modulus lines for limiting stresses of 69, 103.5, and 138 mPa (10, 15, and 20 ksi). As the limiting stress is lowered, the modulus is increased. For a limiting stress of 69 mPa (10 ksi), there was little systematic trend of negative inelastic strains.

The question remains as to whether the modulus calculated with a limiting stress of 69 mPa is the actual modulus, especially at load reversals. Figure 33 shows the elastic modulus lines (based on a limiting stress of 69 mPa) for three cases - initial loading, load reversal at maximum strain, and load reversal at minimum strain. For all three cases, this appears to be a representative modulus line. On this basis, the limiting stress was chosen to be half of the estimated proportional limit. This modulus value was used for calculating ε^I for the entire test.

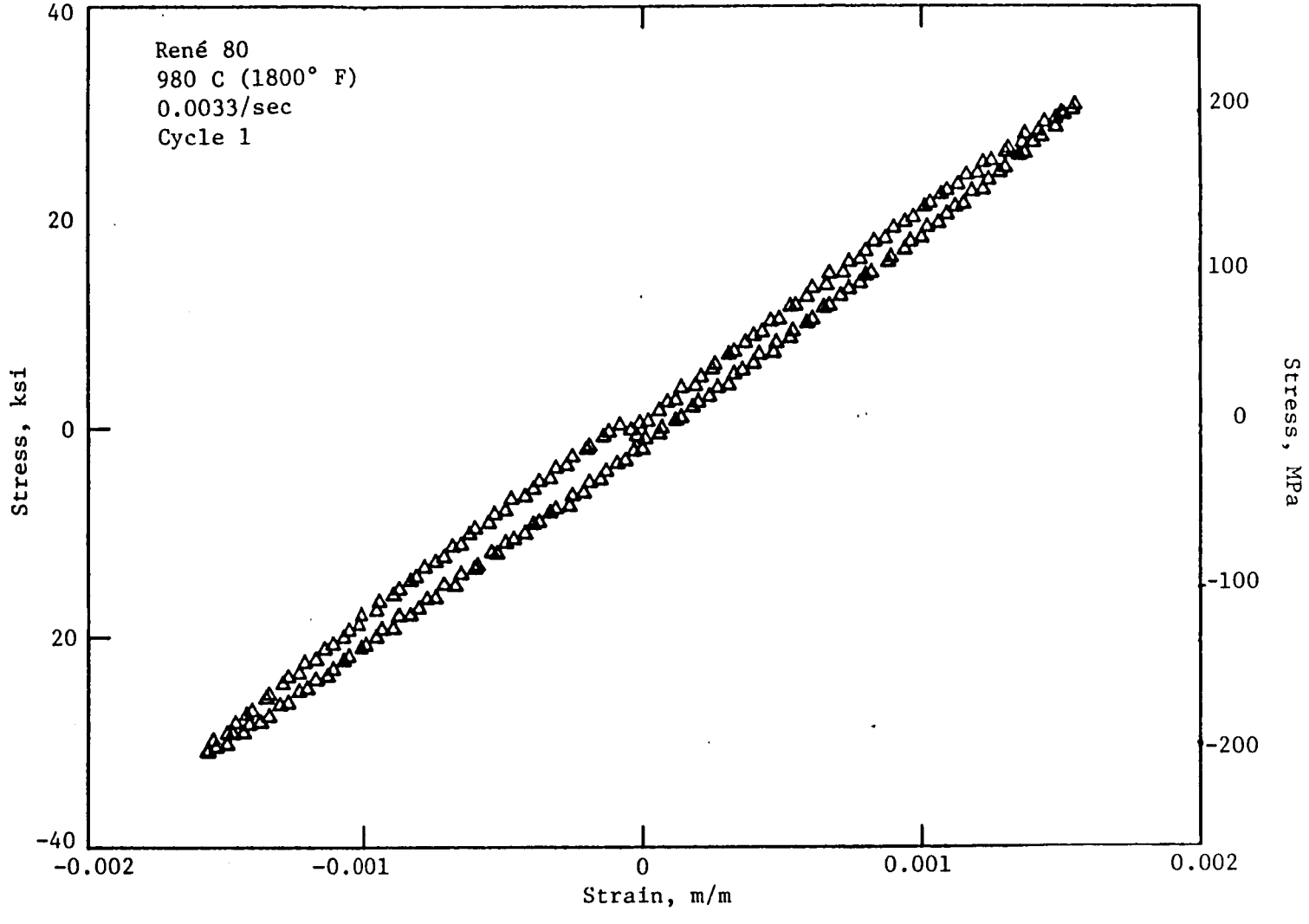

Figure 31. Data From First Cycle of a René 80, 980° C, Cyclic Test.

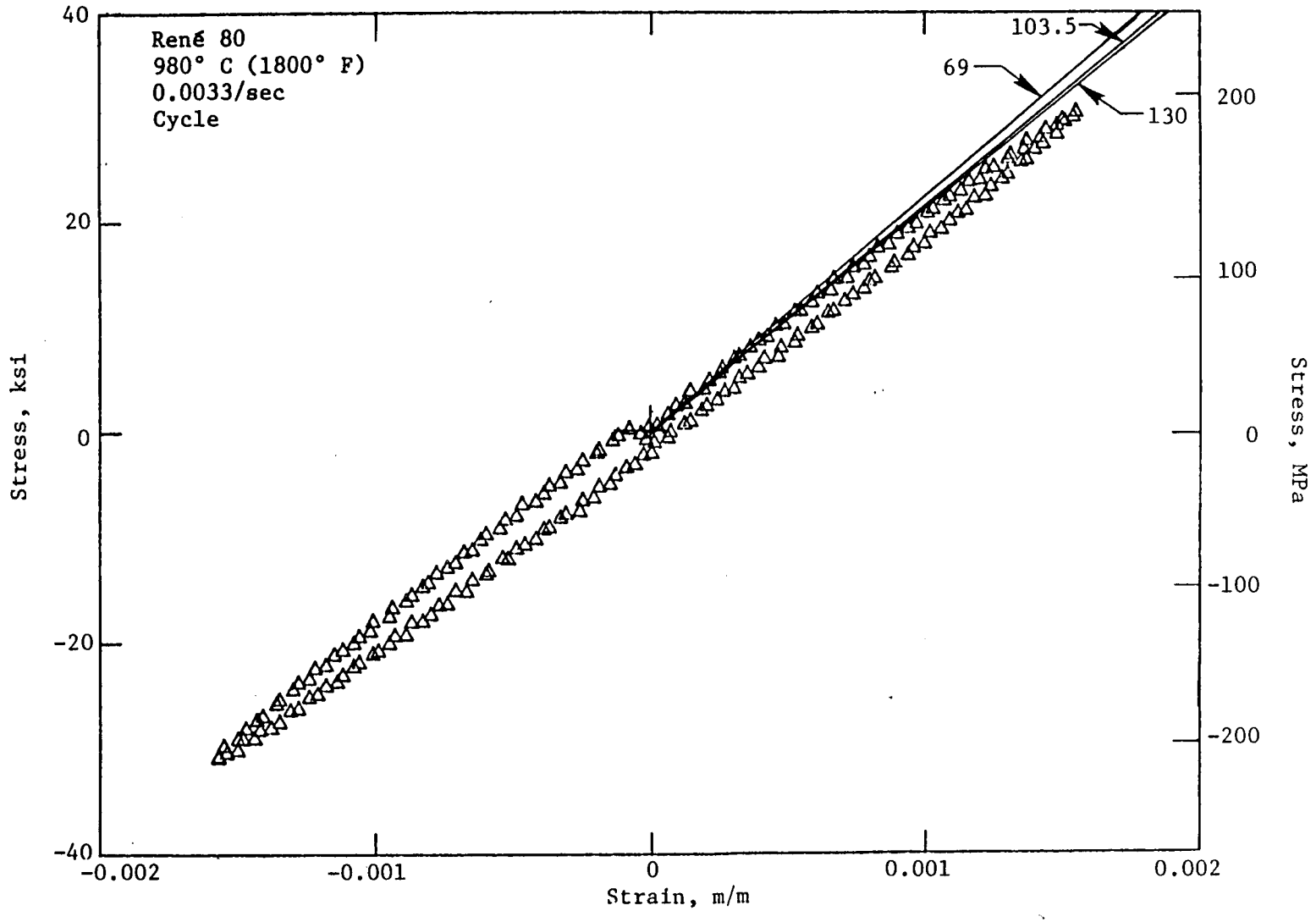

Figure 32. Comparison of Methods for Calculation the Elastic Modulus.

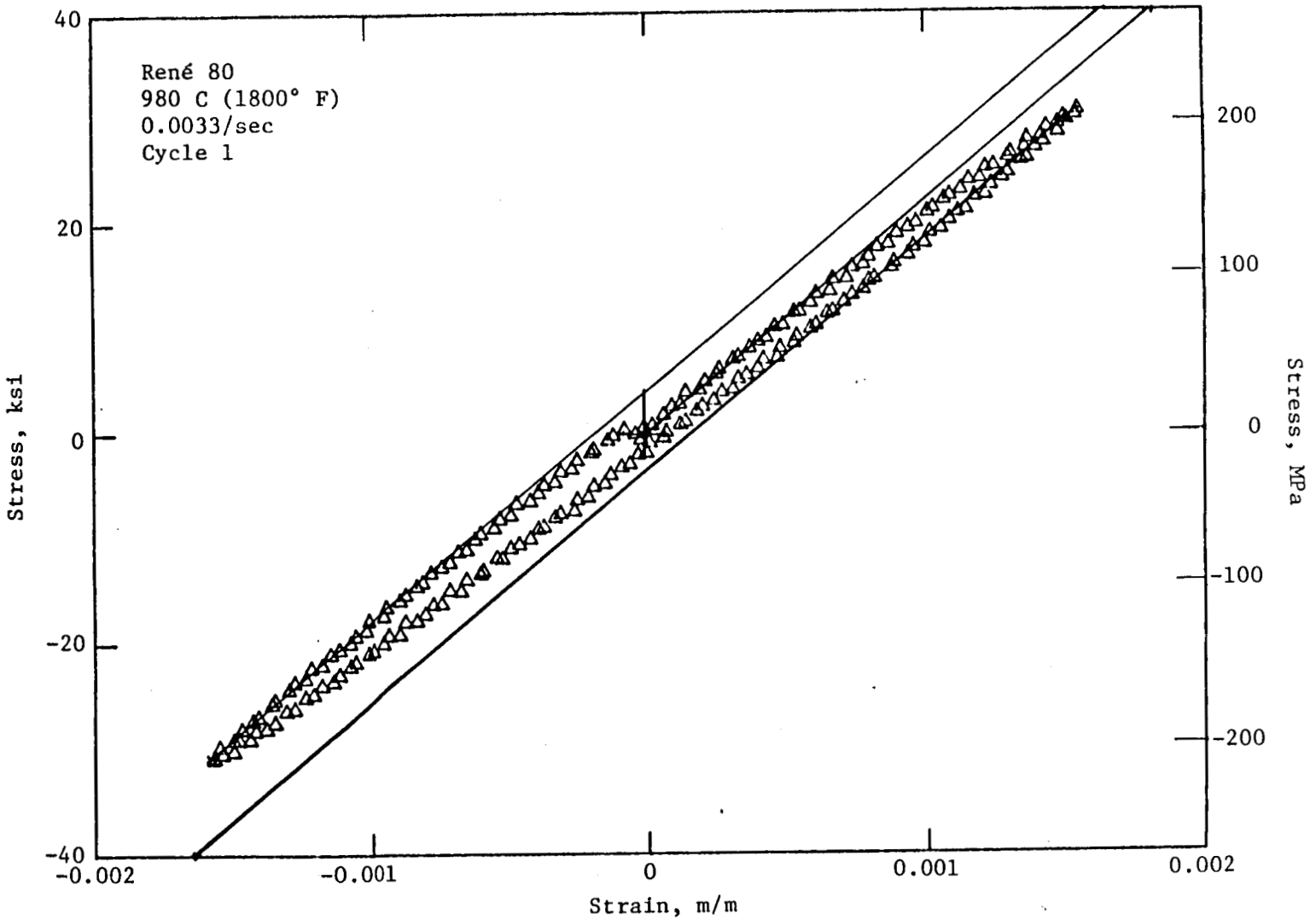

Figure 33. Comparison of Data with Modulus Lines Determined by a Limiting Stress of 69 MPa.

An averaging procedure was developed to calculate the first derivatives of σ, ε, and ε_E^I with respect to time. Figure 34 presents the same data previously seen in Figure 31 except that the data are connected point-to-point by a straight line rather than shown as individual data points. The jagged appearance of the line in Figure 34 is largely a result of the 5 mV resolution in the data acquisition system. This jagged appearance requires that the derivative properties be determined using a smoothing technique.

The approach taken in this program was to fit the data with a seven point sliding polynomial. This technique performs a least square regression analysis through the first seven data points. Then the first datum is dropped, the eighth datum is added, and a new polynomial regression is performed. This procedure is repeated until the last seven data points are analyzed. The polynomial used in this investigation was

$$y = a_0 + a_1 t + a_2 t^2 + a_3 t^3 \qquad (4)$$

where

$$y = \sigma, \varepsilon, \text{ or } \varepsilon^I$$

and t = time

The derivative of y with respect to time is

$$\dot{y} = a_1 + 2a_2 t + 3a_3 t^2 \qquad (5)$$

The values of the coefficients a_0, a_1, a_2, and a_3 were determined by least square regression analysis to Equation 4, and the derivative property was calculated using Equation 5 at the fourth point of the seven used in the polynomial regression. With this approach, the value of $\dot{y}$ can be determined for each point except the first or last three data points.

Figures 35 (a) and (b) show the variation of stress and strain respectively, with time for the fatigue cycle shown in Figure 31. The stress-strain response during this cycle is rather well behaved and shows no abrupt transients.

These data were analyzed with both a second order ($a_3 = 0$) and third order polynomial. Figure 36 (a) and (b) show the values of $\dot{\sigma}$ and $\dot{\varepsilon}$ as a function of time, calculated using both a second-order and third-order polynomial regression analysis. The values of $\dot{\sigma}$ and $\dot{\varepsilon}$ for third-order polynomial regressions (x-symbols) show much higher scatter than those for the second-order polynomial regression (triangles). The most disturbing observation is seen in Figure 36, where a negative value of $\dot{\sigma}$ was determined during the loading portion of the curve. A look at the stress-time data shown in Figure 35a strongly suggests that this is physically unreasonable. On this basis, the values of $\dot{\sigma}$, $\dot{\varepsilon}$, and $\dot{\varepsilon}^I$ were determined using a second-order, seven point sliding polynomial. This restriction permits the value of y to pass through a maximum or minimum, but prohibits the existence of an inflection point ($\ddot{y} = 0$ at a specific value of y) in a y versus time plot. Based on the rather uniform variation of constitutive response in René 80, this seems to be a reasonable restriction for this program.

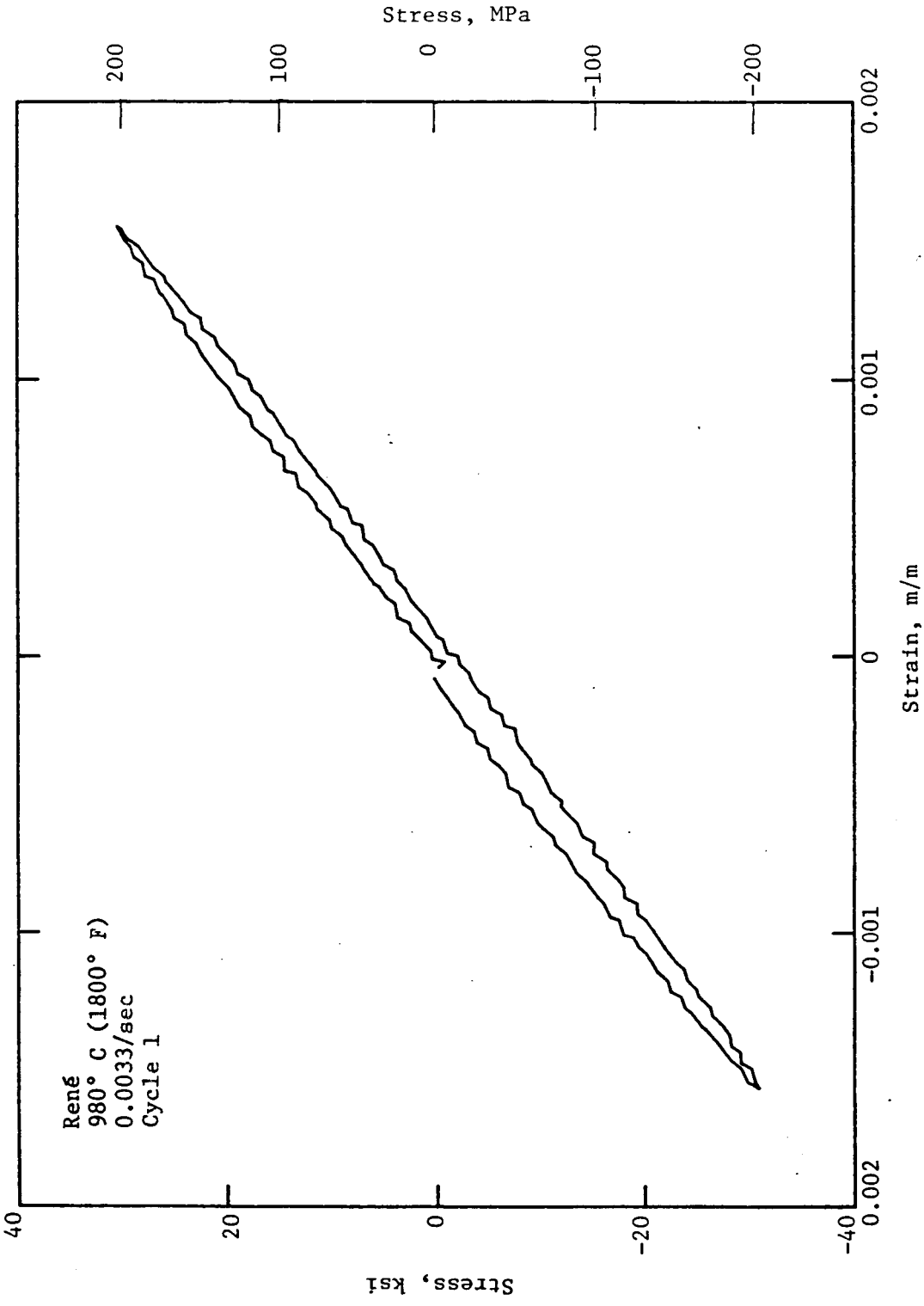

Figure 34. Straight Line Connection of Data in Figure 33.

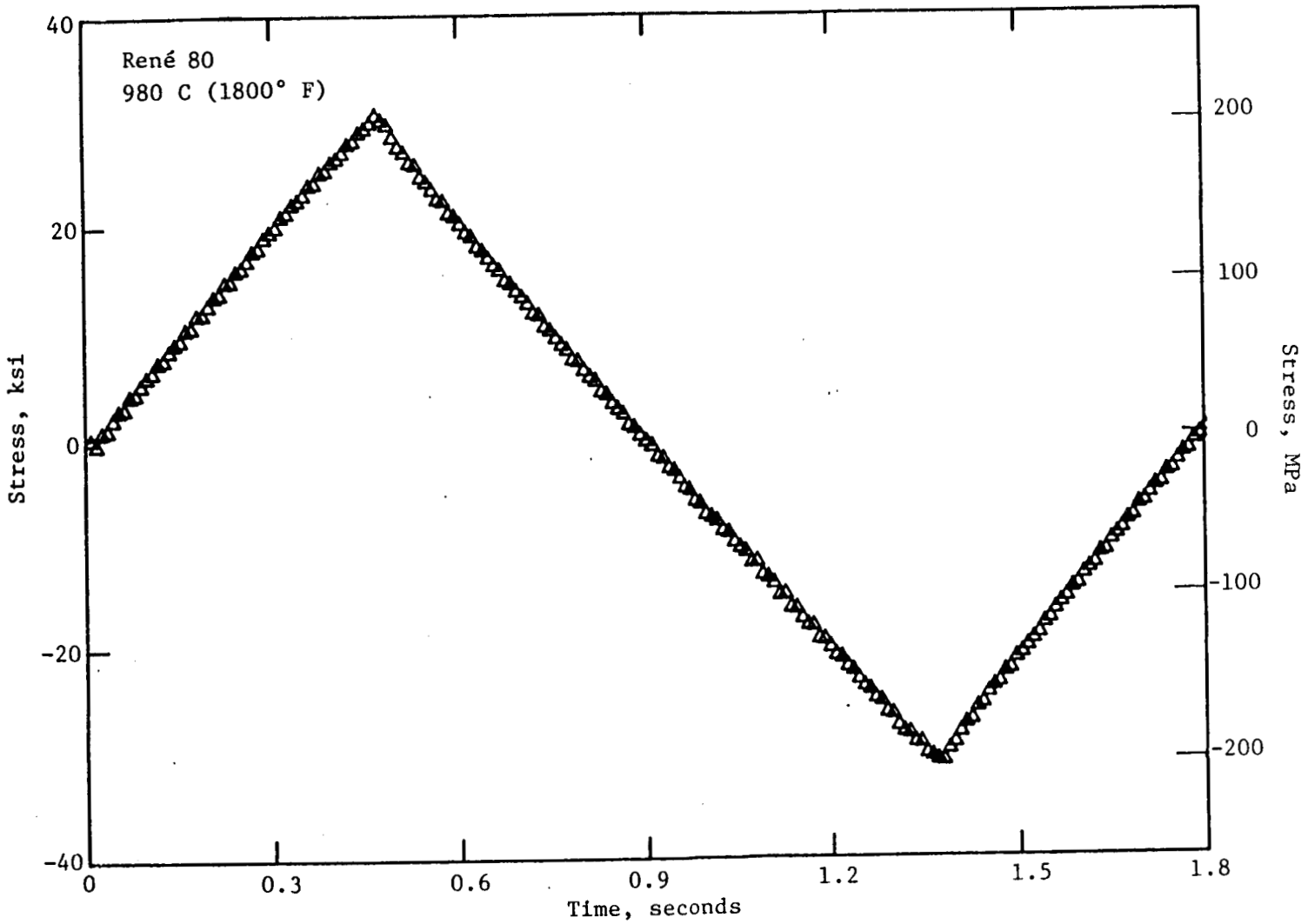

(a) Stress Versus Time.

Figure 35. Raw Data for Fatigue Cycle in Figure 31.

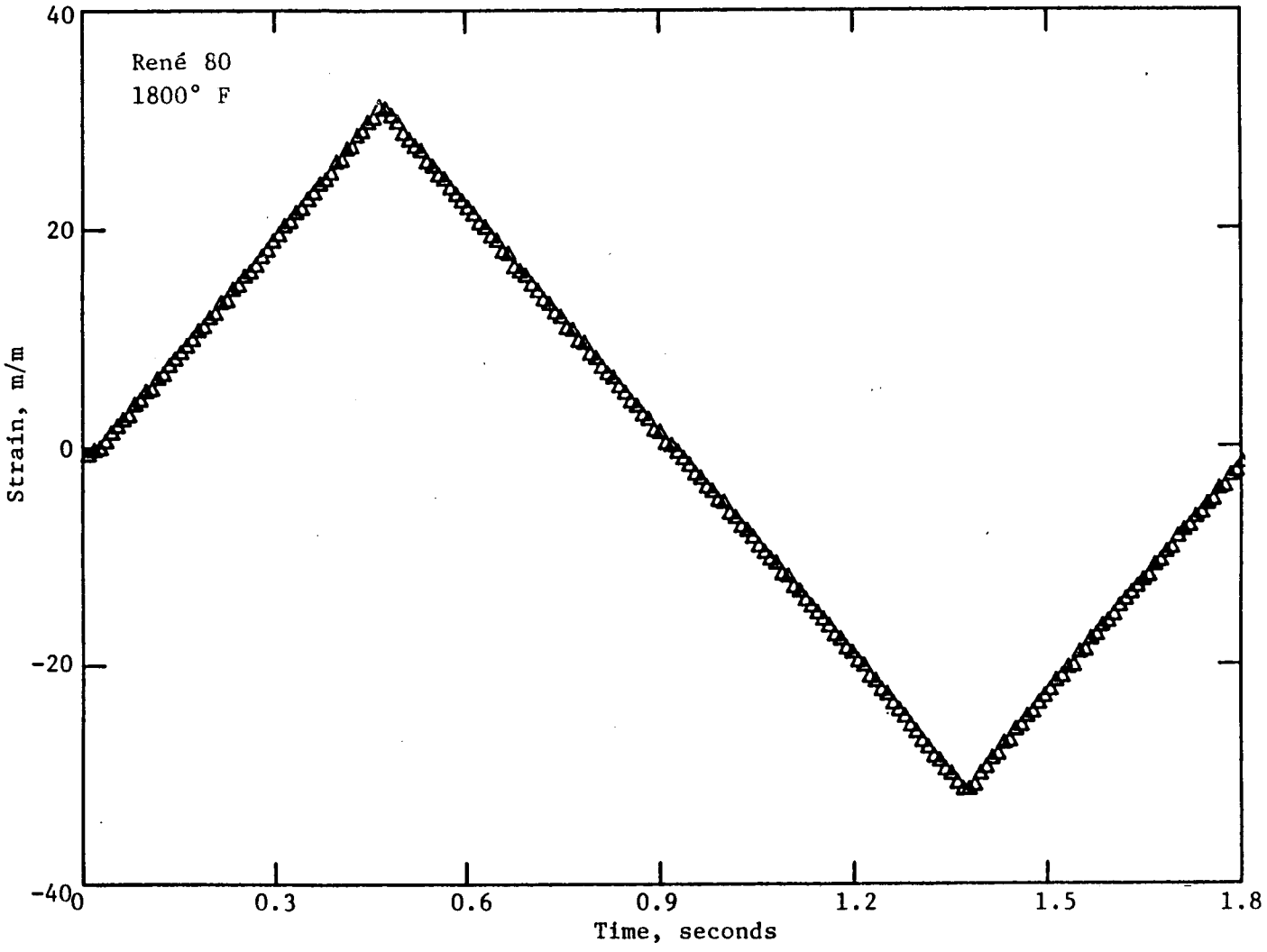

(b) Strain Versus Time.

Figure 35. Raw Data for Fatigue Cycle in Figure 31.

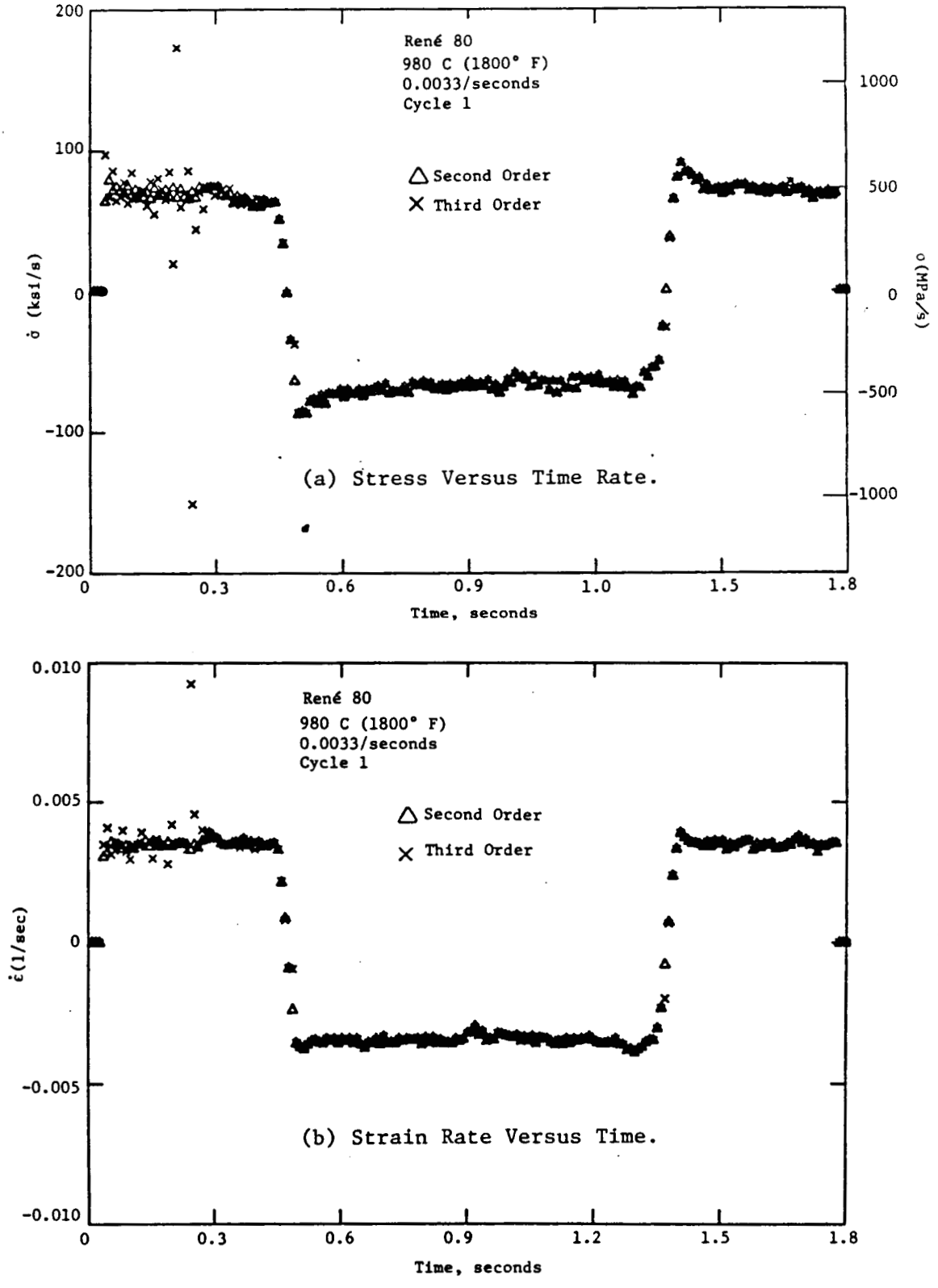

Figure 36. Calculated Rates for Fatigue Cycle in Figure 31.

4.2 EXPERIMENTAL DATA

Only the 1800° F tensile, creep, and $A_\varepsilon = \infty$, continuously cycled René 80 tests have been analyzed at this time. The results of the tensile and creep tests will be discussed in detail in this section to show that the data analysis method properly analyzes the data. The results of all three types of tests will be used in subsequent sections of this report to develop the constitutive model.

Figure 37 shows the stress-strain data at 980° C (1800° F) from René 80 tensile tests at four different strain rates. As expected, the strain rate did not alter the elastic response but significantly affected the stresses during plastic straining. Figure 38 shows the stress as a function of inelastic strain. A two-orders-of-magnitude increase in strain rate increases stress by approximately 50%. A few negative values of ε^I are shown in Figure 38. These are primarily a result of the errors associated with 5mV resolution of stress and strain. The collapse of the elastic portion of the stress-inelastic strain curve supports the accuracy of the data analysis procedures. Figure 39 shows the inelastic strain rates plotted as a function of total strain for the 980° C (1800° F) tensile tests. For plots such as these, the nominally elastic portion of the data has been deleted. The straight lines in this figure are constructed at the applied total strain rates. This figure shows that after approximately 1% strain, $\dot{\varepsilon}^I$ rapidly approaches the total strain rate $\dot{\varepsilon}$. These data show no difficulty with the second order, seven point sliding polynomial technique.

Figure 40 shows the results of three 980° C, constant load (or engineering stress) creep tests. Figure 40 shows the total strain as a function of the logarithm of time. The behavior that occurs at approximately 10 seconds is the transition from elastic loading to a constant stress condition. Figure 41 shows the variation of inelastic strain rate $\dot{\varepsilon}^I$, with total strain for the two higher stress tests. These results showed that both of these tests pass through a minimum creep rate.

The remainder of the tests will be analyzed in the near future.

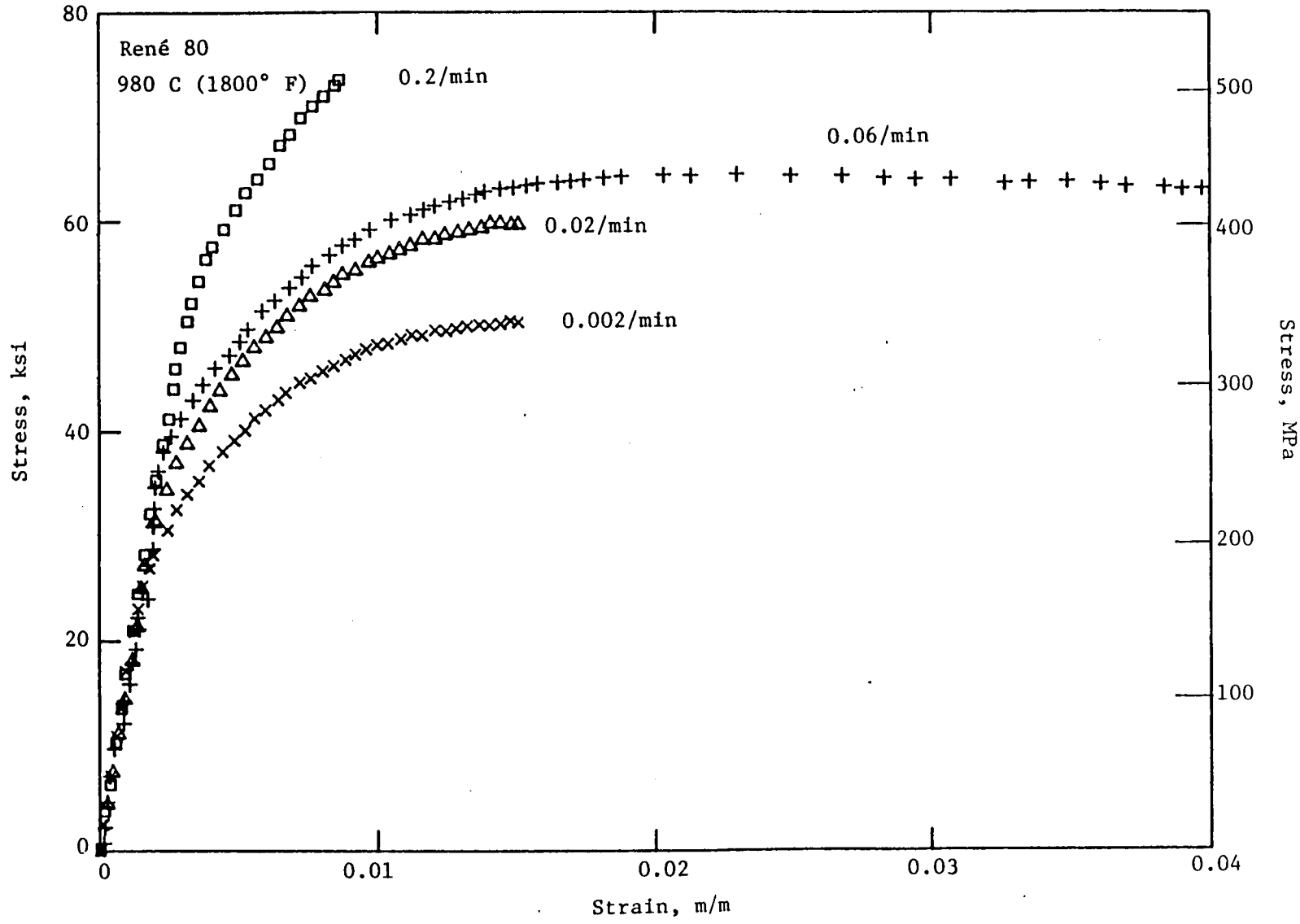

Figure 37. Tensile Test Data at 980° C.

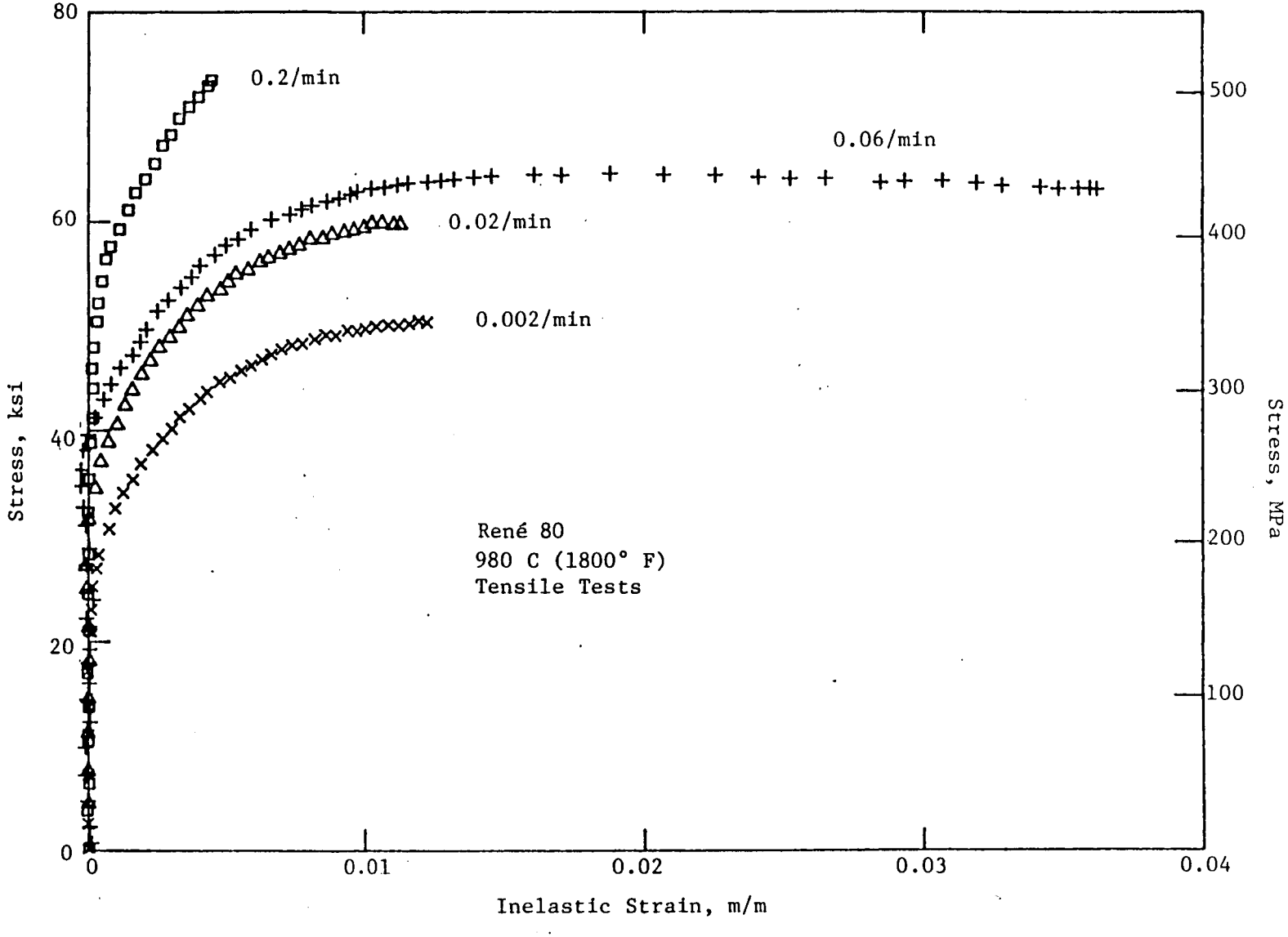

Figure 38. Stress Versus Inelastic Strain, Tensile Tests, 980° C.

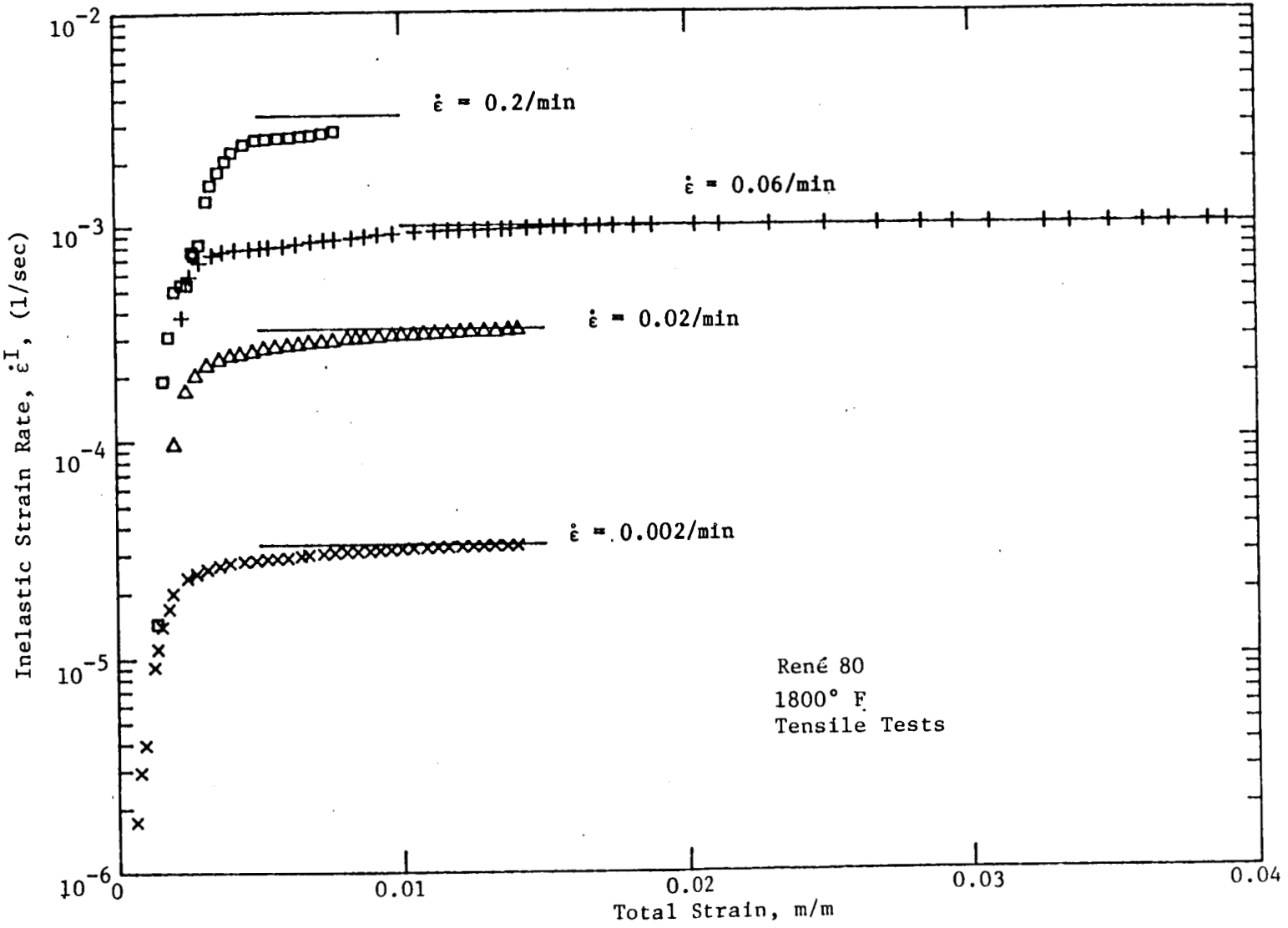

Figure 39. Saturation of Inelastic Strain Rate, 980° C Tensile Tests.

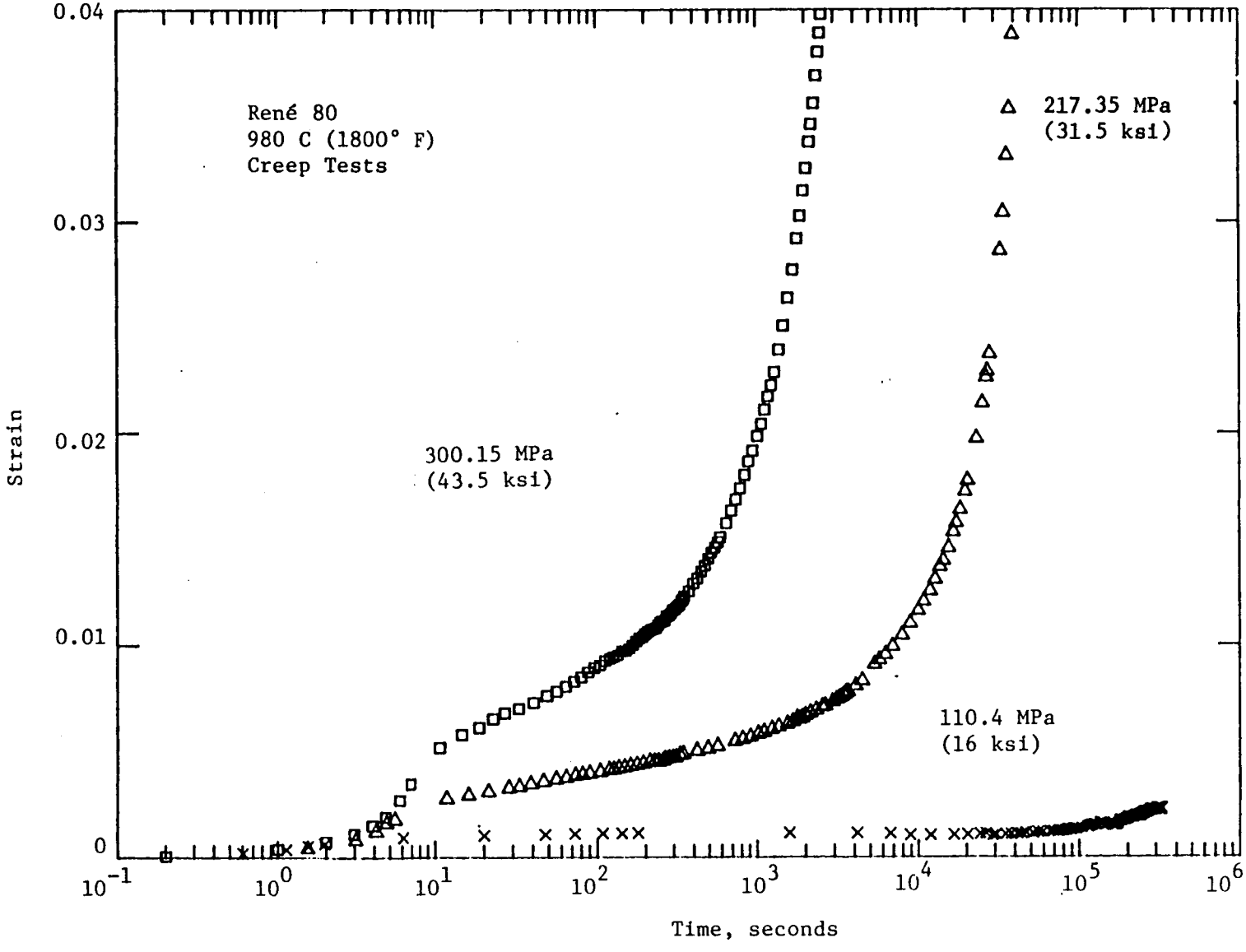

Figure 40. Creep Test Results, 980° C.

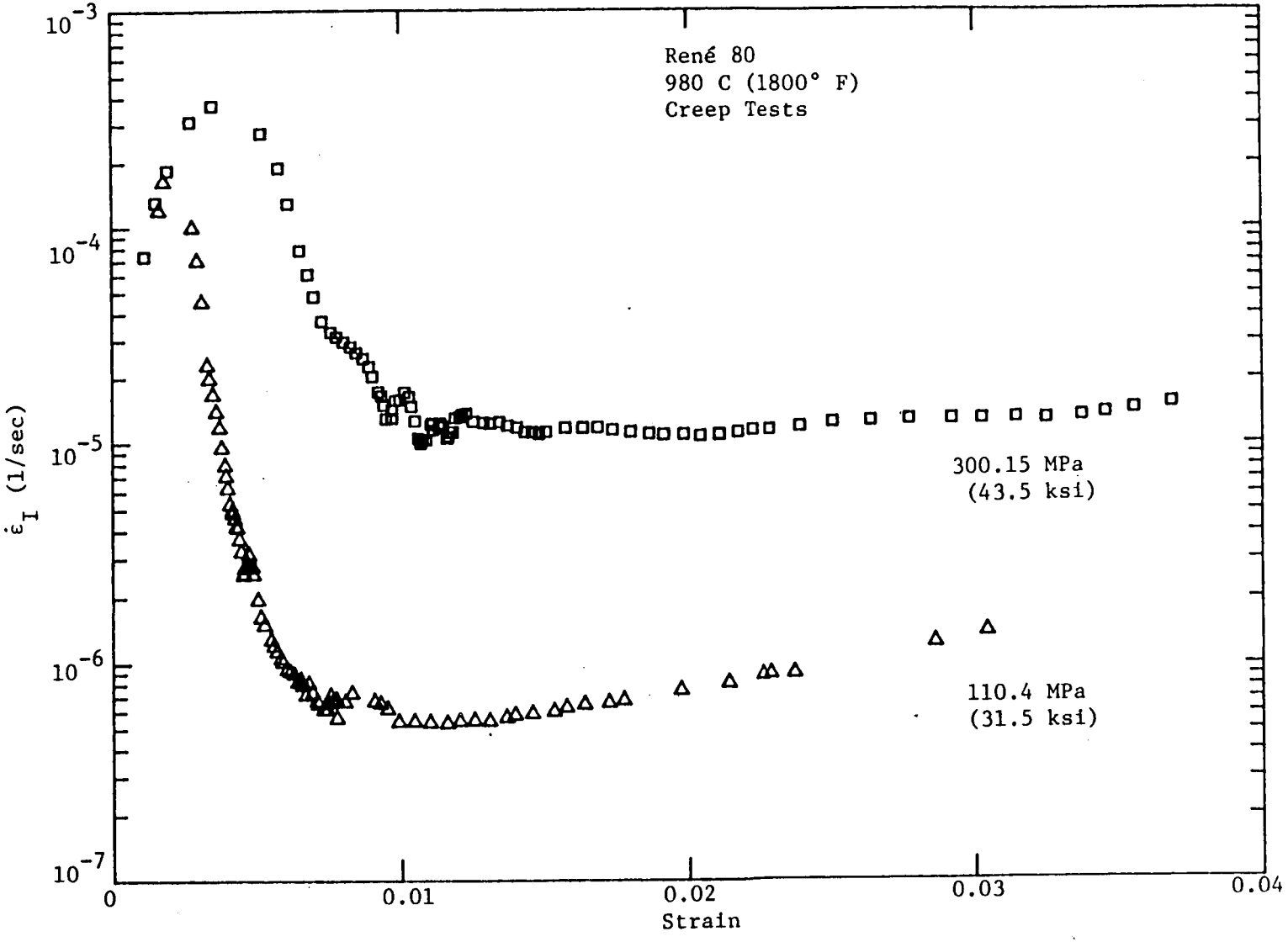

Figure 41. Hodograph of Results of Two Creep Tests 980° C.

5.0 UNIAXIAL EVALUATION OF CONSTITUTIVE MODELS

The comprehensive uniaxial test programs described in the previous sections provide a sound basis for evaluating the two selected unified constitutive models. Once the appropriate material parameters in the models are known for René 80 (base material) analytical predictions can be compared with the experimental results to evaluate the strain rate sensitivity, creep, stress relaxation, history dependence, cyclic softening, and anelasticity capabilities of the two models. The computer programs mentioned in Section 2.0 can be used for this purpose.

However, it has been widely recognized that one of the major sources of difficulty in the use of unified constitutive theories is the determination of the material parameters. No general procedures for determining these parameters are currently available; and therefore, considerable effort has been made in the present contract to develop such a method.

The approach adopted is to develop a computer program which directly uses the various test results as input and generates the various material parameters as output. The program is kept as flexible as possible so that different functional forms can be used. This approach also assures consistency in the treatment of the various test data. However, it should also be noted that, while conceptually simple, such an approach can be very challenging because of the nonlinear equations involved. Such a computer program has been developed for a generic back stress/drag stress model.

The generic back stress/drag stress model is described by the following set of equations for the uniaxial case:

$$\dot{\varepsilon}^I = \left(\frac{\sigma - \Omega}{Z}\right)^N \operatorname{sgn}(\sigma - \Omega) \tag{6}$$

$$\dot{\Omega} = f_1 \dot{\varepsilon}^I - f_2 \left|\dot{\varepsilon}^I\right| \Omega - R_1 \tag{7}$$

$$\dot{Z} = g_1 \left|\dot{\varepsilon}^I\right| - g_2 \left|\dot{\varepsilon}^I\right| Z - R_2 \tag{8}$$

where

$\dot{\varepsilon}^I$ = Inelastic Strain Rate
Ω = Back Stress
Z = Drag Stress

R_1 and R_2 are static thermal recovery functions,
f_1 and g_1 are the hardening functions, and
f_2 and g_2 are the dynamic recovery functions.

Equations 6, 7, and 8 are a set of coupled nonlinear differential equations. The specific forms for the various hardening and recovery functions are significantly different for the various models that have been published. The approach taken in this project is to choose those forms that appear most appropriate for the behavior of René 80. To determine the various material parameters involved, an iterative approach is used. Some starting assumptions are made, which are later relaxed. Specifically, it is assumed that (1) the saturation values for the back stress and drag stress at the end

of the monotonic tests are independent of the strain rate, (2) the drag stress is a monotonically decreasing function, and (3) during steady state creep, the state variables are constant. Their successive nonlinear optimizations are performed in Equations (6), (7), and (8) based on the experimentally measured quantities.

Figure 42 shows a flow chart of the evaluation process for the back stress/drag stress model. As described in Section 4.0, the various test data are first reduced such that stress (σ), strain (ε), time (t), inelastic strain (ε^I), stress rate ($\dot{\sigma}$), strain rate ($\dot{\varepsilon}$), and inelastic strain rate ($\dot{\varepsilon}^I$) are known throughout the test. These results are stored in a computer file that forms the input to the computer program to determine the material parameters.

In the following, the recovery function R_2 is neglected in Equation (8) to yield a greatly simplified form for the drag stress equation:

$$Z = Z_1 + Z_2 \, e^{-Z_3 \Sigma |\varepsilon^I|} \tag{9}$$

where $\Sigma |\varepsilon^I|$ is the accumulated inelastic strain. When the parameters Z_1, Z_2, and Z_3 are positive, the drag stress is a monotonically decreasing function of the accumulated inelastic strain. Previous exercises, described in Section 2.0, had shown that this form of the drag stress equation can model cyclic softening behavior. Rene 80, the base material in this project, cyclically softens at elevated temperatures.

A basic feature of both unified models selected here is that their flow equation can be inverted easily. Thus, the back stress Ω is found during the test using

$$\Omega = \sigma - Z(|\dot{\varepsilon}^I|^{1/N}) \operatorname{sgn}(\dot{\varepsilon}^I) \tag{10}$$

Here, Z can be taken as a constant (= 20), to start. From this, it is possible to find Ω during the test using an appropriate numerical technique. After several trials, it was found that a seven-point sliding technique using a Ramberg-Osgood relation worked satisfactorily for the back stress rate. Based on this Ω and Equation (7), a nonlinear optimization is performed to determine the material parameters in f_1, f_2 and R_1. This is done such that f_1, f_2 are found from high strain rate tests and R_1 from slow strain rate tests and creep tests.

The next step involves the determination of the drag stress equation parameters. The equation for $\dot{\Omega}$ (7) is considered known. The back stress Ω is found by numerical integration:

$$\Omega = \int_0^t \dot{\Omega} \, dt \tag{11}$$

The drag stress Z is found by inverting Equation 6:

$$Z = \frac{|\sigma - \Omega|}{|\dot{\varepsilon}^I|^{1/N}} \tag{12}$$

Nonlinear optimization is performed using Equations (9) and (12) to find Z_1, Z_2, and Z_3. This completes the first iteration of the procedure.

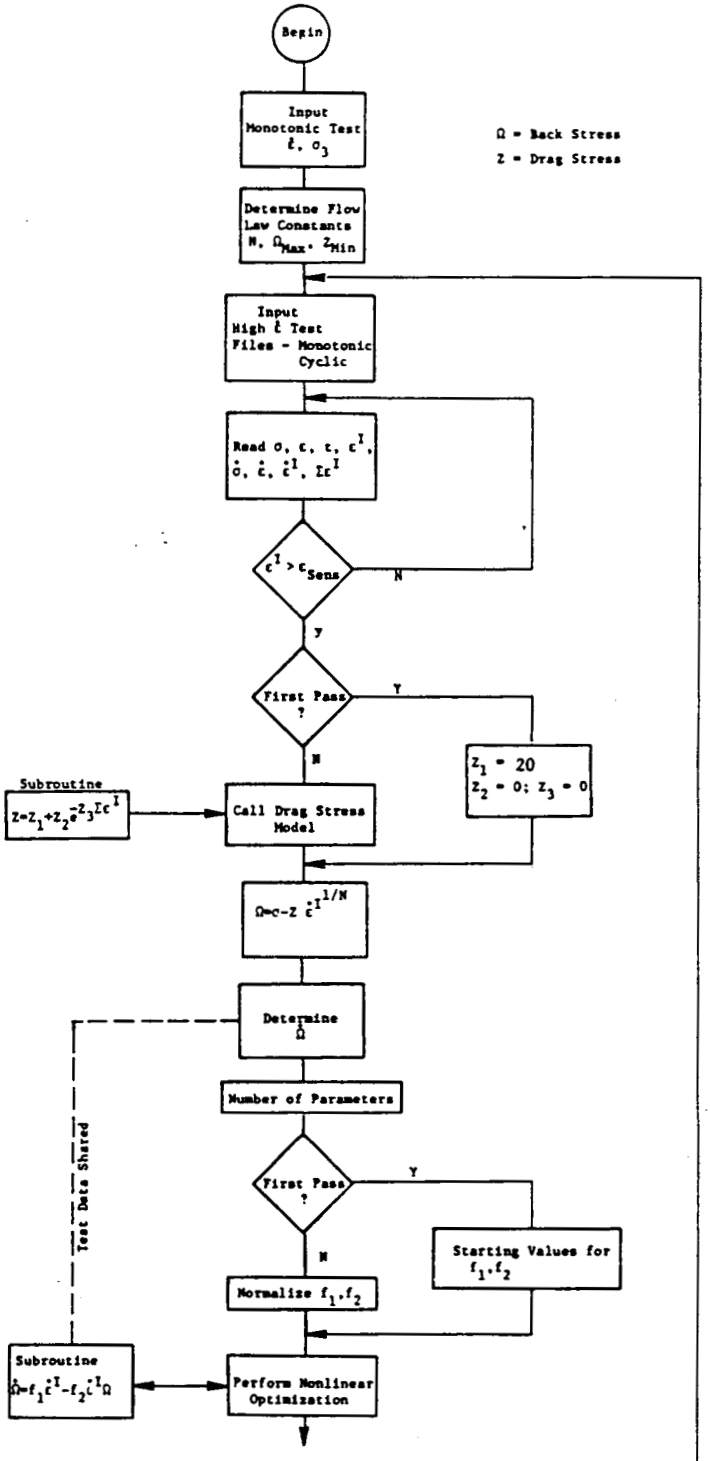

Figure 42. Schematic of the Material Parameters Determination Procedure.

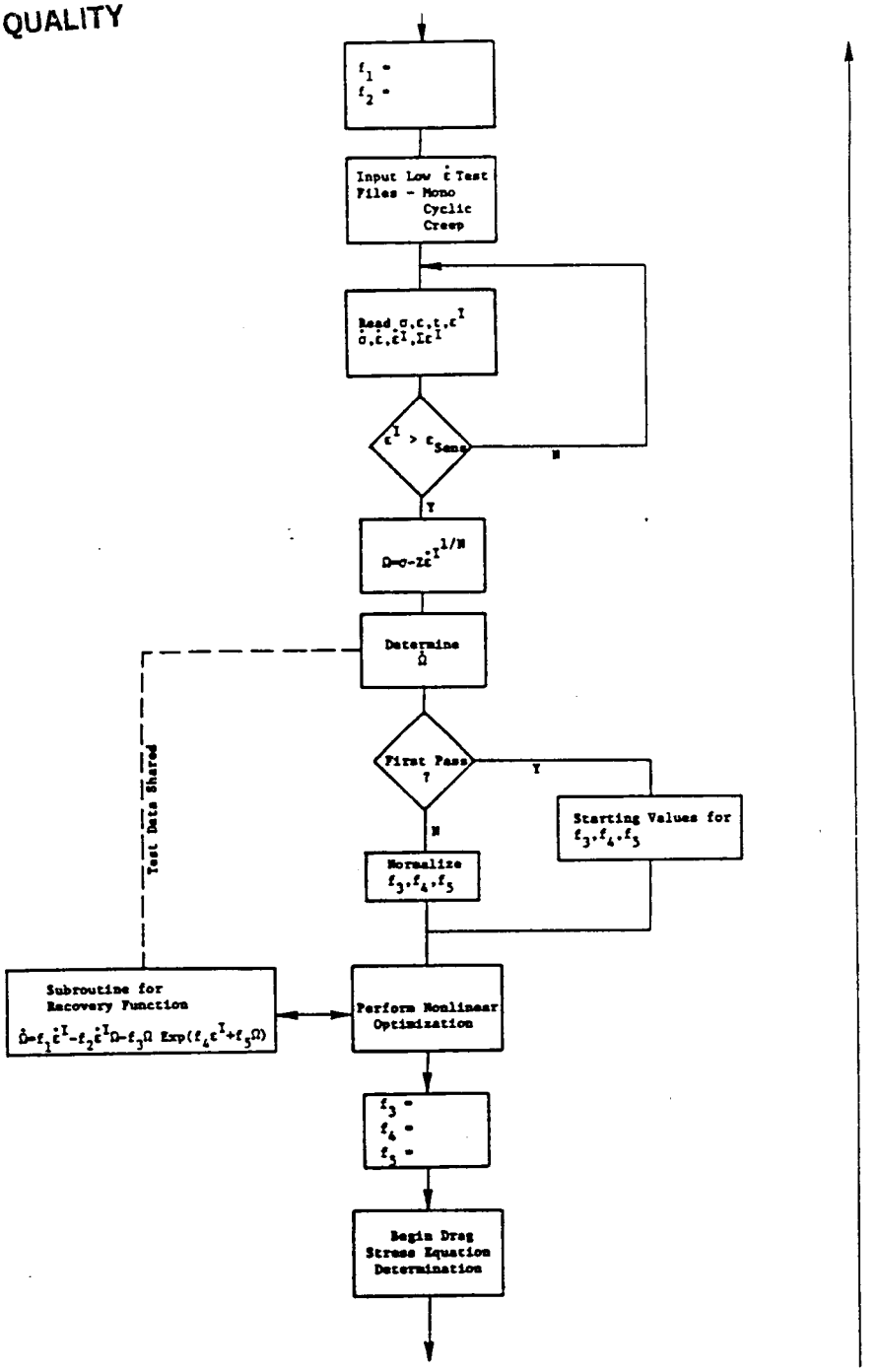

Figure 42. Schematic of the Material Parameters Determination Procedure (Continued).

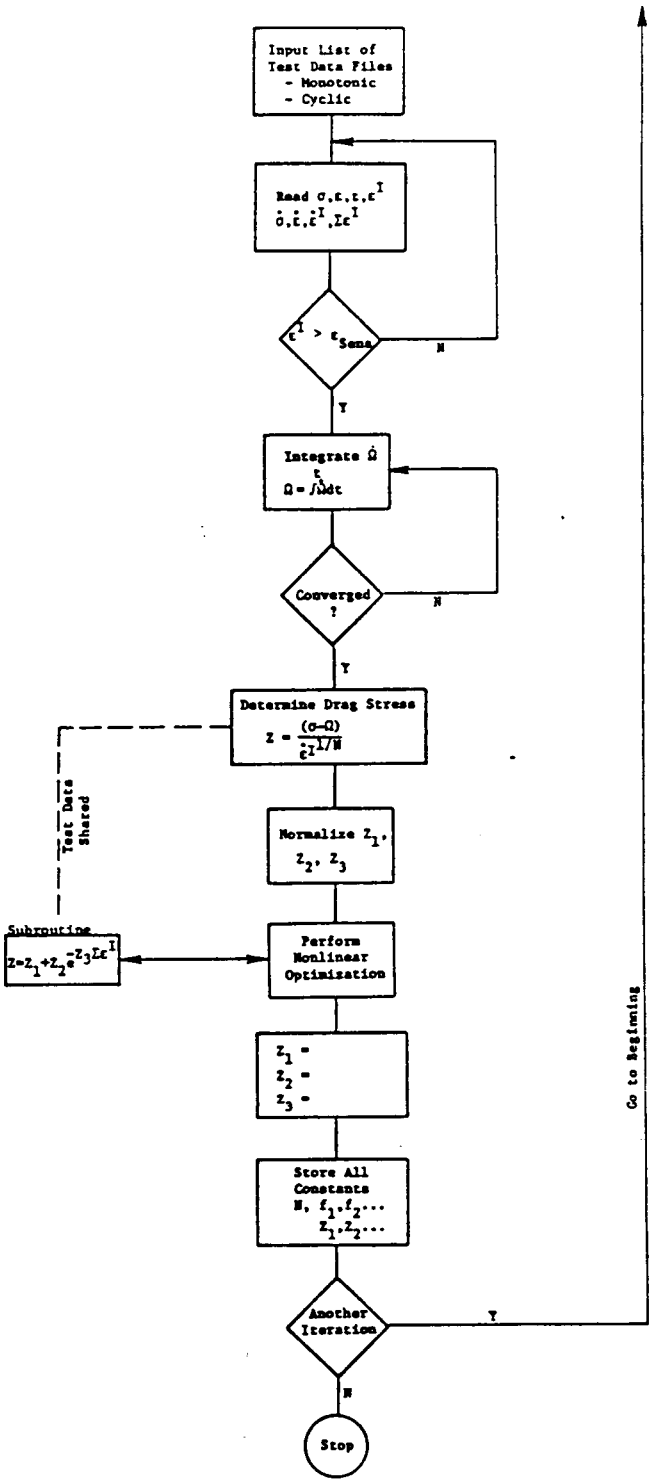

Figure 42. Schematic of the Material Parameters Determination Procedure (Concluded).

With Z_1, Z_2, and Z_3 known, the drag stress Z is known during a test. Using this value, a new back stress is calculated from Equation (10) and the whole process is repeated.

René 80 test data at 980° C (1800° F) have been analyzed in detail using a computer program incorporating the procedure described above. Some of the notable results are discussed below.

1. f_1 = constant, f_2 = constant appears to work reasonably well for this case.

2. An appropriate form for the static recovery term in Equation (7) appears to be:

$$R_1 = f_3 \, |\Omega| \, \exp \, (f_4 \, |\dot{\varepsilon}^I| + f_5 \, \Omega)$$

where f_3, f_4, f_5 are constants. The constants in R_1 have been found using slow strain rate monotonic and creep tests. However, the overall contribution of the above term seems extremely small, as compared to the hardening and dynamic recovery terms.

3. Figure 43(a) shows the results of the iteration procedure after five iterations, using only the high $\dot{\varepsilon}$ monotonic test (0.2 in/in/min). It appears that parameters determined using the computer program can reproduce the stress strain behavior reasonably well. Figure 43(b) shows the same result using only the lower strain rate monotonic test (0.002 in/in/min). The constants for these two strain rates are significantly different. The main deviation seems to arise from the drag stress equation parameters. A similar conclusion, based on cyclic tests, is drawn later.

The monotonic-based constants are not able to predict the cyclic behavior. Figure 44 shows the cyclic loop predictions using monotonic-based constants. The test data, Figure 44(a), indicate that the 96th cyclic loop is stable, without any further softening. The model, however, predicts too much softening after only 3 cycles. The model prediction for the slow strain rate test (Figure 44b) shows stable behavior, but the inelastic strain range is predicted poorly. The deficiencies in the cyclic softening prediction are believed to arise from the drag stress equation. Past experience has shown that the drag stress equation constants control cyclic softening.

Figure 45 shows the results using constants based on all monotonic tests. Note that these parameters overpredict the high $\dot{\varepsilon}$ tests and underpredict the low $\dot{\varepsilon}$ tests. Therefore, although the model appears satisfactory for a specific strain rate, it does not seem able to represent the entire strain-rate spectrum used here (0.002 in/in/min to 0.2 in/in/min).

Figure 46(a) compares the test data and model prediction for a cyclic test at 0.2 in/in/min. (The result shown is for the 96th cycle.) It is assumed that the accumulated inelastic strain is large enough that the drag-stress has saturated to a constant value. The material parameters used (based on this particular test only) were obtained in 15 iterations. The initial hardening shown in the plot is disregarded because the prediction was made for only 2

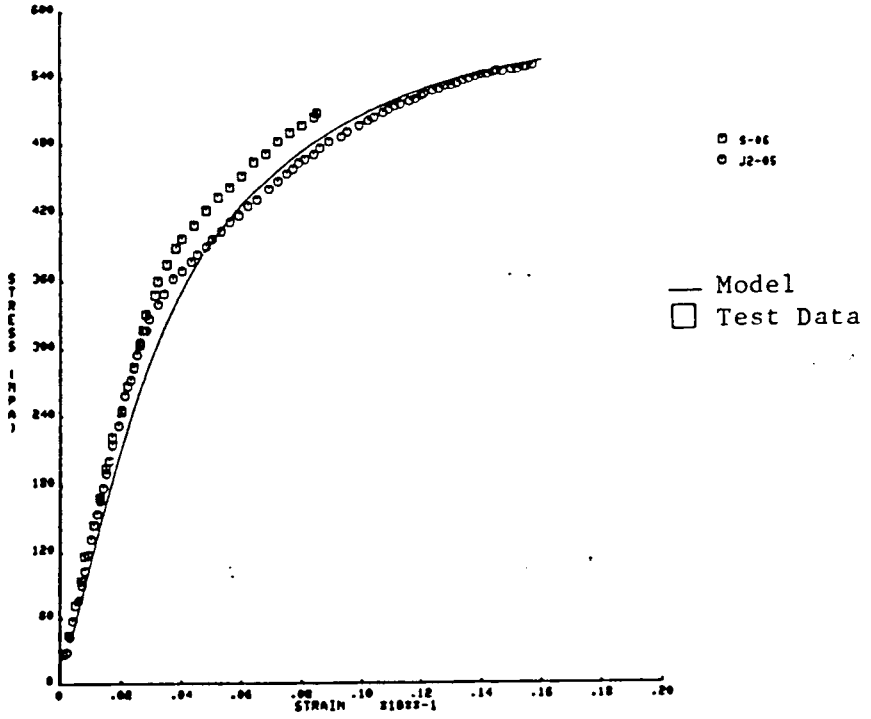

(a) 0.2 in/in/min

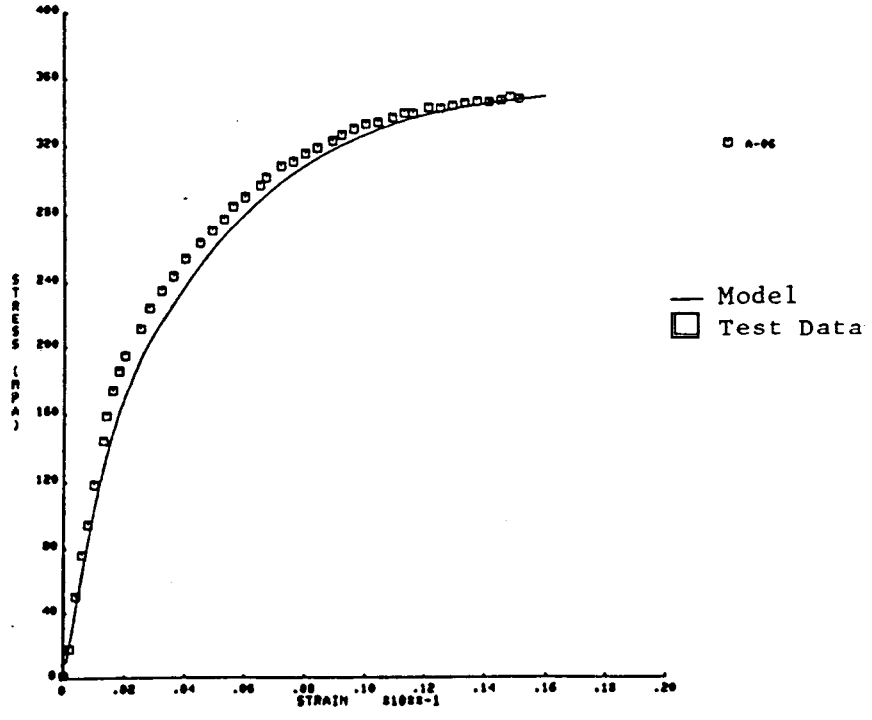

(b) 0.002 in/in/min

Figure 43. René 80 980° C (1800° F) Monotonic Test.

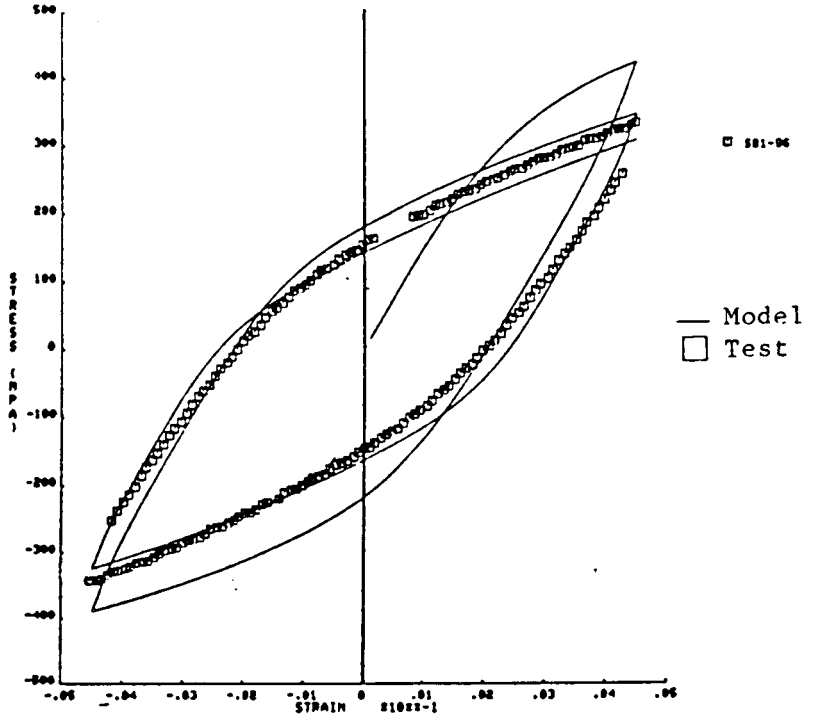

(a) 0.2 in/in/min.

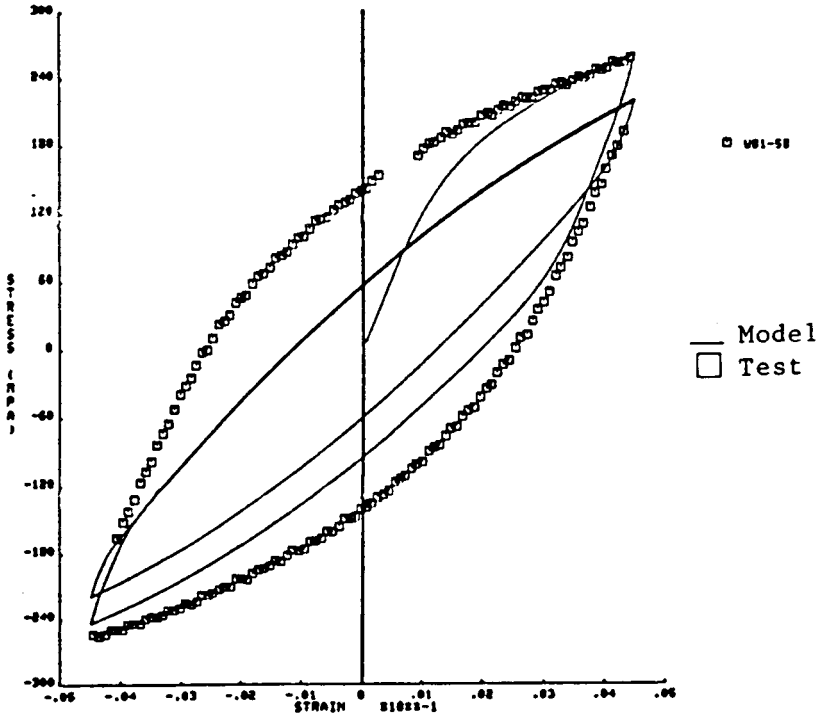

Figure 44. René 80 980° C (1800° F) Test: Model Prediction Using Monotonic Based Material Parameters.

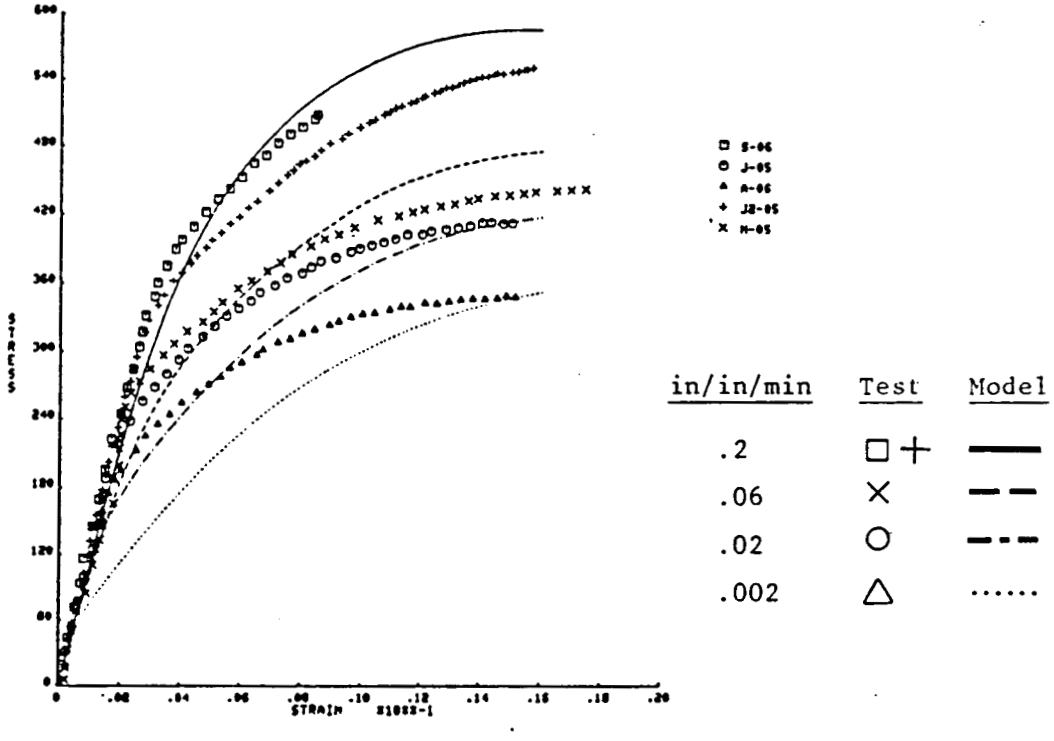

Figure 45. René 80 980° C (1800° F) Monotonic Tests.

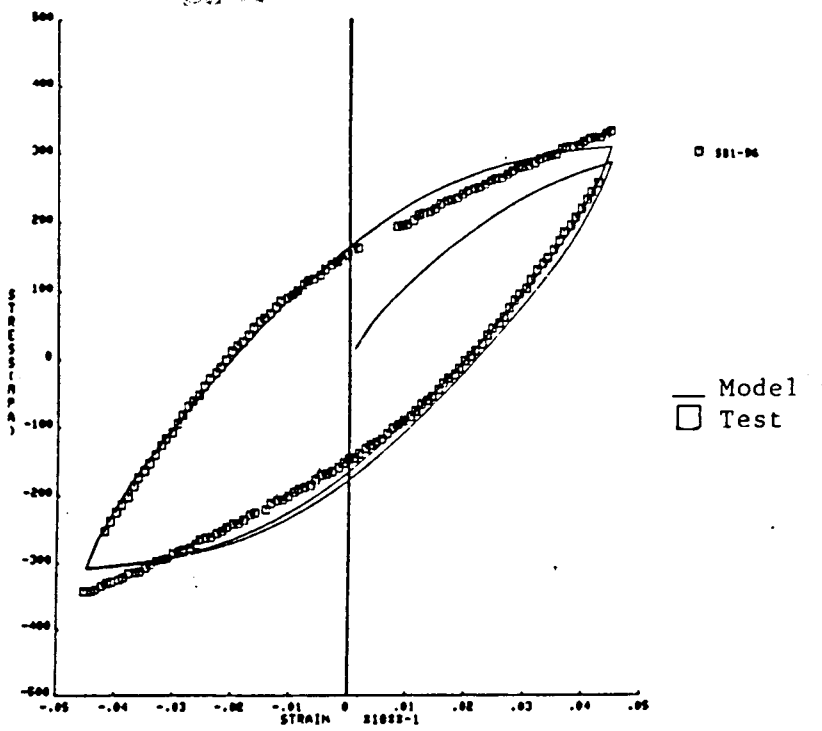

(a) 0.2 in/in/min, 96th Cycle.

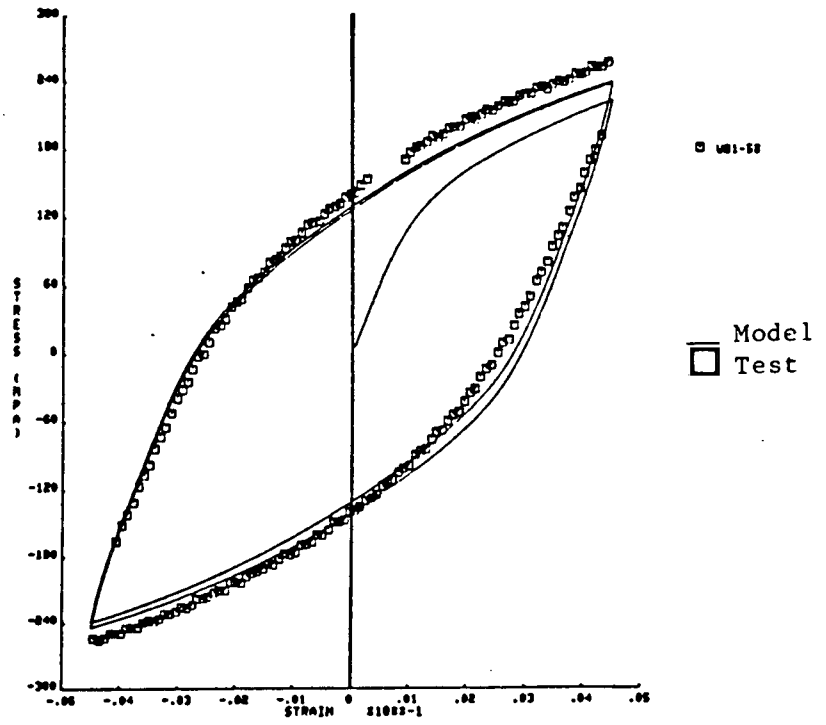

(b) 0.002 in/in/min, 58th Cycle.

Figure 46. René 80 980° C (1800° F) Cyclic Test.

cycles and not the entire 96 cycles. It is clear that this set of material parameters in the model predicts the entire hysteresis loop very well. The maximum and minimum values of stress and inelastic strain are predicted accurately. Figure 46(b) shows similar results for the 0.002 in/in/min cyclic test.

Figure 46 indicates that the test procedure works well for each strain rate. However, the material parameters are significantly different for the two cases. The difference is seen to be caused by the drag-stress equation parameters, as in the monotonic case. This again points to the limitation of the particular model in representing a wide range of strain rate behavior. It appears to be good only for a limited range of strain rates.

Current work is extending the analysis to lower temperatures. René 80 test data indicate less strain rate sensitivity at lower temperatures. A similar procedure is being developed for the Bodner model, which involves only one evolution equation.

6.0 FINITE ELEMENT CODE IMPLEMENTATION

In Task D of this program, a computer program will be developed for use with unified theories. As part of this effort, alternate solution strategies will be evaluated. In order to facilitate the evaluation of different solution methods and to make the final computer program as optimized as possible, a new, dedicated finite-element computer program is being developed.

The two-dimensional (2D) finite element code containing Bodner's constitutive model has been completed and tested. This code uses two-dimensional constant strain triangles and an incremental initial strain iteration technique. To facilitate the simulation of arbitrary load histories, the load history is partitioned into piecewise linear segments with steady state thermal conditions during each segment. In order to simplify input, reduce convergence problems, and minimize cost, a dynamic time-stepping procedure is incorporated. A 3D finite element code has also been developed. The 3D code employs 20-noded isoparametric bricks and computes inelastic strains at the order 2 Gauss points. Other features of the 3D code are essentially the same as for the 2D code.

The incremental equilibrium equation for the initial strain method with steady state thermal conditions is

$$[K]\ \{\Delta d^T\} = \{\Delta F\} + \{\Delta F^I\} \tag{13}$$

where [K] is the elastic stiffness matrix, $\{\Delta d^T\}$ is the increment in the total displacement vector, $\{\Delta F\}$ is the increment in the applied force vector, and $\{\Delta F^I\}$ is a pseudo force vector due to the increment in a vector of the inelastic strains components. The vector $\{\Delta F^I\}$ is calculated by

$$\{\Delta F^I\} = \sum_I^N \left(\int_v [B]^T [E]\ \{\Delta \varepsilon^I\}\ dv \right) \tag{14}$$

where N is the number of elements. In Equation (14), [B] is the strain displacement matrix and [E] is the elastic constitutive matrix.

At the beginning and end of a linear load case the elastic solutions are obtained using

$$\{d^E\}_0 = [K]^{-1} \{F\}_0$$

and

$$\{d^E\}_F = [K]^{-1} \{F\}_F \tag{15}$$

The vectors $d^E{}_{0,\ F}$ are the initial and final elastic displacements due to initial and final applied thermomechanical loads. The elastic displacements at any time t_i in the load case are given by

$$\{d^E\}_i = \{d^E\}_0 + \frac{t_i - t_0}{t_F - t_0} \left[\{d^E\}_F - \{d^E\}_0 \right] \tag{16}$$

The total displacement vector at time t_i is written as

$$\{d^T\}_i = \{d^E\}_i + \{d^I\}_{i-1} + \{\Delta d^I\} \tag{17}$$

where the increment in the inelastic displacement vector is

$$\{\Delta d^I\} = [K]^{-1} \{\Delta F^I\} \tag{18}$$

and the increment in the inelastic pseudo force vector is given by Equation (14). Thus, it is necessary to integrate the constitutive model from time t_{i-1} to t_i. Although any number of integration schemes could be used, a second order Adams-Moulton method was employed. Since the flow equation and the state variable evolution equation are coupled, an iterative procedure is needed to compute $\{\dot{\varepsilon}^I\}$ and $\dot{Z}$ at the end of a time step. The integration of the constitutive equation is within the overall equilibrium iteration loop as shown in Figure 47.

A significant improvement in the iteration scheme was achieved by making an initial estimate of the incremental inelastic pseudo force vector $\{\Delta F^I\}$ in the first iteration of a new time step. If $\{\Delta F^I\}$ is set equal to zero on the first iteration of a new time step (as is usually done) the first estimate of the solution may be very poor. An initial estimate of the inelastic strain increment for each element can be made using $\{\Delta\varepsilon^I\} = \{\dot{\varepsilon}^I\}_{i-1} \Delta t$, where $\{\dot{\varepsilon}^I\}_{i-1}$ is the inelastic strain rate at the beginning of the time increment. If this is then used in Equation (14) to make first estimate of the incremental inelastic force vector, the stability and rate of convergence of the method is improved. By including this logic, the number of equilibrium iterations was reduced by about 60%.

In a finite element code that allows a linear variation of applied loads, large excursions in stress and inelastic strain rate are to be expected. For economy and east of use, dynamic time incrementing is a necessity. There are two important considerations in developing such an algorithm: first, the stability of the iteration scheme and second, the accuracy of the integration procedure. The stability of the system of equations depends on the constitutive model, geometry, loading history, and material parameters. An approximate, but simple and effective approach is to base the time step on the maximum inelastic strain increment to occur in all of the elements. In order not to overshoot the point where inelastic strain rates become significant it is also necessary to limit the maximum stress increment. A final consideration is control of the local integration error when computing inelastic strain increments. For components in which fatigue life is a major consideration, the accurate calculation of local stresses and strains is crucial. In order to control the error, the time step should be chosen such that the local integration error does not exceed some allowable value.

In order to verify the 2D finite element code with Bodner's model, a number of uniaxial test cases were run and compared with published results (References 22-24). A representative example of the results of these calculations is shown in Figure 48. In addition, a large two-dimensional model (Figure 28) of the

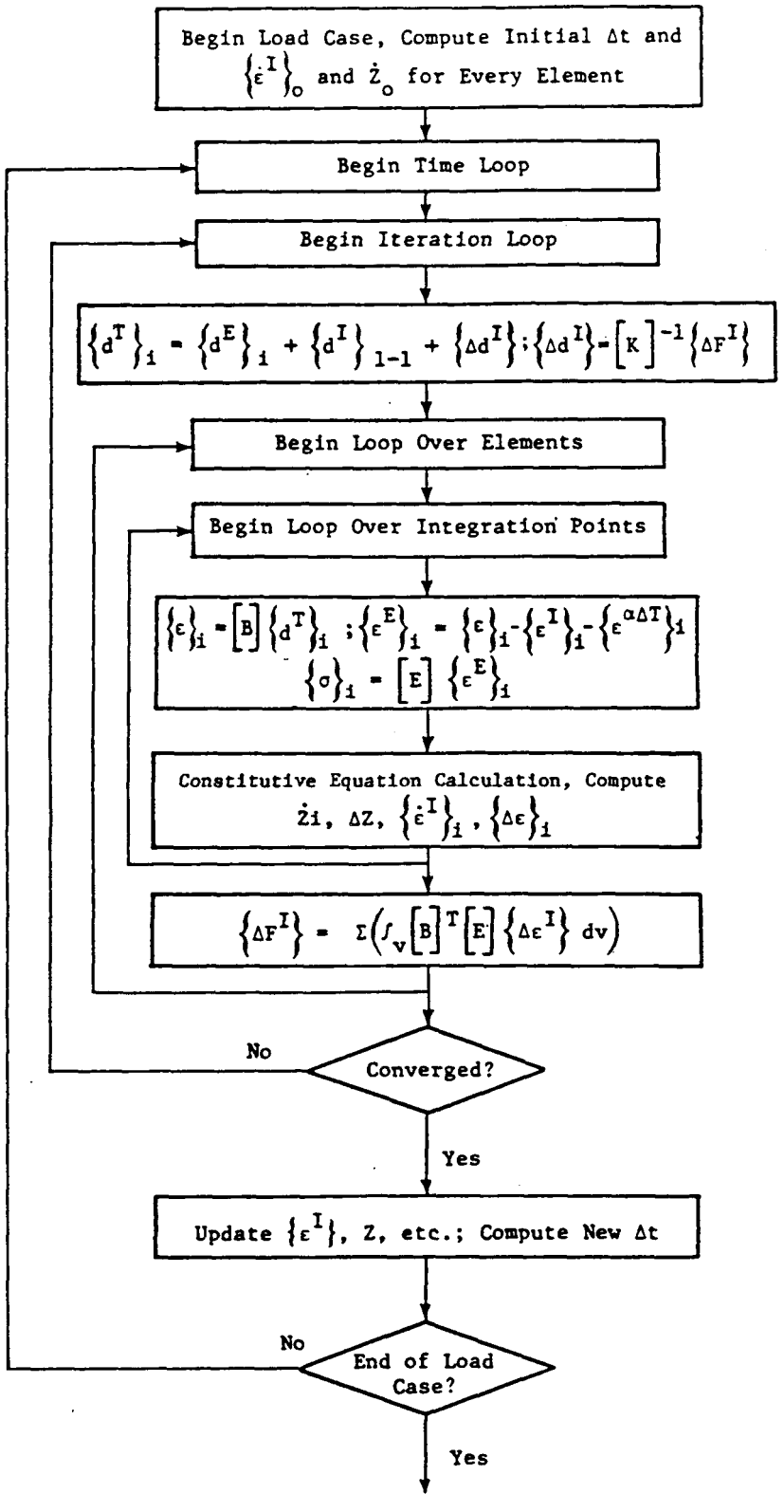

Figure 47. Iteration Scheme in Finite Element Code.

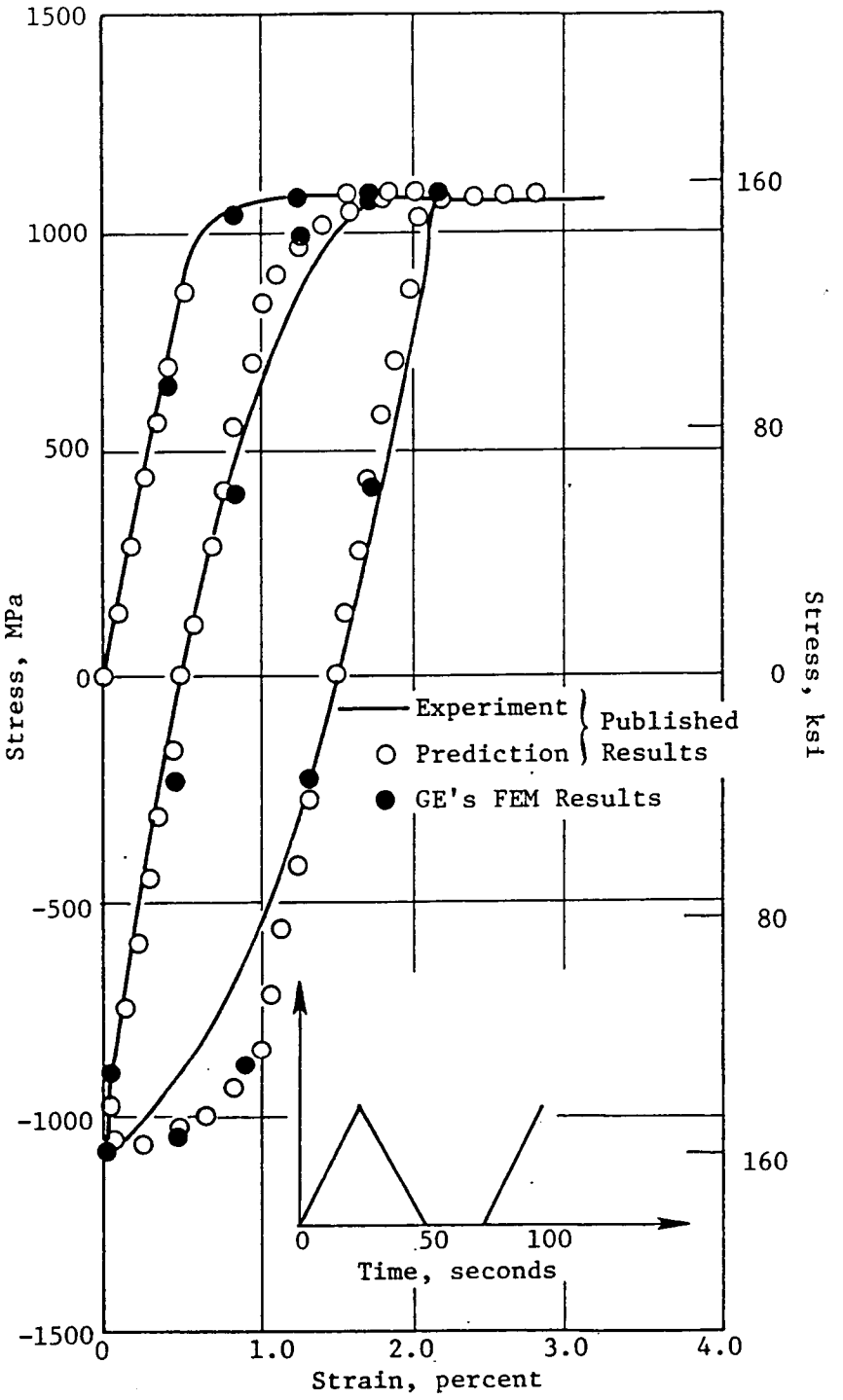

Figure 48. Predicted and Experimental Response of a Fatigue Loop with Stress Relaxation in Compression.

benchmark notch specimen (Reference 21) was constructed and run with three different loading histories and compared with published experimental results. An example of these comparisons can be seen in Figure 49. The overall performance of the finite element code with Bodner's model was quite good. The cost of running the code is comparable to one using a conventional uncoupled plasticity and creep constitutive model.

The second constitutive model will also be implemented in both the 2D and 3D codes.

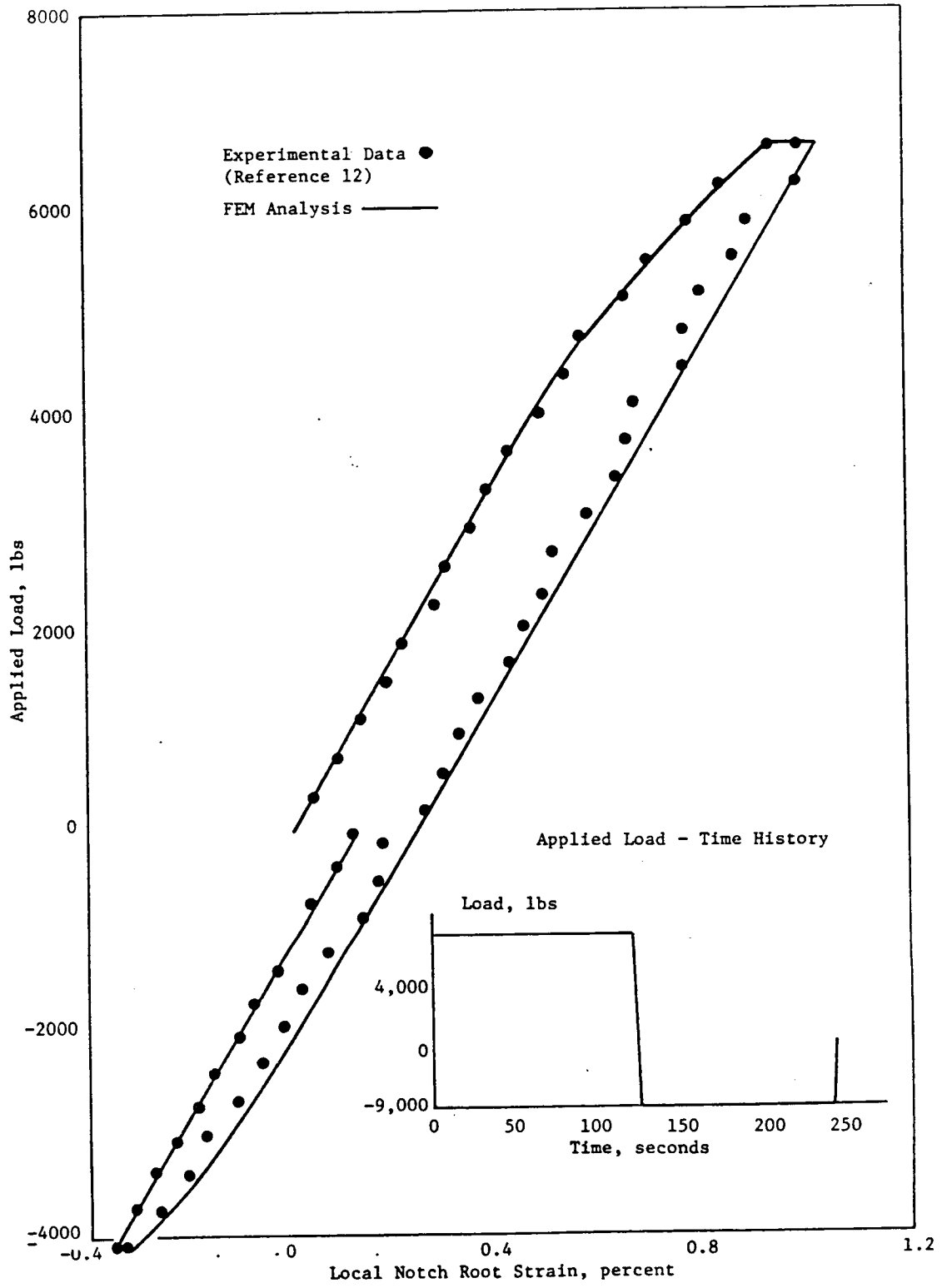

Figure 49. Comparison of Analytical Predictions to Experimental Results.

7.0 DISCUSSION

This report documented the work performed during the first year of Contract NAS3-23927, Constitutive Modeling for Isotropic Materials. As discussed in Section 3.0, conventionally-cast René 80 was selected as the base material for this study. Because of the thin walls of turbine blades and the large grain size of cast materials, all specimens studied were designed to have a wall-thickness of 0.76 mm (0.03 inches). Section 4.0 discussed the various data reduction methods for analyzing stress-strain data and the selection of the best method use in this effort. This system used automated test control and data acquisition equipment; this greatly reduced the work necessary to generate raw data from each experiment.

The screening of available models, discussed in Section 2.0, led to the selection of two: the Bodner model and a generic back stress/drag stress model. Work on both of these models is proceeding. In Section 5.0, the generic model was compared to a set of 980° C (1800° F) of René 80 data generated during the course of this work. These comparisons showed that the monotonic data at several strain rates could not be totally modeled using the generic theory. Furthermore, the cyclic and monotonic data could not be consistently modeled using this theory. In both cases, the constants for the theory were calculated using a specialized nonlinear optimization computer program. Work with this theory at other temperatures will be continued during the coming year.

Section 6.0 briefly discussed the development of a finite element computer code for use with the selected unified theories. The numerical algorithms in the code have been optimized to reduce the costs of structural analyses with unified theories. The program was verified by using the code and the Bodner model to analyze both simple, smooth-specimen and complex, benchmark-notch-specimen behavior. Further work with the code will include developing a 3D version and incorporating the generic unified model.

8.0 REFERENCES

1. Bodner, S. R. and Partom, Y., "Constitutive Equations for Elastic Viscoplastic Strain-Hardening Materials," ASME Journal of Applied Mechanics, ASME, June 1975.

2. Chaboche, J.L., "Thermodynamic and Phenomenonological Description of Cyclic Viscoplasticity with Damage," Translation of Publication No. 1978-3 of the Office National d'Etudes et de Researches Aerospatiales, France, by the European Space Agency Technical Translation Service, Publication No.ESA-TT-548, May 1979.

3. Haisler, W., "Application of an Uncoupled Elastic-Plastic Creep Constitutive Model to Metals at High Temperatures," Symposium on Nonlinear Constitutive Relations for High Temperature Applications, May 19-20, 1982, The University of Akron, Akron, Ohio.

4. Hart. E.W., Li, C.J., Yamada; H. and Wire, G.L., "Phenomenonological Theory: A Guide to Constitutive Relations and Fundamental Deformation Properties," Constitutive Equations in Plasticity, the MIT Press, Cambridge, Mass., London, A.S. Argon, Ed., 1975, pp.149-197.

5. Kreml, E., "On the Interaction of Rate and History Dependence in Structural Metals," Acta Mechanica, Vol. 22, pp.53-90, 1975.

6. Krieg, R. D., Swearengen, J. C., and Rohde, R. W., "A Physically-Based Internal Variable Model for Rate Dependent Plasticity," Proceedings of ASME/CSME PVP Conference, 1978.

7. Laflen, J.H., " A Constitutive Theory for Metal Creep," PhD Dissertation, University of Cincinnati, 1976.

8. Lee, D. and Zaverl, F., "A Description of History Dependent Plastic Flow Behavior of Anisotropic Metals," ASME Journal of Engineering Materials and Technology, ASME, Vol 101, January 1979.

9. Miller, A. "An Inelastic Constitutive Model for Monotonic, Cyclic and Creep Deformation (Parts I and II)," Journal of Engineering Materials and Technology, April 1976.

10. Pian, T.H.H., "Time-Independent Anisotropic Plastic Behavior by Mechanical Subelement Models," Proceedings of NASA Symposium on Nonlinear Constitutive Relations for High Temperature Applications, Akron, Ohio, May 1982.

REFERENCES (Continued)

11. Robinson, D.N. and Swindeman, R.W., "Unified Creep-Plasticity Constitutive Equations for 2 1/4 Cr-1 Mo Steel at Elevated Temperature," ORNL/TM-8444.

12. Valanis, K.C., "A Theory of Viscoplasticity Without a Yield Surface," Parts I and II, Archives of Mechanics, Archiwum, Mechaniki Stoswanej, 24, 4, 1971.

13. Walker, K. P. "Research and Development Program for Nonlinear Structural Modeling with Advanced Time-Temperature Dependent Constitutive Relationships," NASA CR-165533.

14. Stouffer, D. C., Papernik, L., and Bernstein, H. L., "Prediction of the Mechanical Response of a High Temperature Superalloy Rene 95," ORNL/TM-8444.

15. Robinson, D. N. "A Unified Creep-Plasticity Model for Structural Metals at High Temperature," ORNL/TM-5969.

16. Kaufman, M. "Examination of the Influence of Coatings on Thin Superalloy Sections," NASA CR-12115, August 1972.

17. Kaufman, M. "Examination of the Influence of Coating on Thin Superalloy Sections," Volume 1 and 2, NASA CR-134791 and CR-134792, December 1974.

18. McKnight, R. L., Laflen, J. H., Halford, G. R., and Kaufman, A., "Turbine Blade Nonlinear Structural and Life Analysis," AIAA-82-1056, 1982.

19. Bofferding, C. H. III, "A Study of Cyclic Stress and Strain Concentration Factors at Notch Roots Throughout Fatigue Life," M.S. Thesis, Michigan State University, 1980.

20. Guillot, M. "An Experimental Evaluation of Neuber's Cyclic Relation at Room and Elevated Temperature," Ph.D. Dissertation, Louisiana State University, 1981.

21. Domas, P. A., Sharpe, W. N., and Yau, J., "Benckmark Notch Test for Life Prediction," NASA CR-165571, June 1982.

22. Stouffer, D. C., and Bodner, S. R., "A Relationship Between Theory and Experiment for a State Variable Constitutive Equation," Mechanical Testing for Deformation Model Development, ASTM STP 765, R. W. Rohde and J. C. Swearengen, Eds., American Society for Testing and Materials, 1982, pp. 239-250.

REFERENCES (Concluded)

23. Bodner, S. R., "Representation of Time Dependent Mechanical Behavior of Rene 95 By Constitutive Equations," Air Force Materials Laboratory Report AFML-TR-79-4116, August 1979.

24. Stouffer, D. C., "A Constitutive Representation for IN100," Air Force Materials Laboratory Report AFWAL-TR-81-4039, January 1981.

APPENDIX

The subroutines used for the detailed evaluation of the various constitutive models reported here have the general three-dimensional form of the models, as reported in the cited references. However, for the purpose of evaluating the various material parameters of the models from test data, it is useful to reduce the general equations to uniaxial, isothermal form. Such uniaxial forms are listed in the following pages for the five theories examined in Section 2.0.

In these equations, the following notations are used (uniaxial):

$\dot{\varepsilon}^I$ = Inelastic Strain Rate

σ = Applied Stress

B = Back Stress

D = Drag Stress

$R = \int |\dot{\varepsilon}^I| dt$

1. Walker Model (Reference 13)

$$\dot{\varepsilon}^I = \left(\frac{|\sigma - B|}{D}\right)^n \frac{(\sigma - B)}{|\sigma - B|}$$

$$\dot{B} = (n_1 + n_2)\dot{\varepsilon}^I - (B - B_o - n_1\varepsilon^I)\left[(n_3 + n_4\, e^{-n_5|R|})|\dot{\varepsilon}^I| + n_6\,|B|^{m-1}\right]$$

$$D = D_1 - D_2\, e^{-n7|R|}$$

The following constants were used for Hastelloy X at 1200° F (Reference 13):

D_1 = 95631

D_2 = 0*

n^{-1} = 0.079

m = 1.16

n_1 = 0

n_2 = 1.5E7

n_3 = 781

n_4 = 0

n_5 = 0

n_6 = 0

n_7 = 0*

B_o = -2000

*D_2 = -40,000 and N_7 = 100 were used for checking the cyclic softening capability.

2. Krieg, Swearengen, and Rohde Model (Reference 6)

$$\dot{\varepsilon}^I = C_1 \left(\frac{|\sigma - B|}{D} \right)^{C2} \frac{\sigma - B}{|\sigma - B|}$$

$$\dot{B} = C_3 \dot{\varepsilon}^I - C_4 B^2 \left[e^{C_5 B^2} - 1 \right] \frac{B}{|B|}$$

$$\dot{D} = C_6 |\dot{\varepsilon}^I| - C_7 (D - D_o)^n$$

The following constants were used for aluminum, 110° F (Reference 6):

$C_1 = 6.0 \times 10^{-13}$ 1/sec
$C_2 = 6.05$
$C_3 = 424$ MPa
$C_4 = 7.8016 \times 10^{-15}$ MPa^{-2}
$C_5 = 1.15875 \times 10^{-3}$ MPa^{-2}
$C_6 = 0$
$C_7 = 0$
$D_o = 0$
$n = 1.0$

3. Miller Model (References 9 and 13)

$$\dot{\varepsilon}^I = \left\{ \beta\theta^1 \text{ Sinh } \left[\frac{|\sigma - B|}{D} \right]^{1.5} \right\}^n \frac{(\sigma - B)}{|\sigma - B|}$$

$$\dot{B} = H_1 \dot{\varepsilon}^I - H_1 \beta\theta^1 \left\{ \text{Sinh } (A_1 |B|) \right\}^n \frac{B}{|B|}$$

$$\dot{D} = H_2 |\dot{\varepsilon}^I| (C_2 + |B| - \frac{A_2}{A_1} D^3) - H_2 C_2 \beta\theta^1 \left\{ \text{Sinh } (A_2 D^3) \right\}^n$$

$$\theta^1 = \bar{e}^{Q/kT} \text{ for } T \geq 0.6Tm$$

$$= e^{-\left\{ \frac{Q}{0.6kTm} \left[1 + \ln\left(\frac{0.6Tm}{T}\right) \right] \right\}} \text{ for } T \leq 0.6Tm$$

The following constants were used for Hastelloy X at 1200° F (Reference 13):

$D_o = 8000$ psi
$n = 1.598$
$B = 1.0293$ E14 1/sec
$H_1 = 1.0$E7 psi

A_1 = 9.305E-4 psi

H_2 = 100

C_2 = 50,000 psi

A_2 = 5.9425E-12 psi^{-3}

Q = 104600 Cal./Mole

T_m = 1588 K

k = 1.9859

4. Robinson Model (References 11 and 15)

$$\dot{\varepsilon}^I = \frac{1}{2\mu} F^{\frac{n-1}{2}} \left[\frac{2}{3}\sigma - B\right] \quad F>0,\ \sigma B > 0 \text{ and } \sigma\left(\frac{2}{3}\sigma - B\right) > 0$$

or

$$F>0 \text{ and } \sigma B \leq 0$$

$$= 0 \quad F \leq 0$$

or $F > 0$, $\sigma B > 0$ and $\sigma\left(\frac{2}{3}\sigma - \alpha\right) \leq 0$

$$\dot{B} = \frac{2\mu H}{\sqrt{\frac{3}{4}}\left|\frac{B}{K}\right|^{\beta}} \dot{\varepsilon}^I - R\left(\sqrt{\frac{3}{4}}\left|\frac{B}{K}\right|\right)^{n-\beta-1} B; \quad |B| > B_o, \ \sigma B > 0$$

$$= \frac{2\mu H}{\sqrt{\frac{3}{4}}\left|\frac{B_o}{K}\right|^{\beta}} \dot{\varepsilon}^I - R\left(\sqrt{\frac{3}{4}}\left|\frac{B_o}{K}\right|\right)^{n-\beta-1} B; \quad |B| \leq B_o, \ \sigma B \leq 0$$

$$F = \left(\frac{1}{3}\sigma^2 + \frac{3}{4}\alpha^2 - \sigma\alpha\right) / K^2 - 1$$

The following constants were used for 2 1/4 Cr-Mo Steel at 1000^o F (Reference 11):

$\mu = 3.61 \times 10^7$

n = 4

m = 7.73

β = 1.5

$R = 9.0 \times 10^{-3}$ ksi/h

$H = 1.37 \times 10^4$ ksi/h

B_o = 0.14 ksi

K = 0.82 ksi

5. Bodner Model (Reference 14)

$$\dot{C} = \frac{2}{\sqrt{3}} \left|\frac{\sigma}{\sigma}\right| D_o \exp\left[-\frac{n+1}{2n}\left(\frac{Z}{\sigma}\right)^{2n}\right]$$

$$\dot{Z} = m\,(Z_1 - Z)\,\dot{W}^p - AZ_1\,\frac{(Z-Z_2)^r}{Z_1}$$

The following constants were used for Rene 95 at 1200° F (Reference 14):

$D_o = 10^4\ \text{sec}^{-1}$ $\quad$ $A = 4 \times 10^{-4}\ \text{sec}^{-1}$

$n = 3.2$ $\quad$ $r = 1.5$

$Z_1 = 319$ ksi $\quad$ $E = 2.57 \times 10^4$ ksi

$Z_o = 232$ ksi

$Z_2 = 319$ ksi

$m = 2.758\ \text{ksi}^{-1}$